The elastic, electronic, and structural properties of hydrous, sulfur-bearing minerals in planetary environments: from the surface to deep interiors

Thesis by
Olivia S. Pardo

In Partial Fulfillment of the Requirements for the
Degree of
Geophysics

CALIFORNIA INSTITUTE OF TECHNOLOGY
Pasadena, California

2023
Defended May 25th, 2023

Olivia S. Pardo
ORCID: 0000-0003-3964-9272

Acknowledgements

Thank you to my thesis committee: Mike Gurnis, Paul Asimow, George Rossman, and Jennifer Jackson for their insights, holding space for any and all of my questions, and enthusiasm. To Jennifer, for imparting her expertise in a way that both challenges and inspires me as scientist, and for her kindness and guidance through my Ph.D. and life. I am grateful to Wolfgang Sturhahn, whose valuable knowledge, input, and humor has greatly improved every data analysis, group meeting, and backyard barbecue. To my labmates over the last six years: you have made me a better scientist and friend and will continue to be a source of admiration. Thank you to Julie, Donna, Kim, and Sarah for their dedication to students and unwavering support; especially to Sarah for always having an open chair to sit and talk. I'd like to thank my first research mentors, Andy Campbell, Lily Thompson, and Bethany Chidester for their guidance, making me feel valued, and welcoming me into science. Finally to my friends and loved ones: if I were to make a list of all the reasons that I have to be grateful for you it might just reach the center of the Earth.

This work was funded in part by the W.M. Keck Foundation and the National Science Foundation (NSF-CSEDI-EAR-1600956, 2009935). I acknowledge the support of DOE NNSA SSGF (DE-NA0003960). Part of this work was performed at the National Synchrotron Light Source II at Brookhaven National Laboratory and was funded by the Department of Energy (DEAC98- 06CH10886). The use of the 22-IR-1 beamline was supported by COMPRES under NSF Cooperative Agreement EAR 11-57758 and CDAC (DE-FC03-03N00144). This research used resources of the Advanced Photon Source, a U.S. Department of Energy (DOE) Office of Science User Facility operated for the DOE Office of Science by Argonne National Laboratory under Contract No. DE-AC02-06CH11357. Beamline 3-ID-B at the Advanced Photon Source is partially supported by COMPRES, the Consortium for Materials Properties Research in Earth Sciences under NSF cooperative agreement EAR–1606856.

Abstract

In this thesis, a comprehensive investigation of the hydrous iron endmember sulfate szomolnokite ($FeSO_4 \cdot H_2O$) has been conducted using a suite of complementary techniques to measure its structural, elastic, electronic, and vibrational properties under extreme conditions. Through X-ray diffraction (XRD), nuclear resonant inelastic X-ray scattering (NRIXS), synchrotron Mössbauer spectroscopy (SMS), and synchrotron Fourier transform infrared spectroscopy (FTIR) in the diamond anvil cell, the material properties of szomolnokite have been characterized under high pressures and low temperatures relevant to hydrous, sulfur-rich planetary environments. XRD measurements presented in this work have revealed two structural phase transitions occurring at pressures between 5.0 and 6.6 GPa and between 12.7 and 16.8 GPa, with the latter phase stable up to 80 GPa. The elastic parameters of each phase have been determined by fitting third-order Birch-Murnaghan equations of state. I compare our results with elastic parameters of other relevant sulfate phases, highlighting the importance of reporting and comparing these parameters at the pressures where the phases are stable. Using NRIXS and SMS, the lattice vibrational response and the effects on the iron electronic environments during the structural transitions are examined. The NRIXS and SMS data reveal distinct features and pressure-dependent behaviors that characterize alterations in both iron site-specific and bulk lattice properties associated with the phase transitions, including lattice softening and decreased iron-coordination environment symmetry. Utilizing both the NRIXS and XRD results, I discuss how the presence of sulfates in the ice-rich crusts of planetary bodies could affect tidal loading observations. Synchrotron FTIR measurements demonstrate that structurally bound H_2O is retained within the unit cell during the structural transitions and upon subsequent decompression, confirming the retention of water up to 23 GPa and temperatures as low as 20 K and indicating the reversibility of both structural transitions. Supported by our quantum-mechanics molecular dynamics simulations, the existence of two vibrationally unique water sites in szomolnokite's crystal structure is proposed to

explain the experimentally observed H_2O-related features. I develop a spectral diagnostic for observing the high pressure structural transformations at ambient and low temperatures. The measured partial phonon density of states, predicted vibrational density of states, and measured FTIR spectrum are compared. Drawing from the insights gained, we emphasize the advantages of employing complementary experimental and computational techniques and discuss future research directions that can further enhance our knowledge of hydrous, sulfur-rich planetary environments.

Published Content and Contributions

Pardo, O. S., V. V. Dobrosavljevic, T. Perez, W. Sturhahn, Z. Liu, G. R. Rossman, and J. M. Jackson (Mar. 1, 2023). "X-ray diffraction reveals two structural transitions in szomolnokite." In: *American Mineralogist* 108.3, pp. 476–484. ISSN: 0003-004X, 1945-3027. DOI: 10.2138/am-2022-8147. *O.S.P conducted the experimental work and data analysis, and wrote the original manuscript with J.M.J supervision*.

Pardo, O. S., V. V. Dobrosavljevic, W. Sturhahn, T. S. Toellner, B. Strozewski, and J. M. Jackson (May 1, 2023). Lattice dynamics, sound velocities, and atomic environments of szomolnokite at high pressure. preprint. In Review. DOI: 10.21203/rs.3.rs-2861032/v1. *O.S.P conducted the experimental work and data analysis, and wrote the original manuscript with J.M.J supervision*.

TABLE OF CONTENTS

LIST OF ILLUSTRATIONS

LIST OF TABLES

Chapter 1

INTRODUCTION

1.1 Sulfates in the solar system

Hydrous sulfates and other sulfate salts are found in natural environments throughout the solar system: on Earth, Mars, the icy satellites, and even asteroids. On Earth's surface, both hydrous and anhydrous sulfate minerals naturally form through many processes, including formation as weathering products of pyrite, pyrrhotite, or SO_2-basalt interactions, and have been studied in relation to evaporate deposits, hydrothermal systems, mine waste, and as components of igneous rocks from a variety of volcanic systems (Rye, 2005; Chou, Seal, and Wang, 2013; Dyar et al., 2013; McCanta, Dyar, and Treiman, 2014; Machado de Oliveira et al., 2019). These observations have shown that sulfates can host a variety of cations, such as Fe, Mg, Na, Ca, Cu, Mn, and Al, and varying amounts of molecular water and hydroxyl groups. Sulfate cations can be of mixed valence states, and sulfate minerals with different cation valence states can coexist depending on the degree of weathering and environmental conditions. These sulfates may be may be further altered on short timescales (hours to days), generating complex chemical mixtures (McCollom et al., 2013; Wang, Jolliff, et al., 2016). Depending on an environment's redox conditions, these sulfates are capable of releasing significant amounts of trace metals and volatiles into the surrounding environment during these alteration processes (Chou, Seal, and Wang, 2013). When considering their presence in Earth's interior, as discussed below, the redox-sensitivity of sulfur makes these sulfates and sulfur-bearing minerals important phases when characterizing redox properties of the mantle and mantle-derived magma, mantle-crust element partitioning, and degassing of magma and volcanic eruptions (Chowdhury and Dasgupta, 2019).

Hydrous sulfur-bearing phases, and sulfates in particular, are discussed in relation to volatile cycling specifically as phases brought into Earth's mantle via subducting slabs (Bénard et al., 2018; Schwarzenbach et al., 2018; Li et al., 2021; Muth and

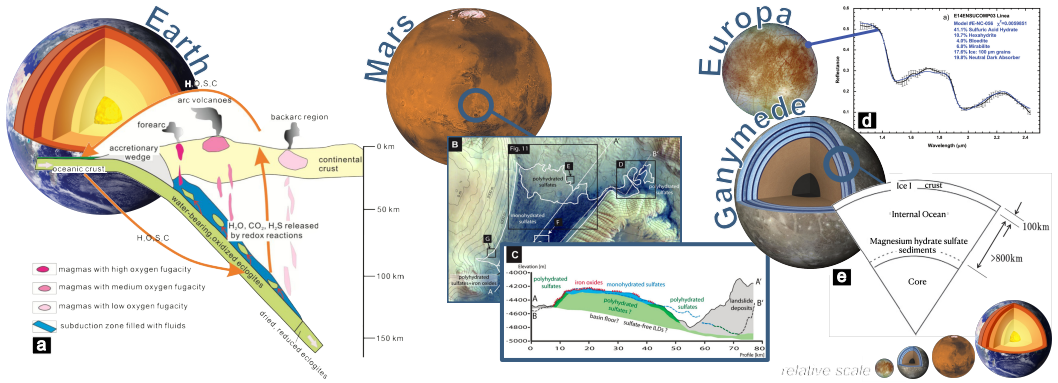

Figure 1.1: Occurrence of sulfur within the solar system on Earth, Mars, and the icy satellites. Panels **a**, **b**, **c**, **d**, **e** are figures from Liu et al. (2016), Lichtenberg et al. (2010) (**b, c**), Dalton, Shirley, and Kamp (2012), and Nakamura and Ohtani (2011), respectively. Images of Earth, Mars, Europa, and Ganymede are credited to NASA/JPL.

Wallace, 2021; Liu et al., 2016). Subducted sulfate may then act as an oxidizing agent at depth upon release from the slab into the overlying mantle wedge, affecting melt compositions (see Figure 1.1 panel **a**). Isotopic δ^{34}S values in eclogite suggest that mantle-derived sulfides may have initially formed as sulfate in seawater, then were subsequently subducted along with basalt into the deep mantle before undergoing further alteration (Bataleva, Palyanov, and Borzdov, 2018). Though there is likely release of sulfate at relatively shallower depths, observations of sulfate inclusions in diamonds, such as $CaSO_4$, suggest that oxidized sulfur is stable and/or recycled to some degree in the deep mantle (e.g., Wirth et al., 2009). Experimental results have supported these observations by demonstrating three thermodynamically stable polymorphs of $CaSO_4$ up to 90 GPa and 1500 K (Fujii, Ohfuji, and Inoue, 2016). However, the abundance of hydrous sulfate phases brought down into the mantle and their stabilities at elevated pressures and temperatures remains unknown.

Though we now have observations of hydrous sulfates and other sulfur-bearing phases on other planetary surfaces like Mars and the icy satellites, even less is known about the interior volatile cycles and the connection between the observed surface phases and interior dynamics of these planetary bodies. Because of the many hydrous sulfates found in close proximity to each other in natural environments and laboratory experiments on Earth, interpretation of remote observations of Mars and the icy satellites has focused on selecting mixtures of sulfates, sulfides, and hydrous phases that reproduce observed infrared, near-infrared, and visible wavelength spectral fea-

tures (Lane, Dyar, and Bishop, 2004; Bishop, Parente, and Weitz, 2009; Lichtenberg et al., 2010; Dalton, Shirley, and Kamp, 2012; Bu et al., 2018). Observations from orbit performed by the Mars Reconnaissance Orbiter (MRO) Compact Reconnaissance Imaging spectrometer for Mars (CRISM) built upon previous in-situ measurements by the Mars Exploration Rover Opportunity and identified layers of sulfate-rich deposits hundreds of meters thick in several locations (e.g., Meridiani Planum) (Lichtenberg et al., 2010) (see Figure 1.1 panel **b, c**). Subsequently, the Curiosity rover observed hydrated sulfates in Gale crater, suggesting that their presence across the entire planet may be important for understanding planetary-wide aqueous processes (Nachon et al., 2014).

The abundance of sulfur on the surface and exposed subsurface of Mars combined with Martian meteorite analysis suggests a more S-rich Martian mantle and core compared to Earth (Gaillard and Scaillet, 2009; Franz, King, and Gaillard, 2019); therefore the observed sulfate phases may play (or have played) a larger role in interior sulfur and water cycling compared to Earth. The abundance of $M^{2+}SO_4 \cdot nH_2O$ (M = Mg, Fe, Ca) phases has led to hydrated sulfates' importance as potential subsurface hosts for water and their use in determining past hydrological activity on the surface of Mars (Lichtenberg et al., 2010; Wendt et al., 2011; McCanta, Dyar, and Treiman, 2014; Franz, King, and Gaillard, 2019). More specifically, orbiter and lander measurements have identified the iron end-member szomolnokite ($FeSO_4.H_2O$), amongst other mono- and poly-hydrated sulfates across Mars (Wang, Haskin, et al., 2006; Bishop, Parente, and Weitz, 2009; King and McLennan 2010; Wendt et al., 2011; Chou, Seal, and Wang, 2013; Singh et al., 2022).

Spectroscopy measurements taken by the Galileo spacecraft identified hydrous sulfur-bearing material on the surface of Europa, specifically on the trailing hemisphere which is significantly darker and spectrally distinct from the ice-rich leading hemisphere (McEwen, 1986; Carlson et al., 2009). Spectral laboratory measurements and computational modeling have identified sulfate-ice mixtures as best matches to the observational data (Dalton, Shirley, and Kamp, 2012; Cerubini et al., 2022; King, Fletcher, and Ligier, 2022) (see Figure 1.1 panel **d**), however the origin of the sulfur-rich phases on the surface is not fully understood. Recent work has suggested a primarily exogenic sulfur source for the surfaces of Io, Europa, and Ganymede (e.g., Trumbo, Brown, and Hand, 2020). For Europa in particular, sulfur radiolytic chemistry resulting from sulfur implantation due to volcanic activity on Io is thought to be one of the main causes for the difference in color and spectral features of Eu-

ropa's trailing hemisphere. Current work suggests endogenic surface material alteration by exogenic sulfur radiolysis (Carlson et al., 2009; Trumbo, Brown, and Hand, 2020), but cannot rule out at least some quantities of endogenic S, such as localized concentrations of SO_2, for example (Becker et al., 2022).

Due to the observed abundance of sulfate on the surface, it has been proposed that hydrated sulfates are primary components of the icy satellite's interior oceans and/or icy mantles and has motivated work on hydrous sulfates at high pressures (Fortes, Wood, Alfredsson, et al., 2006; Fortes, Brand, et al., 2013; Fortes, Fernandez-Alonso, et al., 2017; Nakamura and Ohtani, 2011; Comodi et al., 2014; Pan, Yong, and Secco, 2020). Candidate sulfates primarily consists of Na- and Mg-bearing sulfates with various hydration states. Much work has a focused on magnesium end member hydrated sulfates, which have been modeled in the interior of Ganymede as a layer of sediments at the top of a silicate mantle (see Figure 1.1 panel **e**) (Nakamura and Ohtani, 2011). The interior structures of the icy satellites are subjects of ongoing work (e.g., Gomez Casajus et al., 2021), but gravity field and magnetometer data from spacecraft like Galileo have led to the current understanding of interior ice, mantle, and core layers. Europa, the smallest of the Galilean moons, is differentiated and likely composed of an iron-rich core, silicate mantle, ocean, and ice-rich crust (Carr et al., 1998; Anderson et al., 1998; Hussmann, Sotin, and Lunine, 2015). The largest Galilean moon, Ganymede, may have a more complex differentiated interior composed of an iron-rich core, silicate mantle, and a basal ice-rich layer underlying the ocean and ice-rich crust (Hussmann, Sotin, and Lunine, 2015). Depending on the dynamics within and between these layers, it has been proposed that rocky materials and precipitating salts (e.g., sulfates) in the ice-rich crust and ocean should sink towards and through the basal ice layer, potentially cycling sulfur-bearing phases from the surface of the icy crust to the basal ice-rock interface at the top of the silicate mantle (Vance et al., 2014; Ligier et al., 2019; Molyneux et al., 2020). Internal heating could melt the ice at this interface and cause fluid-rock interactions (Ahrens et al., 2022).

Geologic interpretations of surface imaging and dynamical modeling support surface-subsurface exchange within Ganymede and the other icy satellites (Prockter et al., 2017; Howell and Pappalardo, 2018; Buffo et al., 2020), Thus, the observed abundance of hydrated sulfates on their surfaces may be indicative of their presence at depth and motivates ongoing high pressure work (Zolotov, 2019). While Na- and Mg-rich sulfates are abundant on the surfaces of the icy satellites and have been

the focus of existing high-pressure experimental work, it is frequently observed on Earth and Mars that other 2+ cations can readily substitute in $Me^{2+}SO_4 \cdot nH_2O$ phases. Fe-bearing compositions may be present in higher concentrations at greater depths, especially when considering additional sources of sulfates such as leaching of chondritic sulfates from an iron-rich core into an overlying mixed ice-rock mantle (Kargel, 1991).

The ability for sulfates to host multiple cations in solid solution and the multi-mineral nature of these natural systems containing hydrous sulfates necessitates better chemical and physical characterization of the endmembers, like the iron endmember szomolnokite $FeSO_4 \cdot H_2O$. Whether these sulfates act as components in a localized volatile cycling system, or as major planetary interior phases, high pressure data is needed to better model these environments. Their stability at depth determines, in part, their volatile transport capabilities and geophysical behavior. For example, structural phase transitions influence the dynamics and seismic signatures within planetary interiors, especially for phase transitions exhibiting large volume changes. As an endmember hydrated sulfate, szomolnokite provides a means to study the effects of iron on phase stabilities and elastic properties, for example.

Characterization of szomolnokite under high-pressure conditions will help develop our understanding of the complex behavior of this class of minerals and their role in planetary interior environments. I have performed a suite of multi-modal measurements to construct a comprehensive thermoelastic description of szomolnokite under planetary conditions. I focus on an environment in which hydrated sulfates may be the dominant phase by utilizing high-pressure, cryogenic temperature conditions most applicable to icy, sulfur-rich planetary bodies like those in our solar system. The interplay of these spectroscopic techniques and the structural, electronic, and vibrational properties they measure are described below.

1.2 The interplay of structural, electronic, and vibrational material properties

A material's properties can be described at multiple length-scales and probed using a variety of techniques. For example, information about the "large-scale" periodic arrangement of atoms in a crystalline material can be gleaned from X-ray diffraction experiments and allows one to determine its crystal family and internal symmetry (e.g., a cubic structure), volume, and density. The crystal symmetry (i.e., space group) describes the large-scale structure, by determining the number of allowed vi-

brational modes, their degeneracy and polarization, and the orientation-dependent energy of the modes in the crystal, which in turn are intimately linked to the elastic and vibrational properties of a material. The elastic properties of a material (e.g., seismic wave velocities) may be described as an average of all X-ray propagation orientations by analyzing a sample comprised of many, randomly oriented crystals. On the same sample, small-scale interactions within specific atomic bonding environments and even the electronic environments of individual atoms may be probed.

To characterize szomolnokite at multi-scales, I have utilized three complementary scattering techniques: X-ray diffraction (crystal structure and elastic properties), nuclear resonant spectroscopy (electronic, elastic, and vibrational properties), and infrared spectroscopy (molecular structure and vibrational properties). Each of these techniques relies on different physical principles to interact with the sample and probe different aspects of szomolnokite, providing valuable and complementary information. By utilizing high-pressure devices to perform these measurements at high pressure and low temperature, we are able to characterize the evolution of szomolnokite's thermoelastic properties as a function of pressure and temperature relevant to a variety of planetary surfaces and interiors. These experiments are further complemented by theoretical modeling which validates and improves our analysis and interpretations of the data, demonstrating the strong advantages of combining multiple methods of material property investigation.

1.3 Thesis overview

As described above, the ability to understand and model the natural environments in which we find hydrated sulfates relies on our ability to know the properties of the endmembers that comprise these chemical systems. In this thesis, I present experimental results that contribute to a more detailed understanding of the micro- and macroscopic properties of the iron endmember szomolnokite. The experiments described in this thesis span the pressures associated with sulfur cycling in subduction zones on Earth and the full range of pressures and temperatures of the solar system's icy satellites interiors, including larger, icy bodies that may exist outside of the solar system.

In Chapter 2, I present changes in the crystal structure of szomolnokite in response to compression and associated elastic properties utilizing X-ray powder diffraction, including a detailed analysis of szomolnokite's equation of state to pressures of 83 GPa (Pardo, Dobrosavljevic, Perez, et al., 2023). Within this pressure range, two

different structural phase transitions are revealed: a monoclinic $C2/c$ to triclinic $P\bar{1}$ phase transition at 6 GPa (β-phase), and a triclinic $P\bar{1}$ to monoclinic $P2_1$ phase transition occurring between 13-17 GPa (γ-phase). By fitting finite-strain equations of state to the data for each polymorph we compare against previous work and present new results on the γ-phase. In Chapter 3, I present the results of ^{57}Fe nuclear resonant spectroscopy experiments, specifically synchrotron Mössbauer spectroscopy (SMS) and nuclear resonant inelastic X-ray scattering (NRIXS). SMS and NRIXS were performed in the diamond anvil cell to measure the electronic and vibrational properties of szomolnokite up to 14.5 GPa. We find evidence of crystal lattice softening, changes in elastic properties, and variations in the electric field gradients of iron atoms associated with two structural transitions occurring within the experimental pressure range. In combination with the elastic parameters determined in Chapter 2, I apply these findings to icy satellite interiors, including discussion of elastic properties and implications for tidal observations.

In Chapter 4, I present the results of high pressure, cryogenic synchrotron Fourier transform infrared spectroscopy (FTIR) on szomolnokite, which measures the vibrational properties up to 24 GPa and down to 20 K. To better inform this experimental analysis, I collaborated with William Palfey (Caltech) and present the results of his quantum-mechanical molecular dynamics simulations. We compare our predicted vibrational density of states with our previous ^{57}Fe nuclear resonant inelastic X-ray scattering measurements results at 1 bar. We combine our experimental data to our theoretical vibrational spectra of szomolnokite and present a model for O-H vibrational mode broadening in response to pressure. Changes in H_2O bonding environments as a function of pressure are diagnostic of the structural phase transitions discussed in Chapter 2. Importantly, the synchrotron FTIR analysis reveals that for each phase transition, structurally bound H_2O is retained in the unit cell, even upon decompression and temperature cycling.

In Chapter 5, I summarize the work in this thesis, highlighting the advantages of performing complementary techniques that have led to our understanding of the properties of an iron-endmember hydrated sulfate. Informed by the work in this thesis, I discuss future research directions that will continue to build upon our growing ability to understand hydrous, S-rich planetary environments.

Chapter 2

X-RAY DIFFRACTION REVEALS TWO STRUCTURAL TRANSITIONS IN SZOMOLNOKITE

**This chapter has been previously published as:*
Olivia S. Pardo, Vasilije V. Dobrosavljevic, Tyler Perez, Wolfgang Sturhahn, Zhenxian Liu, George R. Rossman, Jennifer M. Jackson (March 1, 2023) X-ray diffraction reveals two structural transitions in szomolnokite. American Mineralogist; 108 (3): 476–484. doi: https://doi.org/10.2138/am-2022-8147

2.1 Introduction

Szomolnokite ($FeSO_4 \cdot H_2O$) is a hydrous, ferrous iron-sulfate belonging to the kieserite group of minerals which is composed of monoclinic hydrated metal sulfates. On Earth, szomolnokite and other metal sulfates naturally occur as weathering products of pyrite or pyrrhotite and have been studied in relation to evaporate deposits, hydrothermal systems, and mine waste (Chou, Seal, and Wang, 2013; Dyar et al., 2013; Machado de Oliveira et al., 2019). Because ferrous iron-sulfates can host numerous other divalent metals, such as Cu and Mn, they are capable of releasing significant amounts of other trace metals into the surrounding environment (Chou, Seal, and Wang, 2013). Hydrated sulfates have also been discussed in relation to volatile cycling within the mantle and their role as potential oxidizing agents upon release of their volatiles at depth (Bénard et al., 2018; Schwarzenbach et al., 2018; Li et al., 2021).

Hydrated sulfates are not only studied in relation to surface and subsurface processes on Earth but have more recently become of interest for other planetary bodies, after sulfate minerals, including szomolnokite, were detected on Mars using absorption spectroscopy (Bishop, Parente, and Weitz, 2009; King and McLennan, 2010; Chou,

Seal, and Wang, 2013). This has led to hydrated sulfates' importance as potential hosts for water at depth, their use in determining past hydrological activity on the surface of Mars, and their role in volatile and sulfur cycling (Lichtenberg et al., 2010; Wendt et al., 2011; McCanta, Dyar, and Treiman, 2014; Franz, King, and Gaillard, 2019). On Venus, sulfates are hypothesized to exist at the surface and crust (Barsukov, Volkov, and Khodakovsky, 1982). Additionally, hydrous metal sulfates have been proposed to exist on the surface of icy moons in our solar system owing to their spectral similarity between laboratory measurements and remote observations (Dalton and Pitman, 2012; Ligier et al., 2019; Trumbo, Brown, and Hand, 2020).

Hydrated sulfates have been characterized under a range of pressures and temperatures. Szomolnokite has a monoclinic crystal structure (space group $C2/c$) at ambient conditions as determined by early X-ray diffraction (XRD) measurements on powdered szomolnokite (Pistorius, 1960), and ambient pressure single crystal XRD measurements (Wildner and Giester 1991, Giester, Lengauer, and Redhammer, 1994) (see Table 2.1). At ambient conditions szomolnokite belongs to the kieserite group, which consists of monoclinic, hydrous metal sulfates ($M\mathrm{SO_4}\cdot\mathrm{H_2O}$). The kieserite structure consists of corner sharing $[M\mathrm{O_4}(\mathrm{H_2O})]^{6-}$ units running parallel to the crystallographic c-axis. Most recently, single crystal, high-pressure XRD measurements combined with Raman and Fourier-transform infrared (FTIR) spectroscopy up to 9.2 GPa found a monoclinic-triclinic structural phase transition at 6.154(1) GPa and retention of structurally-bound $\mathrm{H_2O}$ throughout the pressure range investigated (Meusburger, Ende, Talla, et al., 2019). An analogous transition was observed to occur in the Mg-endmember kieserite ($\mathrm{MgSO_4}\cdot\mathrm{H_2O}$) at lower pressures (Meusburger, Ende, Matzinger, et al., 2020), the Ni-endmember dwornikite ($\mathrm{NiSO_4}\cdot\mathrm{H_2O}$) (Ende et al., 2020), and the Co-endmember ($\mathrm{CoSO_4}\cdot\mathrm{H_2O}$) (Wildner, Ende, et al., 2021).

Table 1. Szomolnokite ambient condition lattice parameters.

a (Å)	b (Å)	c (Å)	b (°)	Volume (Å^3)	Ref.
7.624(9)	7.469(9)	7.123(9)	115.86(3)	391.70	Pistorius (1960)[a]
7.078(3)	7.549(3)	7.773(3)	118.65(2)	364.45	Wildner and Giester (1991)[b]
7.084	7.550	7.779	118.63	365.16	Giester et al. 1994[a]
7.086(1)	7.555(1)	7.780(1)	118.61(1)	365.63(8)	Talla and Wildner (2019)[b]
7.0823(2)	7.5525(2)	7.7786(5)	118.631(3)	365.23(30)	Meusburger et al. (2019)[b]
7.086(2)	7.5497(3)	7.779(2)	118.656(3)	365.15(3)	This work[a]

Table 2.1: Szomolnokite ambient condition lattice parameters.
Notes: uncertainties are given in parentheses for the last significant digit(s).
[a]Powder X-ray diffraction.
[b]Single crystal X-ray diffraction.

Other studies conducted on hydrated sulfates have focused on decomposition induced by moderate pressure and variable temperature. Neutron powder diffraction of deuterated $MgSO_4 \cdot 11D_2O$, the deuterated analog of meridianiite, was used to explore pressures between 0.1-1000 MPa and temperatures between 150-280 K (Fortes, Fernandez-Alonso, et al., 2017). At ambient conditions meridianiite is triclinic (space group $P\bar{1}$) with a structural phase transition and decomposition of $MgSO_4 \cdot 11D_2O$ to ice VI + $MgSO_4 \cdot 9D_2O$ occurring at 0.9 GPa and 240 K. The relatively dehydrated $MgSO_4 \cdot 9D_2O$ is monoclinic (space group $P2_1/c$). Additional work has focused on the decomposition of hydrous, Cu-, Ni-, Zn-, and Fe-bearing sulfates as a function of temperature using X-ray photoelectron spectroscopy, scanning electron microscopy/X-ray microanalysis, thermogravimetric analysis, diffuse reflectance infrared Fourier transform spectroscopy, and X-ray diffraction (Siriwardane et al., 1999). Results for the $FeSO_4 \cdot 7H_2O$ sample used in these decomposition experiments indicate dehydration initiating at temperatures up to 200°C with the decomposition of sulfate initiating around 500°C, producing Fe_2O_3 (Siriwardane et al., 1999).

Phase relations of $MSO_4 \cdot nH_2O$ systems have been explored at high pressure and temperature. One experiment on the $MgSO_4$-H_2O system at temperatures ranging from 298-500 K and pressures up to 4.5 GPa found a eutectic system with six distinct phases (Nakamura and Ohtani, 2011). Using X-ray diffraction and micro-Raman spectrometry, $MgSO_4 \cdot H_2O$, $MgSO_4 \cdot 6H_2O$, and $MgSO_4 \cdot 7H_2O$ were among the identified phases that coexisted with high-pressure ice polymorphs. In-situ X-ray diffraction and Mössbauer spectroscopy were used to investigate the two endmembers and 10 intermediate compositions of the $FeSO_4 \cdot H_2O$-$CuSO_4 \cdot H_2O$ solid solution series (Giester, Lengauer, and Redhammer, 1994). At ambient conditions $CuSO_4 \cdot H_2O$ is triclinic (space group $P\bar{1}$). Giester, Lengauer, and Redhammer (1994) found that $FeSO_4 \cdot H_2O$-$CuSO_4 \cdot H_2O$ compositions with >20 mol% Cu are triclinic (space group $P\bar{1}$), distorted from the monoclinic (space group $C2/c$) structure of $FeSO_4 \cdot H_2O$. Additionally, the $FeSO_4 \cdot H_2O$-$MgSO_4 \cdot H_2O$ solid-solution series was examined under ambient and Martian surface temperature conditions using X-ray diffraction, Fourier transform infrared spectroscopy, and Raman spectroscopy (Talla and Wildner, 2019). Linear changes in lattice parameters, crystal structure, and the positions of absorption bands were observed as a function of Fe-content and deviated from linear behavior with decreasing temperature.

The pressure dependence of hydrated sulfate properties, in particular szomolnokite, has received less attention. Their stability at depth determines, in part, their volatile transport capabilities and geophysical behavior. For example, structural phase transitions influence the dynamics and seismic signatures within planetary interiors, especially for phase transitions exhibiting large volume changes. As an endmember hydrated sulfate, szomolnokite provides a means to study the effects of iron on phase stabilities and elastic properties, which are the focus of this study. Characterization of endmember species, like szomolnokite, under high-pressure conditions will help develop our understanding of the complex behavior of this class of minerals and their role in planetary interior environments.

In this study, we focus on the effect of pressure on the crystal structure of szomolnokite and associated elastic properties utilizing X-ray powder diffraction and synchrotron infrared spectroscopy. We present detailed analysis and equation of state fits of X-ray powder diffraction measurements conducted in the pressure range of 0-83 GPa. Within this pressure interval we find that the data are compatible with two different structural phase transitions. We term the high pressure phases β-Sz and γ-Sz. The phase transition from the $C2/c$ to $P\bar{1}$ space group (β-Sz) occurs between 5.0(1) and 6.6(1) GPa, and the transition from the $P\bar{1}$ to $P2_1$ space group (γ-Sz) occurs between 12.7(3) and 16.8(3) GPa, where the number in parentheses is the estimated pressure uncertainty for the last significant digit. Synchrotron infrared spectra reveal that for each phase transition, structurally bound H_2O is retained in the unit cell. We fit finite-strain equations of state to the data for each polymorph, compare against previous work, and present our new results on the γ-Sz phase.

2.2 Methods

Powdered szomolnokite was synthesized through collaboration with Isoflex ($FeSO_4 \cdot H_2O$, using 96% ^{57}Fe) and loaded into a symmetric diamond anvil cell (DAC) using a helium pressure medium to achieve hydrostatic pressure conditions. Diamond anvils (250 μm flat culet diameter, 300 μm bevel) were mounted on either a tungsten carbide seat (upstream side of the DAC) or a cubic boron nitride seat (downstream side of the DAC) to maximize the accessible 2θ range for X-ray diffraction measurements. Using an electric discharge machine, a 150 μm (diameter) hole was drilled into a pre-indented (50 μm thick) rhenium gasket, which served as the sample chamber. The powdered szomolnokite sample that was loaded had the approximate shape of a disk with the following dimensions: 85 μm in diameter and approximately 50 μm

thick, together with pressure gauges (one ruby sphere and a small amount of tungsten powder). Helium was loaded and sealed into the sample chamber, with a ruby fluorescence signal indicating a pressure of 0.44 GPa in the sample chamber. The sample chamber diameter decreased by ~20 μm immediately after helium loading at 0.44 GPa, and the approximate volume ratio of helium to sample and pressure gauges (tungsten powder and a ruby sphere) was ~3:1. In-situ pressure determination was achieved using X-ray diffraction (XRD) measurements of the tungsten powder at each compression point (Dorogokupets and Oganov, 2006). The tungsten and sample were not co-located, thus pressure determination and uncertainties were estimated by collecting an XRD pattern of the tungsten powder immediately before (and after) collecting an XRD pattern of the szomolnokite sample. The reported experiment pressure was taken to be the standard error of these two pressure measurements.

X-ray diffraction measurements were conducted at beamline 12.2.2 of the Advanced Light Source at Lawrence Berkeley National Laboratory up to 83 GPa at room temperature. An X-ray wavelength of 0.4972 Å and a beam size of 20 μm were used on a sample size of ~85 μm in diameter. Ambient pressure (1 bar) room-temperature measurements were performed on powdered szomolnokite in a Kapton tube. The sample-to-detector distance and tilt were calibrated using a CeO_2 standard. The integration of raw diffraction patterns was performed using the Dioptas software (Prescher and Prakapenka, 2015). Saturated regions and diamond reflections were manually masked for each XRD pattern in Dioptas before being exported to GSAS-II for Pawley refinement (Toby and Von Dreele, 2013; Prescher and Prakapenka, 2015). Although the observable 2θ range extends up to 28.7°, we restrict our refinement analysis to the range of $\sim 4 \leq 2\theta(^\circ) \leq 24$ to simplify background removal.

High-pressure synchrotron infrared compression and decompression measurements up to 24 GPa were conducted at beamline 22-IR-1 at the National Synchrotron Light Source II at Brookhaven National Laboratory. Powdered szomolnokite was loaded into a diamond anvil cell with a KBr pressure medium and ruby sphere for pressure determination. Synchrotron FTIR spectroscopic measurements were taken using a Bruker Vertex 80v FTIR spectrometer and a custom IR microscope system with a wide-band MCT detector from 400-5000 cm^{-1}.

Third-order Birch Murnaghan equation of state fits for each of the three structural polymorphs identified in this study were carried out using the MINUTI (MINeral physics UTIlities) open-source software (Sturhahn, 2020). Three approaches were

used to fit each of the polymorphs: (1) K_{T0}' was fixed and V_{T0} and K_{T0} were varied without the use of priors; (2) K_{T0}', V_{T0}, and K_{T0} were varied without priors; and (3) K_{T0}', V_0, and K_{T0} were all varied with priors. See Table 2.2 for select details on initial values and choice of prior values. The $C2/c$ and $P\bar{1}$ single crystal szomolnokite data of Meusburger, Ende, Talla, et al. (2019) were refit using the same procedure described above. This allows our work to be directly compared with the low-pressure polymorphs, including pressure-dependent error ellipses to visualize the correlation between V, K_T and K_T' for each fit result.

2.3 Results

Figure 2.1 presents select X-ray diffraction patterns with predicted reflections corresponding to each structural phase identified in this work. An overview of the full integrated diffraction pattern data set is displayed in the supplemental Figure S1. The $C2/c$ structure fits the XRD patterns from 0-5 GPa, after which a second-order structural phase transition occurs and the patterns are well described by the $P\bar{1}$ structure. Following the nomenclature used for the same $C2/c$ to $P\bar{1}$ transition for kieserite ($MgSO_4 \cdot H_2O$) (see Meusburger, Ende, Matzinger, et al., 2020), we term the $FeSO_4 \cdot H_2O$ $P\bar{1}$ structure β-Sz. Between 12.7(3)-16.8(3) GPa β-Sz undergoes a previously unknown transformation into a $P2_1$ structure, now termed γ-Sz, that fits the data until the last compression point measured at 83 GPa. See supplement Table S2 for the full set of refined lattice parameters resulting from Pawley refinement in GSAS-II. Figure 2.1 shows a schematic of the three unit cells associated with the $C2/c$, $P\bar{1}$, and $P2_1$ phases. See Figure S2 for the relative size and orientation of each cell. High-pressure FTIR measurements indicate retention of water and the strengthening of hydrogen bonds within the unit cell of each phase up to pressures of 24 GPa.

3.1 $C2/c$ to β-Sz $P\bar{1}$: 1 bar-12.7 GPa

The ambient pressure diffraction pattern was fitted using the lattice parameters and space group $C2/c$ reported from an earlier study on szomolnokite (Giester, Lengauer, and Redhammer, 1994; Meusburger, Ende, Talla, et al., 2019) as starting values in the refinement process. The ambient pressure lattice parameters derived in this work are generally in good agreement with those reported from recent XRD experiments, with the exception of those reported by Pistorius, 1960 Table (2.1). With increasing pressure, the space group $C2/c$ provides a good fit to the XRD patterns up to 5 GPa. After this pressure peak splitting is observed, and the patterns can no longer

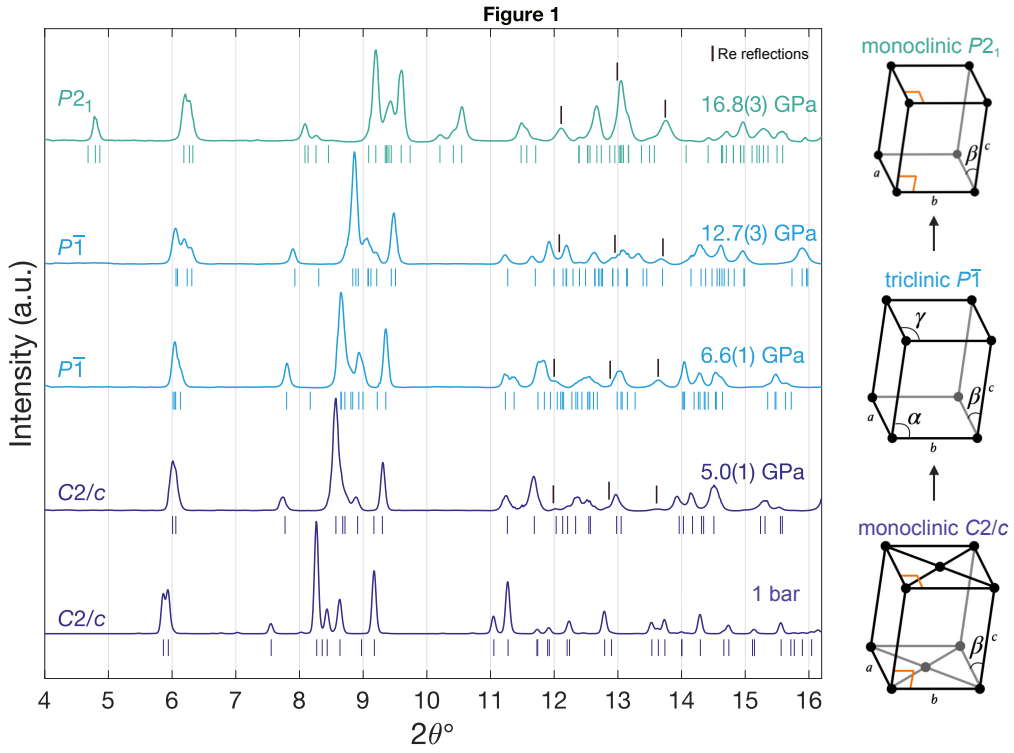

Figure 2.1: Integrated diffraction patterns at five selected compression points are plotted with a vertical offset: the ambient pressure pattern and the diffraction patterns before and after each structural phase transition. Each pattern has undergone background removal and the intensity of each pattern has been normalized for easier comparison between the different compression points such that the maximum value of each pattern is equal to one. Reflections for the crystal structures used to fit each pattern are plotted below each respective pattern. The phase transition from the $C2/c$ to $P\bar{1}$ space group occurs between 5.0(1) and 6.6(1) GPa, and the transition from the $P\bar{1}$ to $P2_1$ space group occurs between 12.7(3) and 16.8(3) GPa. The unit cell transformations are described schematically to the right of the diffraction patterns, see Figure S2 for relative cell size and orientation.

be fit using the predicted reflections for the monoclinic $C2/c$ structure. Using the cell-search capability in GSAS-II, selected crystal structures and space groups were tested in order to find the best-fit crystal structure model for the high-pressure phase. This analysis finds a structural phase transition occurring from the monoclinic $C2/c$ to triclinic $P\bar{1}$ structure between 5.0(1) and 6.6(1) GPa.

The XRD patterns collected from 6.6(1) GPa to 12.7(3) GPa are well described by the triclinic structure ($P\bar{1}$). The monoclinic-triclinic transition pressure interval in our study brackets the transition pressure reported from recent XRD measurements (Giester, Lengauer, and Redhammer, 1994; Meusburger, Ende, Talla, et al., 2019). Meusburger et al. (2019) performed single crystal XRD measurements on szomolnokite up to 9.2 GPa, finding a second-order, monoclinic-triclinic structural phase transition occurring between 5.951(5)-6.154(1) GPa. They identify distortion in the crystal lattice after the phase transition, which creates a second, distinct octahedral site within the crystal structure. A comparison between our low-pressure monoclinic and high-pressure triclinic (β-Sz) lattice parameters and those reported by Meusburger, Ende, Talla, et al., 2019 is shown in Figure 2.2. The structural parameters of β-Sz are transformed into the monoclinic $C2/c$ space group for both datasets to allow for easier comparison (see Giester, Lengauer, and Redhammer (1994) for details of this transformation).

The unit cell volume values agree well with the single crystal data at all overlapping pressures with more deviation occurring between the reported lattice parameters. The a-parameter agrees well up to ~2 GPa, where it begins to deviate (up to ~0.06 Å difference) and follows a steeper pressure-dependence trend compared to Meusburger, Ende, Talla, et al. (2019). The b-parameter in both studies follow the same general trend, but in our work it appears to decrease linearly versus parabolically in the $C2/c$ phase. In the β-Sz phase the differences between b-parameters increases by approximately double (from ~0.01 Å to ~0.02 Å) with increasing pressure. Our values are higher than the single crystal work and further diverge as pressure increases. The c-parameter in both studies agrees the best out of the three unit cell lengths up to 6.6 GPa, just past the β-Sz phase transition. After this pressure our c-parameter values trend lower than the single crystal work and intersect the b-parameter at ~8.8 GPa. The b and c parameters as reported by Meusburger, Ende, Talla, et al. (2019) indicate they would also intersect, but at higher pressures than our data. Axial ratio trends for unit cell lengths a, b, and c are plotted in supplemental Figure S3.

The unit cell angles α, β, and γ across the entire pressure range of this work together

Table 2. Equation of state fit parameters and results.

Phase	V_0 (Å3)	K_0 (GPa)	K_{0T}'	χ^2
Szomolnokite ($FeSO_4 \cdot H_2O$) *C*2/*c*				
Fixed: K_{0T}'	[365.23 0.30]	[45.2 5]	[6.7]	0.93
Fit: V_0, K_0	365.13(2)	45.2(4)		
Fit: V_0, K_0, K_{0T}'	[365.23 0.30]	[45.2 5]	[6.7 2]	0.65
	365.14(2)	44.5(5)	7.5(5)	
Refit of published data	[365.23 0.30]	[45.2 5]	[6.7 2]	0.53^a
Fit: V_0, K_0, K_{0T}'	365.23(2)[a]	45.2(2)[a]	6.8(1)[a]	0.53^b
	365.2(3)[b]	45.2(2)[b]	6.7(1)[b]	
Szomolnokite ($FeSO_4 \cdot H_2O$) *P*$\bar{1}$				
Fixed: K_{0T}'	[367 0.4]	[45.11 5]	[5.4]	0.14
Fit: V_0, K_0	367.02(9)	45.5(2)		
Fit: V_0, K_0, K_{0T}'	[367 0.4]	[45.11 5]	[5.4 2]	0.09
	367.02(9)	46.3(6)	5.1(2)	
Refit of published data	[367 0.4]	[45.11 5]	[5.4 2]	1.72^a
Fit: V_0, K_0, K_{0T}'	367.0(4)[a]	45(1)[a]	5.4(2)[a]	0.93^b
	367.0(4)[b]	45.1(6)[b]	5.4 (fixed)[b]	
Szomolnokite ($FeSO_4 \cdot H_2O$) *P*2_1				
Fit: V_0, K_0, K_{0T}'	[365 15]	[45 5]	[5.4 2]	1.03
	357(2)	44(2)	5.8(1)	
Kieserite ($MgSO_4 \cdot H_2O$): *C*2/c and *P*$\bar{1}$				
*C*2/c	[355.5 0.4]	[48.1 2]	[8.1 2]	0.63^c
Refit of published data	355.5(3)[c]	48.5(5)[c]	7.8(5)[c]	0.60^d
Fit: V_0, K_0, K_{0T}'	355.5(4)[d]	48.1(5)[d]	8.1(6)[d]	
P$\bar{1}$	[355.8 0.4]	[49.3 2]	[4.8 2]	1.01^c
Refit of published data	355.8(2)[c]	49.3(6)[c]	4.8(1)[c]	1.14^d
Fit: V_0, K_0, K_{0T}'	356(2)[d]	49(6)[d]	5(1)[d]	
Blödite ($Na_2Mg(SO_4)_2 \cdot 4H_2O$)				
P2_1/*a*	[496.6 0.4]	[36 2]	[5.1 2]	4.82
Refit of published data	496.5(2)[e]	36.0(7)[e]	5.1(2)[e]	[f] Not Reported
Fit: V_0, K_0, K_{0T}'	496.9(7)[f]	36(1)[f]	5.1(4)[f]	

Table 2.2: Equation of state fit parameters and results.

Notes: notation explanation for columns V_0, K_0, K_{0T}', [A B] X(Y): starting value of A with a prior window of B, and best fit value of X with an error of Y. [A]: fixed parameter at value of A.

[a] This work's results from re-fitting the data of Meusburger, Ende, Talla, et al. (2019).

[b] As-reported results in Meusburger, Ende, Talla, et al. (2019).

[c] This work's results from re-fitting the data of Meusburger, Ende, Matzinger, et al. (2020).

[d] As-reported results in Meusburger, Ende, Matzinger, et al. (2020).

[e] As-reported results in Meusburger, Ende, Matzinger, et al. (2020).

This work's results from re-fitting the data of Comodi et al. (2014).

[d] As-reported results in Meusburger, Ende, Matzinger, et al. (2020).

[f] As-reported results in Comodi et al. (2014).

with the parameters reported by Meusburger, Ende, Talla, et al. (2019) are shown in panels (b) and (c) of Figure 2.2. The α and γ angles in the $C2/c$ and β-Sz phase are fixed at 90°, characteristic of the monoclinic structure. For easier comparison between the three phases, the β-Sz data are transformed into the monoclinic setting using the cell transformation tool in GSAS-II, using the transformation matrix as described in Giester, Lengauer, and Redhammer (1994). The transformation provides a description of the cell in the monoclinic structure by allowing the α and γ angles to be approximately 90°. Lattice parameters in the $P\bar{1}$ space group are reported in Table S3. For both our data and the transformed $P\bar{1}$ data reported by Meusburger, Ende, Talla, et al. (2019) α remains approximately constant, with our values scattering around 90°, while γ increases by ~2° throughout the β-Sz stability field.

γ-Sz

$P2_1$: 16.8-83 GPa

At 16.8 GPa, the $P\bar{1}$ space group cannot describe the XRD pattern due to the appearance of intense peaks where no $P\bar{1}$ reflections are predicted (e.g., at ~10.5 ° 2θ), and the disappearance or merging of triclinic-assigned peaks (see Figure S4 for reflections predicted by the $P\bar{1}$ space group at 16.8 GPa). These significant changes in the pattern at 16.8(3) GPa indicate the likelihood that a structural phase transition is occurring. A cell-search was again performed in order to find the best-fit crystal structure and space group. The results of this search indicated that at 16.8(3) GPa, β-Sz undergoes a phase transition from triclinic $P\bar{1}$ to a primitive monoclinic lattice. We select $P2_1$ as the best-fitting space group (see discussion below), and term this new phase γ-Sz. Upon further compression, the XRD data are compatible with the $P2_1$ structure up to the highest pressure in this study, 83 GPa. Figure 2.1 displays selected X-ray diffraction patterns highlighting the ambient pressure pattern and the two structural phase transitions occurring between 5.0(1)-6.6(1) GPa and 12.7(3)-16.8(3) GPa.

At 16.8(3) GPa, there are several new reflections with a larger $\partial(2\theta)/\partial P$ compared to other reflections. These reflections cannot be attributed to other materials in the sample chamber (W, Al_2O_3, He, or Re). The decomposition of β-Sz was considered, but these additional reflections cannot be attributed to H_2O ice VI-VIII, Fe_2O_3, or other iron sulfate/hydroxyl mixtures. However, direct comparison of various iron sulfate/hydroxyl mixtures at these experimental pressures is difficult without available high-pressure XRD data for such phases. In Figure S4 we demonstrate that

the theoretical high-pressure phase of SO_2 does not account for the new reflections (Zhang, Tóth, et al., 2020). While this is not an exhaustive list of possible phases, the shift of the additional reflections as a function of pressure is well-described by a primitive monoclinic space group and thus we do not attribute these new reflections to a separate phase.

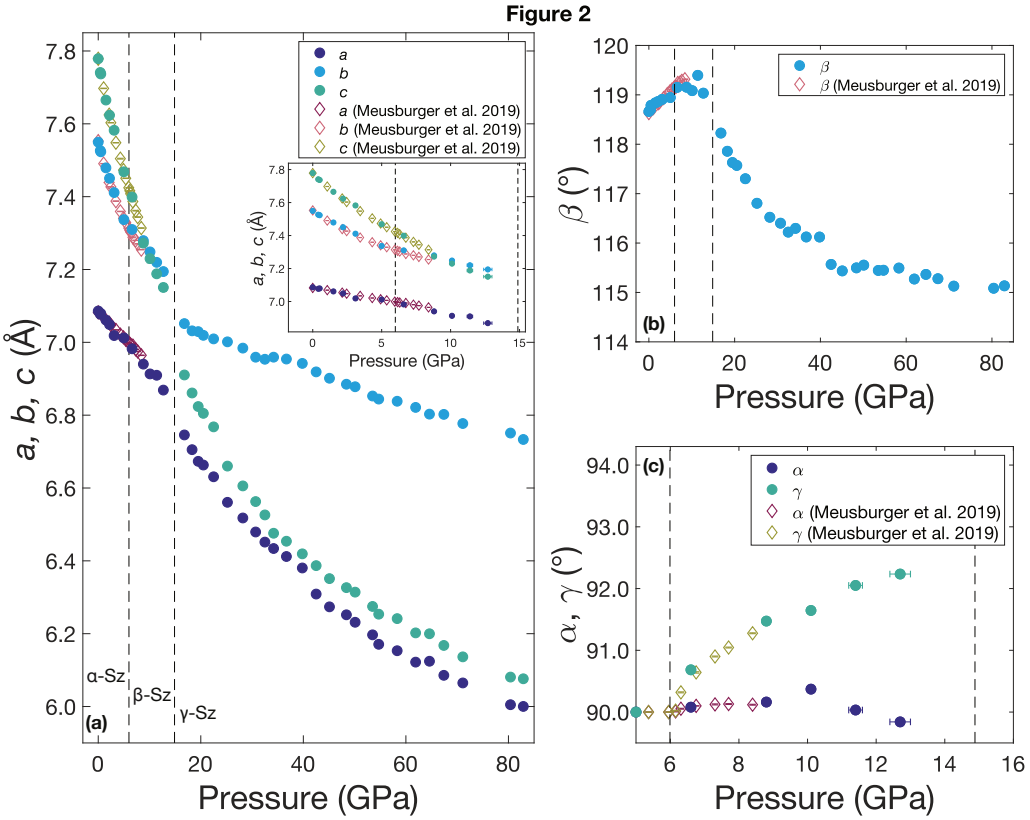

Figure 2.2: The lattice parameters determined from this work are plotted as a function of pressure: **(a)** *a, b, c*, **(b)** β, **(c)** α and γ. Lattice parameters reported by Meusburger, Ende, Talla, et al., 2019 up to 9.2 GPa are also plotted for comparison. Dashed lines indicate the $C2/c$ to $P\bar{1}$ (between 5.0(1) and 6.6(1) GPa) and $P\bar{1}$ to $P2_1$ (between 12.7(3) and 16.8(3) GPa) structural transitions. Lattice parameters for the $P\bar{1}$ cell have been transformed into the monoclinic setting for easier comparison across the dataset.

This work tested many possible crystal structures and space groups in order to identify the best-fitting structural model to the γ-Sz phase transition at 16.8(3) GPa. The $P\bar{1}$ and $P1$ space groups do not account for several peak positions in the γ-Sz phase, including the complete absence of the cluster of peaks between 10 ° and 11 ° 2θ. A triclinic cell with a larger unit cell volume compared to the last-calculated $C2/c$ volume could be a possible solution, but due to the inability to extract atomic positions

within the unit cell and choose a cell with consistent density relative to β-Sz, we do not consider triclinic cells as candidate structures. Nevertheless, the data is well-fit by a primitive monoclinic structure of comparable size to the monoclinic-setting β-Sz unit cell and thus exhibits reflections that can be attributed to a higher symmetry phase.

Supplemental figures S5 and S6 plots reflections for the $C2/m$ (Figure S5 only), $P2_1$, $P2_1/m$, $P2/m$, $P2/c$, $P2_1/c$, $P2$, Pm, and Pc groups resulting from Pawley refinement fits at 16.8 and 67.4 GPa. Face-centered monoclinic structures do not fit the data, as seen in Figure S5 with the example of the $C2/m$ space group, thus only primitive monoclinic structures were examined in detail. The eight monoclinic-P space groups tested here all exhibit almost identical reflection sets except for a few reflection regions located at ~5 °, ~8.45 °, ~12.15 °, ~14.1 °, ~20.3 ° 2θ at 16.8 GPa. The peaks present at ~12.15 ° and ~14.1 ° 2θ for space groups such as Pm and $P2/c$ additionally overlap with Re peaks from the strained gasket detected by tails of the X-ray focused beam. Figure S5 contains a caked diffraction image at 16.8 GPa zoomed into the 2θ region containing two Re peaks at ~12.15 ° and ~14.1 ° 2θ. The Re peaks are diffuse and the image does not indicate presence of overlapping szomolnokite reflections. For this reason, only space groups *without* reflections overlapping with the ~12.15 ° 2θ Re peak were considered: $P2_1$, $P2_1/m$, $P2/m$, and $P2_1/c$.

Upon increasing pressure it is clear that more than one reflection is needed to fit the peaks at ~5.1 ° 2θ and ~9.4 ° 2θ, which only includes the $P2_1$, $P2_1/m$, and $P2/m$ space groups, which are almost identical. With the broad and overlapping nature of the peaks characteristic of high-pressure powder data, it is difficult to make any further distinction based on the quality of fits (see Figure S7 for R_w discussion). Out of these three space groups, the $P2_1$ phase is chosen as the reported space group due to it being the lowest symmetry. However, we fit the entire γ-Sz pressure region with both the $P2_1$ and $P2/m$ space groups and find that the resulting equation of state parameters are the same within error. Lattice parameters for all space groups fit are given in Table S1, S2, S3. We stress that the γ-Sz phase may be attributed to several primitive monoclinic space groups, and although we choose the $P2_1$ space group for discussion within this manuscript, future work is needed to accurately determine the atomic positions within the unit cell of γ-Sz and allow for selection of a unique space group.

The stability of γ-Sz and the retention of H_2O within its crystal structure after the high-pressure phase transition is further supported by high-pressure synchrotron in-

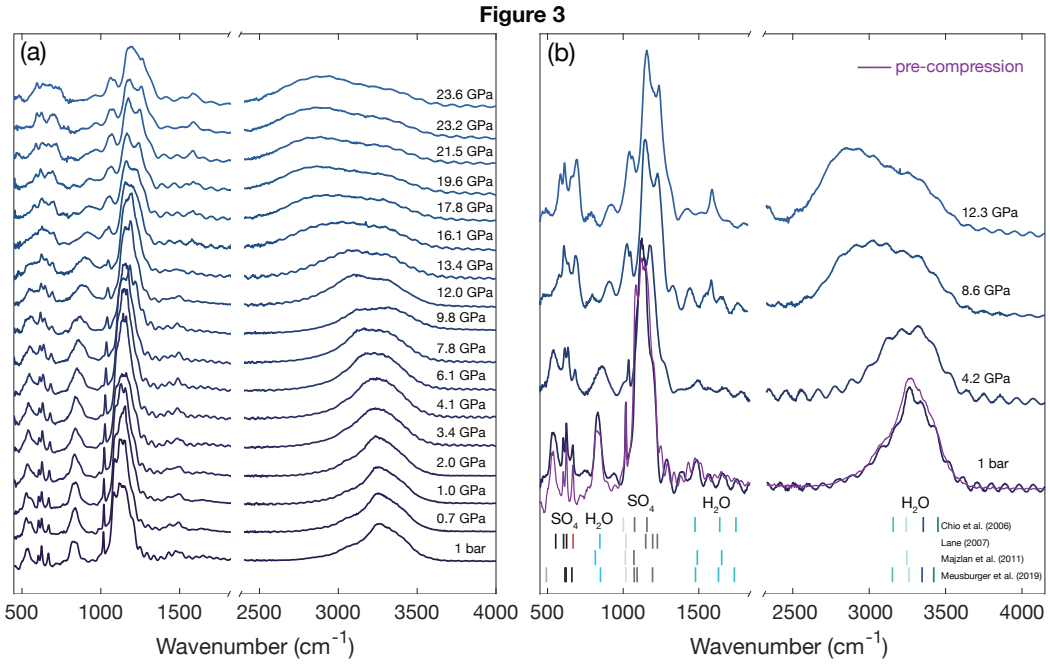

Figure 2.3: High pressure infrared spectra. Panel **(a)** plots infrared spectra for the 17 compression points up to 24 GPa. Pressure-dependent shift of the H_2O bands initially centered around 3200 cm^{-1} at 1 bar towards lower wavenumbers with increasing pressure indicates increased hydrogen bonding within the crystal structure. Panel **(b)** plots the four decompression measurements. The pre-compression 1 bar pattern is also plotted against the post-decompression 1 bar pattern for comparison. The bottom of panel **(b)** plots assigned bands as reported by their four respective studies. The high-frequency noise present in all spectra is due to interference from the diamond anvils within the sample chamber.

frared measurements. Figure 2.3 displays measured FTIR spectra in the frequency range of 500-4000 cm^{-1} of 17 compression measurements up to 24 GPa and four decompression measurements. Assigned SO_4^{2-} and H_2O bands from several infrared spectroscopy measurements on szomolnokite are plotted at the bottom of the right panel in Figure 2.3 (Chio, Sharma, and Muenow, 2007; Lane, 2007; Majzlan et al., 2011; Meusburger, Ende, Talla, et al., 2019). Spectral features indicate increased hydrogen bonding environments and strength in the crystal structure due to the broadening and pressure-dependent shift of H_2O bands in the ~3000 cm^{-1} range towards lower wavenumbers with increasing pressure. The shift towards lower wavenumbers, combined with increasingly broadened H_2O bands without addition of new spectral features in the ~3000 cm^{-1} region with increasing pressure does not indicate addition of H_2O groups into the unit cell, suggesting that the monohydrated structure is the most stable at high pressure. Upon decompression, all bands in the spectra re-

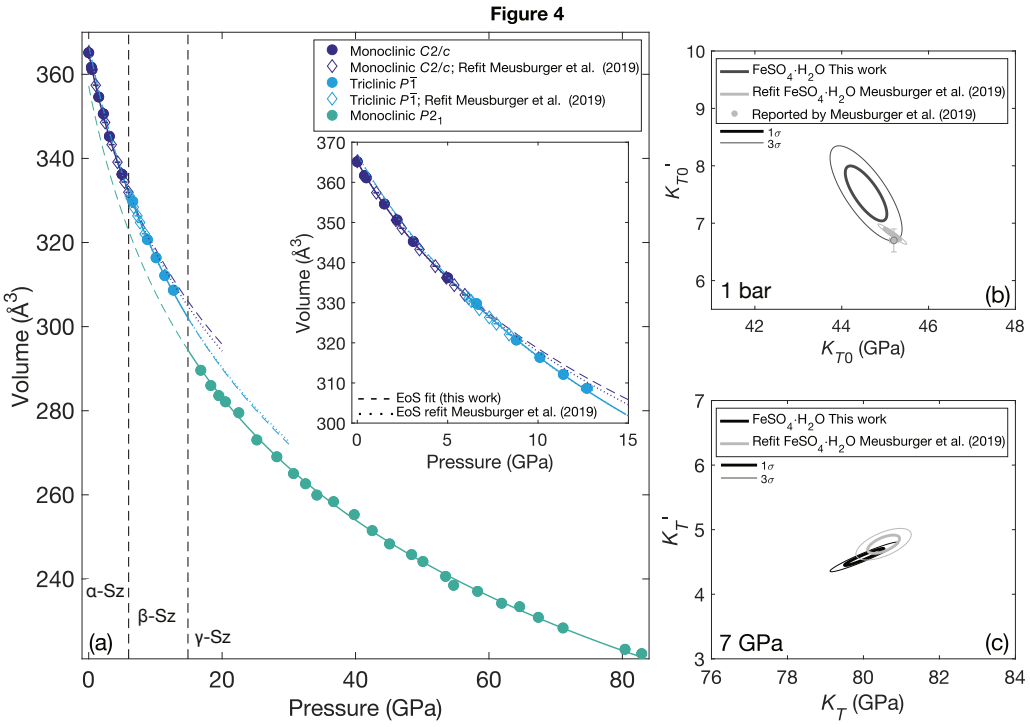

Figure 2.4: Volume data with equation of state fits for the three $C2/c$, $P\bar{1}$, and $P2_1$ phases are plotted in panel **(a)** for this study (solid circles, dashed lines) and the re-fits of the single crystal study for the $C2/c$ and $P\bar{1}$ phases (open diamonds, dotted lines). Volume measurements for these two phases match well between these two studies. Our work extends the $P\bar{1}$ stability field until at least 12.7(3) GPa. 1σ and 3σ error ellipses are plotted in panel **(b)** K_{T0}' vs. K_{T0} error ellipse at 1 bar, in addition to reported values by Meusburger, Ende, Talla, et al. (2019), and panel **(c)** K_T' vs. K_T at 7 GPa for our data and refit of Meusburger, Ende, Talla, et al. (2019).

turn to the same wavenumber positions and relative intensities measured at ambient pressure prior to compression.

The β-Sz $P\bar{1}$ to γ-Sz $P2_1$ transition exhibits a noticeable volume drop (~6% decrease over a ~4 GPa pressure interval, see Figure 2.4). The volume drop is characterized by a sharp decrease in the c-axis unit cell length (0.25 Å), and moderate drops in the a- and b-axis lengths (0.12 and 0.14 Å, respectively) over the ~4 GPa interval bracketing the phase transition. At higher pressures, the β angle begins to decrease and continues until ~45 GPa. At this pressure, the β angle plateaus until the last compression point. The β angle decreases from 118.2° to 114.8° from the start of the γ-Sz phase transition at 16.8(3) GPa to the last measured compression point at 83 GPa. Over the γ-Sz pressure range the a and c axis lengths compress at approximately the same rate beginning at ~45 GPa, corresponding with the plateauing of

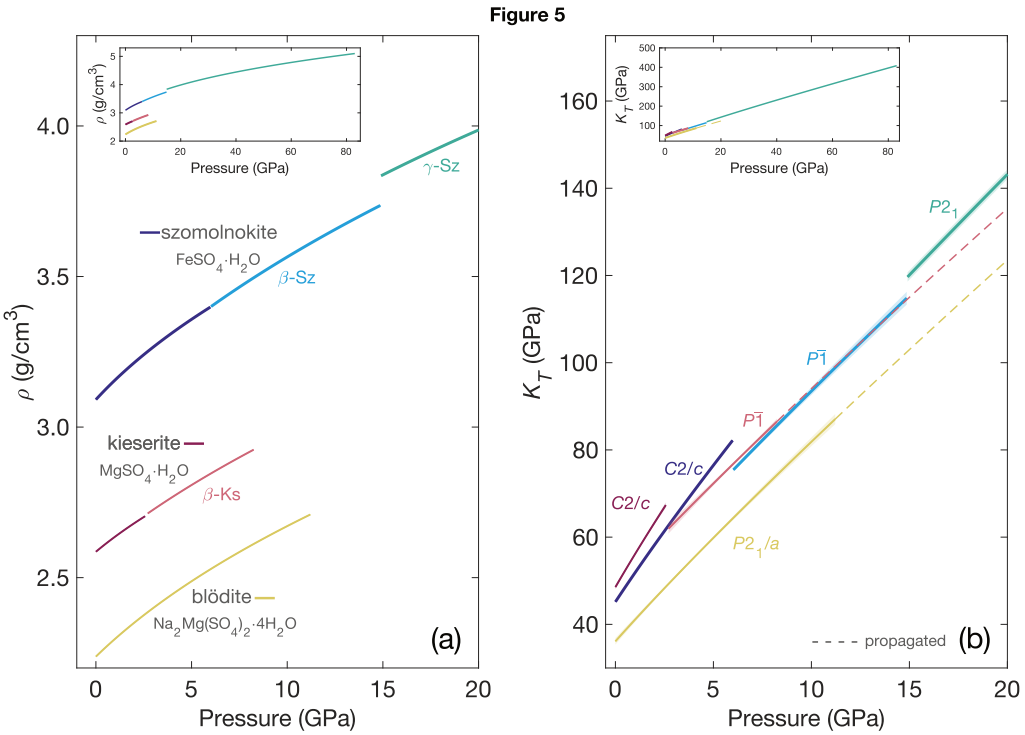

Figure 2.5: Calculated densities output by MINUTI for szomolnokite, kieserite, and blödite and their respective high-pressure phases. The high-pressure polymorphs of szomolnokite and kieserite are plotted as different colors (blue and green for szomolnokite, pale red for kieserite). **(b)** MINUTI results for the bulk modulus K_T as a function of pressure are plotted for szomolnokite, kieserite, and blödite and their respective high-pressure phases. Space groups for each polymorph are indicated by adjacent color-coded labels. Errors are reported as the shaded regions, most visible in the γ-Sz $P2_1$ phase. Dashed lines indicate extrapolation above previously reported experimental pressures. It is unknown if β-Ks and blödite undergo phase transitions above 8.3 and 11.2 GPa, respectively.

the β angle. This behavior may occur over the pressure range in which the Fe atoms undergo a broad spin transition between 45 and 95 GPa. See Perez et al. (2020) for further discussion regarding spin transition models for szomolnokite and its high-pressure phases.

2.4 Equations of state

Equation of state (EoS) fits from MINUTI using priors and pressure-volume data for szomolnokite and its β-Sz and γ-Sz high-pressure polymorphs are presented in Figure 2.4a. We compare our re-fit of the single-crystal data from Meusburger, Ende, Talla, et al. (2019) for the $C2/c$ and β-Sz $P\bar{1}$ phases. We find that extremely small

differences in volume measurements, most likely due to experimental conditions, combined with small volume-error values, produces EoS fit results with statistically different V_0 values (see supplemental Figures S8, S9, S10 for K_T-V_T error ellipses for each phase). Error ellipses provide a valuable method for visualizing the uncertainty and correlation between model parameters in an EoS fit. Figure 2.4b and 4c plot K_T'-K_T at 1 bar and 7 GPa. Error ellipses for our re-fit results of Meusburger, Ende, Talla, et al., 2019 along with their reported EoS fit values at 1 bar are also plotted. We find that for the $C2/c$ phase at 1 bar both studies exhibit a strong negative correlation between K_T' and K_T, but these parameters are positively correlated by 7 GPa in the β-Sz phase.

EoS model parameters are commonly reported at 1 bar, regardless if the data are representative of phases whose stability fields only exist at high pressure. In this work, we demonstrate the importance of comparing the elastic properties of high-pressure phases within their respective stability fields. In supplemental Figure S11 we plot our re-fit K_T vs. K_T' error ellipse results for the Mg-hydrated sulfate end-member kieserite ($Mg(SO_4)\cdot H_2O$) using volume values reported from single-crystal XRD data (Meusburger, Ende, Matzinger, et al., 2020), and a re-fit of a single-crystal XRD volume measurements of blödite ($Na_2Mg(SO_4)_2\cdot 4H_2O$) (Comodi et al., 2014), a candidate Na-bearing mineral modeled on the surface of Europa (Dalton, Shirley, and Kamp, 2012). We find that at ambient pressure, szomolnokite is less compressible than blödite, but more than kieserite. However, by 7 GPa, both szomolnokite and kieserite have undergone $C2/c$ to $P\bar{1}$ structural transitions (into the β-Sz and β-Ks phases, respectively) and have approximately the same bulk modulus value, while blödite remains lower than both phases up to 20 GPa. Figure 2.5 plots K_T and density as a function of pressure for szomolnokite, kieserite, blödite, and their respective high-pressure phases resulting from our MINUTI EoS fits and re-fits.

Even though β-Ks and β-Sz display similar incompressibilities around 10 GPa, kieserite and β-Ks are much lower in density (Figure 2.5). Szomolnokite exhibits a slight density increase across the β-Sz transition, but undergoes a sharp increase in density across the γ-Sz transition. Blödite is significantly lower in density than both phases which is accompanied by its lower bulk modulus across this entire pressure range. It was not observed to undergo a phase transition from its ambient pressure monoclinic $P2_1/a$ structure up to 11.2 GPa and retains water within the unit cell, exhibiting increased hydrogen bonding with increasing pressure (Comodi et al., 2014).

2.5 Implications

Surface measurements and observations of icy satellites in the solar system indicate an abundance of hydrated sulfates on Europa, Ganymede, and Callisto (Dalton, Shirley, and Kamp, 2012; Hibbitts et al., 2019; Cartwright et al., 2020). The relative exogenic vs. endogenic origins of these surface sulfur-bearing ice and salt phases is unclear (Trumbo, Brown, and Hand, 2020), but even a purely exogenic sulfur origin could result in subsequent sulfur cycling due to exchange between the icy crust and underlying interior (Vu et al., 2020). The stability and elastic properties of szomolnokite and related phases discussed in this work imply complex pressure and chemical-dependent behavior, and thus potentially important factors for icy satellite interiors. Within the high-pressure triclinic stability field, β-Sz and β-Ks exhibit equal incompressibility with drastically different density, while the addition of Fe into Mg-bearing hydrated sulfates may affect the elastic parameters and increase the depth at which the monoclinic-triclinic transition occurs within sulfate-bearing icy mantles. For smaller icy satellites, where mantle pressures are less than 5 GPa, this transition may not occur at all.

If β-Sz retains its water after the γ-Sz structural transition, as our preliminary FTIR data indicate, the stability of this new high-pressure phase to pressures of at least 83 GPa could have implications for its ability to retain water in planetary deep interiors. However, other obvious factors such as temperature and co-existing phases, would affect this behavior and are largely unexplored. For example, incorporating Mg into the crystal structure could significantly lower the β-phase transition pressure (Meusburger, Ende, Matzinger, et al., 2020) and also affect water retention. In particular, future work investigating the effect of temperature on the structural behavior of szomolnokite, its high-pressure β-Sz and γ-Sz phase transitions, and other co-existing and/or hydrous sulfates will deepen our understanding of their ability to retain water at conditions most relevant to icy satellite or terrestrial-type planetary interiors. Future work investigating the electronic and vibrational properties of szomolnokite will further broaden our understanding of the Fe-endmember hydrated sulfate. Such data, including the work presented here, are needed to conduct more complex phase equilibria modeling for planetary interiors in which hydrous sulfates are proposed to exist.

Chapter 3

LATTICE DYNAMICS, SOUND VELOCITIES, AND ATOMIC ENVIRONMENTS OF SZOMOLNOKITE AT HIGH PRESSURE

**This chapter is currently in review and available online:*
Olivia S. Pardo, Vasilije V. Dobrosavljevic, Wolfgang Sturhahn, Thomas S. Toellner, Benjamin Strozewski, Jennifer M. Jackson (May 1, 2023). Lattice dynamics, sound velocities, and atomic environments of szomolnokite at high pressure. preprint. In Review. DOI: 10.21203/rs.3.rs-2861032/v1

3.1 Introduction

Sulfates in planetary environments

Complex chemical mixtures comprised of hydrous sulfates and other sulfate salts are found in natural environments throughout the solar system. These sulfates can host a variety of cations, such as Fe, Cu, Mn, and Al, and varying amounts of molecular water and hydroxyl groups. Sulfate cations can be of mixed valence states, and sulfate minerals with different cation valence states can coexist depending on the degree of weathering. These sulfates may be produced by surface weathering of pyrite or pyrrhotite and may be further altered on short timescales (hours to days) (McCollom et al., 2013; Wang, Jolliff, et al., 2016). Because of the many hydrous sulfates found in close proximity to each other, interpretation of remote observations of Mars, the icy satellites, and other planetary bodies has focused on suggesting possible mixtures that reproduce observed spectral features (Lane, Dyar, and Bishop, 2004; Bishop, Parente, and Weitz, 2009; Lichtenberg et al., 2010; Dalton, Shirley, and Kamp, 2012; Bu et al., 2018).

For Mars in particular, these measurements have led to the identification of the iron end-member szomolnokite ($FeSO_4 \cdot H_2O$), amongst other mono- and poly-hydrated sulfates across the planet (Wang, Haskin, et al., 2006; Bishop, Parente, and Weitz,

2009; King and McLennan 2010; Wendt et al., 2011; Chou, Seal, and Wang, 2013; Singh et al., 2022). The abundance of sulfur on the surface and exposed subsurface of Mars combined with Martian meteorite analysis suggests a S-rich Martian mantle and core (Gaillard and Scaillet, 2009; Franz, King, and Gaillard, 2019); therefore the observed sulfate phases may play (or have played) a larger role in interior sulfur and water cycling compared to Earth. In subduction zone environments on Earth, sulfur-bearing phases have been suggested as minor but important mantle components of the Earth's volatile cycling system (McCanta, Dyar, and Treiman, 2014; Bataleva, Palyanov, and Borzdov, 2018; Bénard et al., 2018; Schwarzenbach et al., 2018; Li et al., 2021).

Due to the abundance of sulfur on the surface of the icy satellites and spectral observations, it has been proposed that hydrated sulfates are primary components of their interior oceans and/or icy mantles and has motivated work on hydrous sulfates at high pressures (Fortes, Wood, Alfredsson, et al., 2006; Fortes, Brand, et al., 2013; Fortes, Fernandez-Alonso, et al., 2017; Nakamura and Ohtani, 2011; Dalton, Shirley, and Kamp, 2012; Comodi et al., 2014; Pan, Yong, and Secco, 2020). Recent work has suggested a primarily exogenic sulfur source for the surfaces of Io, Europa, and Ganymede (e.g., Trumbo, Brown, and Hand, 2020). For Europa in particular, sulfur radiolytic chemistry resulting from sulfur implantation due to volcanic activity on Io is thought to be one of the main causes for the difference in color and spectral features of Europa's trailing hemisphere. Current work suggests endogenic surface material alteration by exogenic sulfur radiolysis (Trumbo, Brown, and Hand, 2020). Therefore, surface-subsurface exchange is possible within these dynamic planetary bodies (Prockter et al., 2017; Buffo et al., 2020), and the observed abundance of Mg- and Na-bearing hydrated sulfates on their surfaces may be indicative of their presence at depth (Zolotov, 2019). Given the propensity of these sulfates to host multiple cations, Fe-bearing compositions may be present at greater depths, especially where leaching of chondritic sulfates from an iron-rich core into an overlying rocky, icy, or mixed ice-rock mantle may have occurred (Kargel, 1991). On Ganymede, rocky materials and precipitating salts in the icy crust and ocean should sink towards the basal ice layer and rocky mantle, potentially bringing sulfur-bearing phases from the surface to the ice-rock interface (Vance et al., 2014; Ligier et al., 2019; Molyneux et al., 2020). Internal heating could melt the ice at this interface and cause fluid-rock interactions (Ahrens et al., 2022).

The ability for sulfates to host multiple cations in solid solution and the multi-mineral nature of these natural systems containing hydrous sulfates necessitates better chemical and physical characterization of the endmembers. Whether these sulfates act as components in a localized volatile cycling system, or as major planetary interior phases, high pressure data is needed to better model these environments. In this work we present nuclear resonant scattering results that characterize the electronic and vibrational properties of szomolnokite ($FeSO_4 \cdot H_2O$) in response to compression.

Nuclear resonant scattering measurements

Nuclear resonant scattering techniques rely on achieving nuclear resonance with a participating atom in the material of interest. In these experiments, we achieve resonance with the nuclei of ^{57}Fe atoms (14.4125 keV) within the szomolnokite sample and conduct both nuclear resonant forward scattering, also known as synchrotron Mössbauer spectroscopy, and nuclear resonant inelastic X-ray scattering (NRIXS) experiments. Both methods utilize time and energy discrimination to excite the resonant nuclei (Toellner, 2000). Synchrotron Mössbauer spectroscopy (SMS) detects photons emitted from micro-eV scale features originating from splitting of the iron atoms' nuclear energy levels, while NRIXS detects emission from meV-scale features originating from simultaneous excitation of the iron atoms and, in the case of crystalline materials, lattice vibrations (phonon excitations) that quantify the dynamics of the crystal lattice.

In particular, SMS provides access to the hyperfine structure of the iron components in the sample, including quadrupole splitting, isomer shift, and relative weight fractions of distinct iron sites, as well as the Lamb-Mössbauer factor (e.g., Jackson, Hamecher, and Sturhahn, 2009; Zhang, Jackson, et al., 2022). The Lamb-Mössbauer factor is, however, more accurately determined by NRIXS via the 0^{th} order moment of the excitation probability density and the partial projected phonon density of states (pPDOS) (Sturhahn, 2004). In this work, we determine the Lamb-Mössbauer factor at each measured pressure from the NRIXS spectra, which provides tighter constraints on the resulting hyperfine parameters determined from SMS spectral fits (discussed in section 4). Additional properties of the iron sub-lattice can be determined from higher order moments of the data and the pPDOS, such as the mean force constant of the iron atoms and Debye velocity. When combined with the equation of state determined for the high-pressure polymorphs of szomolnokite

(Pardo, Dobrosavljevic, Perez, et al., 2023), the shear wave velocities (V_S) and moduli (Ks, G) can be constrained (Sturhahn and Jackson 2007).

Together, the SMS and NRIXS results contribute to a more detailed understanding of the micro- and macroscopic properties of the iron endmember szomolnokite, which will aid in future models containing complex mixtures of endmember sulfates.

Previous work

Much of the published work on hydrous sulfates has focused on ambient pressure and variable temperature with relevance to interpreting remote observations on planetary surfaces, while relatively fewer studies have characterized high-pressure behavior. Two structural transitions in $FeSO_4{\cdot}H_2O$ were identified with powder X-ray diffraction occurring below 20 GPa with complementary infrared spectroscopy measurements indicating the retention of water across both phase transitions (Pardo, Dobrosavljevic, Perez, et al., 2023). The α-β transition was bracketed between 5-6.6 GPa (monoclinic $C2/c$ to triclinic $P\bar{1}$) and the β-γ transition was bracketed between 12.7-16.8 GPa (triclinic $P\bar{1}$ to monoclinic $P2_1$). The low-pressure α-β monoclinic-triclinic transition was identified with single crystal X-ray diffraction measurements at 6.15 GPa and characterized by a slight distortion in the Fe-octahedra (Meusburger, Ende, Talla, et al., 2019). An analogous $C2/c$ to $P\bar{1}$ transition in the Mg-endmember $MgSO_4{\cdot}H_2O$ was observed at lower pressures than in $FeSO_4{\cdot}H_2O$ and remains in the β-phase through the highest pressure achieved in the experiment (~8 GPa) (Meusburger, Ende, Matzinger, et al., 2020). Additionally, the Ni-endmember dworkinite $NiSO_4{\cdot}H_2O$ and Co-endmember $CoSO_4{\cdot}H_2O$ exhibit a similar low-pressure transition ($C2/c$ to $P\bar{1}$) at 2.47 GPa and 2.40 GPa, respectively (Ende et al., 2020; Wildner, Ende, et al., 2021). The deuterated analog of meridianiite $MgSO_4{\cdot}11D_2O$ was studied up to 1 GPa with neutron powder diffraction by Fortes, Fernandez-Alonso, et al., 2017, who observed a structural phase transition and decomposition of $MgSO_4{\cdot}11D_2O$ ($P\bar{1}$) to $MgSO_4{\cdot}9D_2O$ (orthorhombic Pc) + ice VI occurring at 0.9 GPa and 240 K. $MgSO_4{\cdot}H_2O$, $MgSO_4{\cdot}6H_2O$, and $MgSO_4{\cdot}7H_2O$ were among several phases found to coexist with ice at pressures up to 4.5 GPa (Nakamura and Ohtani, 2011).

$FeSO_4{\cdot}H_2O$ was investigated up to pressures of 95 GPa with synchrotron Mössbauer spectroscopy (SMS), which resulted in three possible models for pressures above 20 GPa, two of which included the occurrence of a high- to low-spin transition (Perez et al., 2020). SMS has also been used to observe the pressure dependence of mag-

netic ordering for jarosite $KFe_3(OH)_6(SO_4)_2$ up to 40 GPa (Klein et al., 2018). The majority of existing conventional and synchrotron Mössbauer data for hydrous sulfates focuses on ambient pressure, including a suite of measurements consisting of 47 natural and synthetic sulfate species (Dyar et al., 2013), five ferrous and ferric natural sulfate compositions (Majzlan et al., 2011), characterization of both ferrous and ferric amorphous sulfates (Sklute et al., 2015), and identification of magnetic order-disorder transition in $FeSO_4 \cdot H_2O$ at 30 K (Alboom et al., 2009).

Even fewer studies have taken advantage of NRIXS to study the lattice dynamics of hydrous sulfates (Dauphas, Roskosz, Alp, Golden, et al., 2012, 2014; Roskosz et al., 2022). To the authors' knowledge the presented work is the first NRIXS study of a hydrous sulfate at high pressure. In this study, we describe the high-pressure evolution of szomolnokite's electronic and vibrational properties including the Fe-site quadrupole splitting, the Lamb-Mössbauer factor, the ^{57}Fe mean force constant, wave speeds and shear elasticity, thus spanning scales from atomic environments to lattice dynamics. The presented work focuses on pressures relevant to the interiors of a range of planetary bodies.

3.2 Experimental methods

Sample preparation

Powdered szomolnokite was synthesized through collaboration with Isoflex ($FeSO_4 \cdot H_2O$, using 96% ^{57}Fe) and confirmed using X-ray diffraction (Pardo, Dobrosavljevic, Perez, et al., 2023). A powder pile ~85×100×50 μm^3 was loaded into a panoramic diamond-anvil cell (panDAC) with a Be gasket and a boron-epoxy insert to strengthen the gasket. Two ruby spheres were loaded proximal to the sample and within the boron epoxy insert (~120 radial degrees apart) as in-situ pressure markers. Ruby sphere locations were chosen to eliminate alteration of the sample from the ruby fluorescence excitation laser. Pressure was determined by taking the average of the ruby-determined pressure before and after the experiments (Dewaele et al., 2008). Errors were rounded to reflect the drift in pressure occurring during the experiment, as well as the estimated pressure gradient within the sample chamber due to the fact that the ruby spheres and sample were not co-located (~30 μm apart).

Synchrotron Mössbauer Spectroscopy (SMS)

Using the same batch of synthesized szomolnokite powder, five ambient pressure coherent elastic X-ray scattering measurements were taken at 1 bar with a powdered portion that was either placed on a plexiglass slide or contained within the non-pressurized sample chamber. Measurements were conducted using both the 24-bunch and hybrid timing modes at the Advanced Photon Source beamline 3ID. Four 24-bunch mode measurements were performed at station B. Monochromatic X-rays were tuned to the nuclear resonance energy of ^{57}Fe (14.4125 keV) with an energy spectrum full-width at half maximum of 1 meV using a tunable, high-resolution monochromator (Toellner, 2000). Using an avalanche photo diode (APD) placed downstream in the X-ray beam path and conventional time-filtering electronics, time spectra were collected between delay times of ~25–135 ns after the excitation pulse with collection times ranging between ~1300–1700 seconds (see Ratschbacher et al., 2023 for experimental setup schematic).

The 1 bar hybrid mode measurement was collected at station D with a new spectrometer utilizing a pair of custom high-speed periodic shutters which allows for isolation of an extended delay time window containing the SMS signal without the need for a high-resolution monochromator (Toellner et al., 2011). Hybrid mode measurements access longer timing windows than 24-bunch mode (Finkelstein et al., 2017) and the use of the dual-shutters achieves higher count rates in hybrid mode (Toellner et al., 2011; Ratschbacher et al., 2023). The time window for this data set was 60-600 ns and the collection time was 300 seconds. Isomer shifts were determined in two of the 24-bunch mode measurements by placing a 0.5 mm thick ^{57}Fe enriched stainless steel reference foil in the beam path, resulting in identical values for each measurement (see S1).

High pressure SMS measurements were collected using one APD positioned downstream either just before or immediately following the NRIXS measurements at each compression point. The average collection time was ~900 seconds per spectrum and a timing window of ~25 to 135 ns after excitation was used to fit the data. An attempt was made to measure the high pressure isomer shift using a 2 mm thick ^{57}Fe enriched stainless steel foil placed in the beam path. The perceived heterogeneity in the reference foil within the X-ray scattering volume prevented a robust determination of the isomer shift. Therefore, iron "site 1" for all pressures is fixed at the value determined at ambient conditions in the 24-bunch mode experiments described above, while all other sites' isomer shifts are allowed to vary.

The SMS time spectra were analyzed using the open-source software CONUSS (version 2.2.1, *nrixs.com*) which performs a least squares fitting procedure to best-fit iron's hyperfine parameters, including quadrupole splitting, isomer shift, full width at half maximum of quadrupole splitting distributions, and relative weight fraction of each site, with the use of prior information to constrain fits (Sturhahn 2000). At each compression point, the NRIXS-determined Lamb-Mössbauer factor was fixed (described below). The best-fit values from each pressure were used as starting values for each subsequent pressure.

Nuclear Resonant Inelastic X-ray Scattering (NRIXS)

Incoherent inelastic X-ray scattering was measured with three radially-positioned avalanche photo diodes (APDs) adjacent to the sample chamber and one APD positioned in the X-ray path downstream of the sample to simultaneously measure the monochromator's energy-resolution function (see Jackson, Hamecher, and Sturhahn, 2009 for experimental setup schematic). NRIXS measurements were taken at 1 bar, 4.0(5), 6.5(5), 9.0(6), and 14.5(6) GPa at beamline 3-ID-B at the Advanced Photon Source at Argonne National Laboratory operating in 24-bunch mode with top-up and 153 ns bunch separation, where the number in parentheses reflects the estimated pressure uncertainty in the last reported digit. The X-ray beam was focused using Kirkpatrick-Baez mirrors with a full-width half-maximum of ~16×16 μm^2 (Dobrosavljevic et al., 2022). The average collection time was ~1 hour per scan and ~12 scans were collected at each compression point, with each scan consisting of 1001 steps, 3 seconds/step. Within these ~12 scans, a subset was selected for further data analysis, omitting scans in which significant drift of the incident X-ray intensity occurred during the scan time. The energy scan range for each pressure was: -100 to +150 meV (1 bar), -100 to +150 meV (4.0 GPa), -80 to +220 meV (6.5 GPa), -80 to +220 meV (9.0 GPa), and -80 to +200 meV (14.5 GPa).

All NRIXS data were analyzed with the PHOENIX software package (version 3.0.4, *www.nrixs.com*, Sturhahn 2000) to obtain the partial projected phonon density of states (pPDOS) from the one-phonon contribution of the excitation probability density function. The pPDOS provides access to several quantities related to the ^{57}Fe-participating atoms in the material: the average Lamb-Mössbauer factor, vibrational kinetic energy, mean force constant, vibrational free energy, and vibrational entropy (see Sturhahn 2000, 2004; Sturhahn and Jackson 2007; Murphy, Jackson, and Sturhahn, 2013).

The low-energy portion of the inelastic spectrum is important for determining the Debye velocity, V_D, which is calculated by using a phonon dispersion model to determine the projected sound velocity, $V(E)$, where $V(E) = V_D$ at zero-energy (Sturhahn, 2004). A Debye-like dispersion model varies quadratically with energy. In order to utilize as much data as possible in the low-energy region, an improved empirical model for the dispersion of long-wavelength acoustic phonons is applied to our data (Sturhahn and Jackson 2007; Morrison et al., 2019). Analysis of this low-energy region necessitates measuring the monochromator energy-resolution function in order to remove the elastic peak originating from zero-phonon excitations that masks the inelastic signal. The elastic peak for each compression point was measured with the APD positioned downstream of the sample and removed from the measured NRIXS spectrum using PHOENIX (see supplementary Figs S1 and S2). After elastic peak removal and subsequent extraction of the pPDOS, the data within a selected energy window were evaluated with a fitting procedure to determine V_D using both a polynomial and power law $V(E)$ fit function (Morrison et al., 2019, Sturhahn, 2020 *www.nrixs.com*).

The isothermal bulk modulus K_T and density ρ for szomolnokite's α, β, γ phases were determined in Pardo, Dobrosavljevic, Perez, et al. (2023) using the MINUTI software package (version 2.2.2, Sturhahn 2022). We used MINUTI and tested a range of thermoelastic input parameters to compute the Grüneisen parameter γ and thermal expansion α for each compression point, where the volume dependence of γ is defined as $\gamma = \gamma_0(V/V_0)^q$ (Mie-Grüneisen model). The adiabatic bulk modulus, K_S, is then calculated at each compression point from the relationship $K_S = K_T(1+\alpha\gamma T)$. Shear velocity V_S and compressional velocity V_P may then be determined from our experimental data using the following relations:

$$\frac{3}{V_D^3} = \frac{1}{V_P^3} + \frac{2}{V_S^3}$$

$$\frac{K_S}{\rho} = V_P^2 - \frac{4}{3}V_S^2$$

.

A range of values for γ_0 and q were tested based upon existing reports of γ_0 (and lack of reported q) for sulfates (Knittle, Phillips, and Williams, 2001; Fortes, Wood, Alfredsson, et al., 2006; Fortes, Wood, Vočadlo, et al., 2007; Fortes, Brand, et al., 2013; Brand et al., 2010; Gromnitskaya et al., 2013; Meusburger, Hudson-Edwards,

et al., 2022; Wildner, Zakharov, et al., 2022). Uncertainties in K_S incorporated uncertainty due to pressure and choice of γ_0 and q within the range of γ_0 = 0.67-2.5, q = 1.5-2.5, and Debye temperature T_θ = 300-500 K.

3.3 Results

Synchrotron Mössbauer Spectroscopy (SMS) results

SMS ambient pressure (1 bar)

Table S1 reports the five ambient pressure measurements from this work and from existing literature. All five 1 bar measurements are in good agreement with each other and we find the hyperfine parameters of the two sites needed to fit the data to be consistent with ferrous iron. Figure 3.1 plots all SMS measurements for the high pressure dataset as well as the 1 bar hybrid mode spectrum with both a one- and two-site model in Figure 3.1. The one-site and two-site model are almost identical at earlier delay times (<250 ns), but it becomes evident at later delay times that only the two-site model can best fit the data.

At ambient pressure szomolnokite has one structurally unique iron site (Pistorius, 1960; Wildner and Giester, 1991; Meusburger, Ende, Talla, et al., 2019). Previous work on iron-bearing phases has demonstrated the sensitivity of Mössbauer measurements to differences in local iron environments that X-ray diffraction may not be sensitive to. For example, using X-ray diffraction, bridgmanite and ferropericlase are characterized by a single crystallographic ferrous iron site (Marquardt et al., 2009; Ismailova et al., 2016). In Mössbauer experiments, a second distinct ferrous iron site has been needed to best describe the spectra for these samples, likely arising from differences in next-nearest neighbor environments (e.g., Fei et al., 1994; McCammon, 1997; Jackson, Sturhahn, et al., 2005; Solomatova et al., 2017). Two ferrous sites in natural samples of szomolnokite have also been reported using Mössbauer spectroscopy (see S1).

Isomer shifts (IS) relative to a stainless steel reference foil were determined from 24-bunch mode measurements at 1 bar (24-bunch mode models C and D in Table S1), and are similar to existing data on szomolnokite. The averages and standard deviations for all hyperfine parameters determined from our data are reported in Table S1. All reported parameters for our data and existing literature agree relatively well with each other, but there is some variation in the absolute difference between the reported site 1 and site 2 isomer shifts.

SMS high pressure

Although two ferrous iron sites are needed to fit the data, the weight fraction of site 1 decreases upon increasing pressure (see 3.1, Figure 3.2, and Figure S20 for select high-pressure hyperfine parameters). At 4.0 GPa, site 1 and site 2 are equal in weight fraction within error. Figure 3.1 displays the calculated energy spectrum from the measured time domain data. At 6.5 GPa, two new ferrous sites appear with relatively lower quadrupole splitting (QS) and small weight fractions. The additional sites are most likely the result of the structural transition occurring at 6 GPa, during which distortion of octahedral sites occurs to generate a second, structurally unique iron octahedral site Meusburger, Ende, Talla, et al., 2019. The increase in site 1 and site 2 QS values and the addition of two new sites is consistent with increased octahedral distortion within the unit cell. Meusburger, Ende, Talla, et al., 2019 reports interatomic distances including the Fe-O bond lengths for the octahedral sites at select pressures (see Figure 3.3a). The octahedral distortion metric plotted in Figure 3.3b is defined by Fe-O bond lengths within the octahedra (Brown and Shannon, 1973), but the oxygen bifurcation associated with the α-β structural transition may contribute to asymmetric distortion in the electric field gradient that Mössbauer spectroscopy is sensitive to, leading to more complexity in the iron sites and thus requiring more sites to fit the data than expected from the crystallographic structure alone.

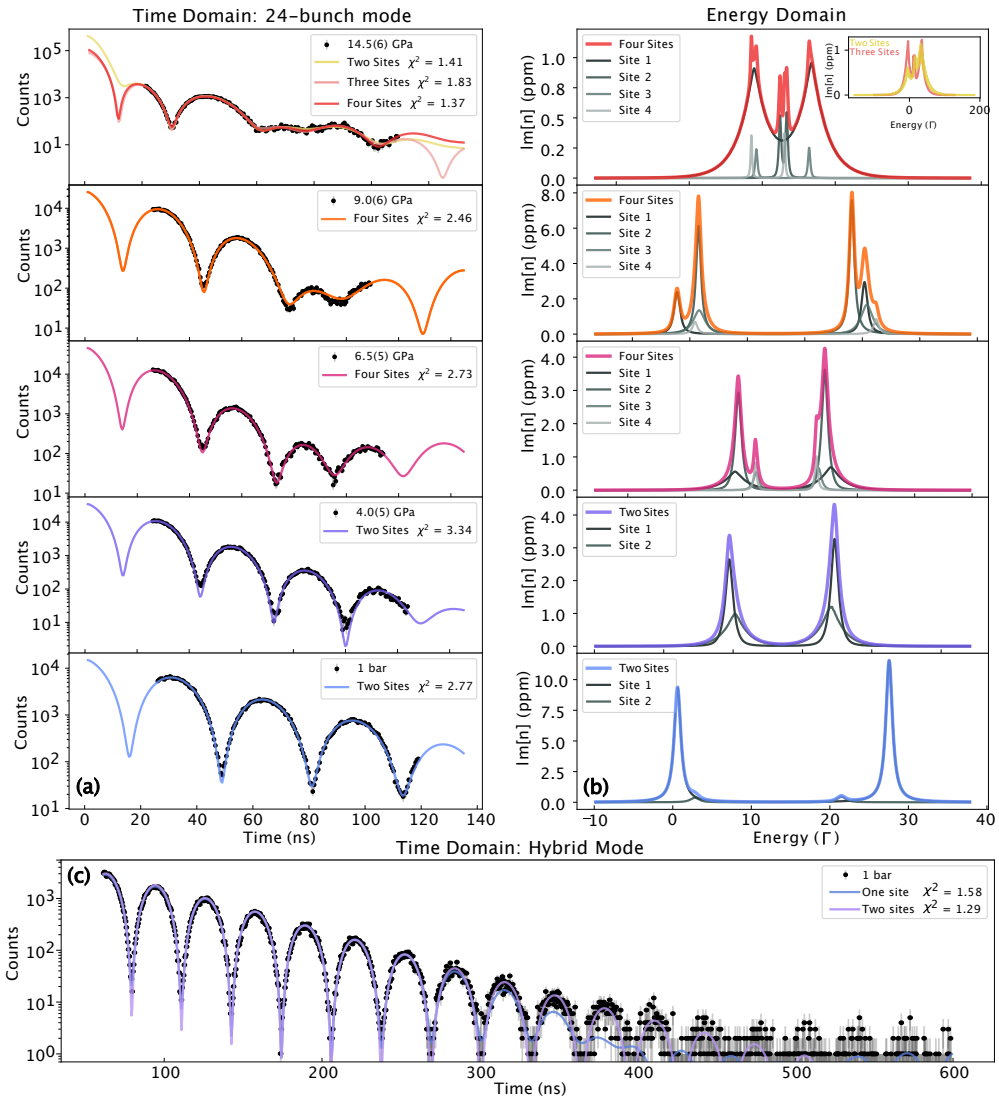

Figure 3.1: SMS data and CONUSS models. **(a)** Time-domain, 24-bunch mode spectra and CONUSS models for the high pressure series including 1 bar spectra "24-bunch mode A", **(b)** energy-domain spectra calculated from the time-domain models for the high pressure series, and **(c)** the ambient pressure hybrid-mode spectrum including the "Hybrid mode A" two-site model.

Table 1. High Pressure Hyperfine Parameters.

Pressure	QS Site 1 (mm/s)	QS Site 2 (mm/s)	QS Site 3 (mm/s)	QS Site 4 (mm/s)	IS Site 1 (mm/s)	IS Site 2 (mm/s)	IS Site 3 (mm/s)	IS Site 4 (mm/s)	FWHM Site 1 (mm/s)	FWHM Site 2 (mm/s)	FWHM Site 3 (mm/s)	FWHM Site 4 (mm/s)	Weight Fraction Site 1	Weight Fraction Site 2	Weight Fraction Site 3	Weight Fraction Site 4
1 bar χ^2 = 2.74	2.614(1)[a]	1.804(28)	-	-	[1.366]	1.179(9)	-	-	0.005(2)	0.034(14)	-	-	0.954(3)	0.046(3)	-	-
4.0(5) GPa χ^2 = 3.34	2.950(5)	2.68(2)	-	-	[1.366]	1.56(1)	-	-	0.121(8)	0.42(2)	-	-	0.528(71)	0.472(66)	-	-
6.5(5) GPa χ^2 = 2.73	3.24(3)	2.927(3)	[2.115]	[2.065]	[1.366]	1.485(6)	[1.516]	[1.629]	0.55(3)	0.122(5)	[0.095]	[0.015]	0.304(14)	0.537(15)	0.085(10)	0.074(6)
9.0(6) GPa χ^2 = 2.46	[3.164][b]	2.588(5)	2.83(3)	[3.057]	[1.366]	1.441(5)	1.572(7)	[1.615]	[0.024]	0.006	0.112(2)	[0.006]	0.220(10)	0.498(15)	0.225(16)	0.056(12)
14.5(6) GPa χ^2 = 1.37	3.810(7)	0.438(4)	3.507(8)	2.203(7)	[1.366]	1.405(9)	1.364(9)	0.379(8)	1.383(4)	0.073(7)	0.064(1)	0.020(1)	0.889(1)	0.058(1)	0.026(1)	0.027(1)

Table 3.1: High Pressure Hyperfine Parameters.

[a]Numbers in parentheses indicate 1σ error throughout the table.

[b]Numbers in brackets indicates fixed value throughout the table. Other than IS Site 1, all values were iteratively fit/fixed during the CONUSS fitting procedure to arrive at the best-fit model.

Further increasing pressure results in site 3 increasing in weight fraction, equivalent to site 2. Site 3 and site 4 QS increases, while site 1 and site 2 QS decrease slightly. This is accompanied by only slight changes in all three sites' IS relative to site 1. At the β-γ structural transition, significant changes occur in all four sites. It is not clear from X-ray powder diffraction how the reconstruction of the unit-cell effects the iron sites. One notable change is the appearance of a very broad site (full-width half-maximum ~1.4 mm/s), which we interpret to be related to the β-γ phase transition. As shown in the calculated energy spectrum in Figure 3.1, the spectral features indicate line-broadening, and the detection of features at earlier delay times, outside of the measured timing window, may be necessary to fit a more accurate model. We therefore show additional two-site and three-site models at 14.5 GPa in Figure 3.1 (time domain) and Figure 3.1 (inset, energy domain) that could explain the measured time spectrum. The three-site model does not accurately capture the shape of the spectrum at times >100 ns compared to the four-site model. The two-site model requires the texture parameter to significantly increase from ~20 to 90 which would imply unlikely reorientation of the grains in the powdered sample. Therefore, while the two- and three-site model are statistically good fits to the data, the four-site model is preferred because it best describes the entire time spectrum without increasing texture and results in the lowest χ^2 of the three models.

Existing high-pressure SMS work on szomolnokite finds similar trends, where two iron sites are required to fit the spectra at ambient pressure and additional sites are needed above the α-β and β-γ transition pressures (Perez et al., 2020). In our work and in Perez et al., 2020, a fourth low-QS site (~0.4 mm/s) is needed to fit the data in the γ-phase field. In both studies, only a small weight fraction of this low-QS site is required to fit the data, and the site with the highest QS in the γ-phase pressure region is also the site with the highest weight fraction. In both studies, a low IS site (relative to site 1 at 1 bar) appears at pressures above the β-γ-phase transition (see Figure 3.2). The low-QS site and low-IS site parameters are not observed in amorphous ferrous or ferric sulfates (Sklute et al., 2015). Differences between this work and Perez et al. (2020) could be caused by differences in sample thickness and non-hydrostatic conditions in our sample chamber at higher pressures. A non-hydrostatic sample chamber could broaden the structural transitions and thus affect the hyperfine parameters associated with each pressure.

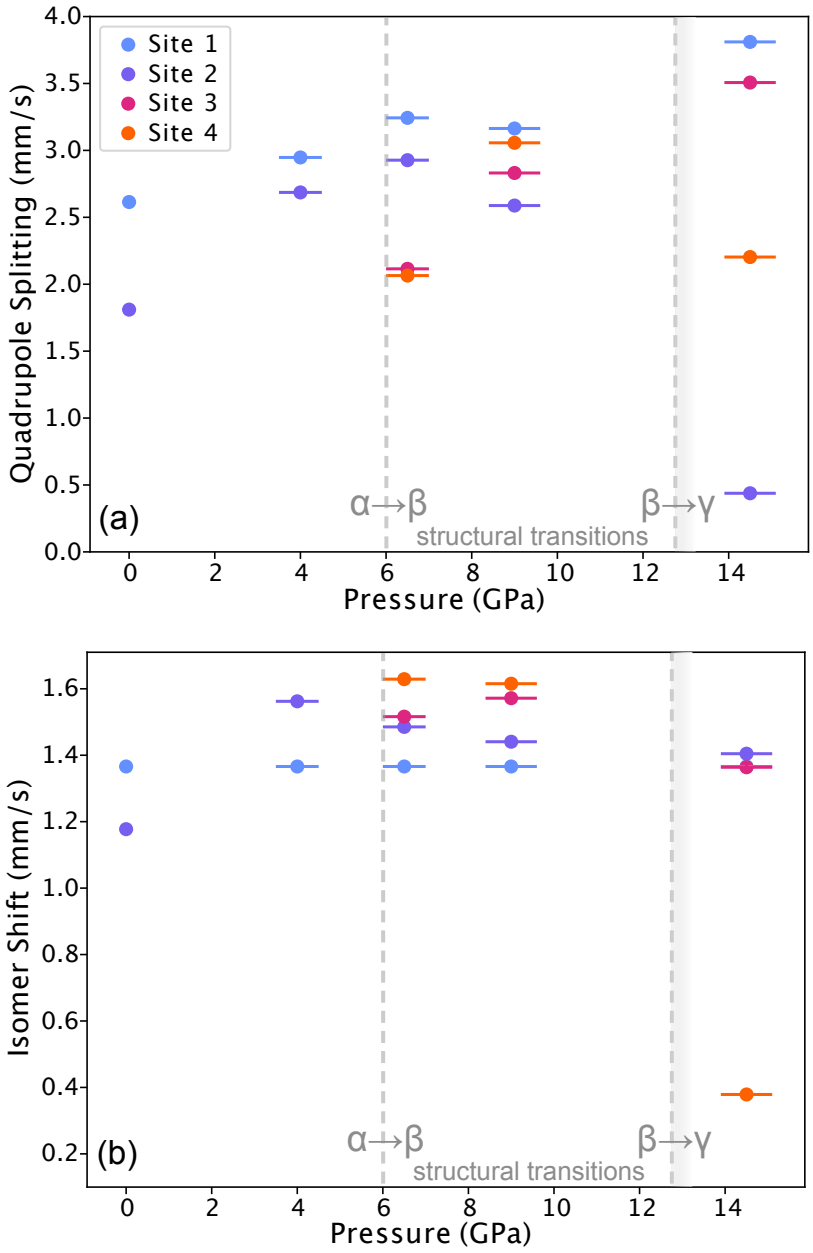

Figure 3.2: Select hyperfine parameters are plotted as a function of pressure, **(a)** quadrupole splitting and **(b)** isomer shift. See supplementary Figure S20 for full-width half-maximums (FWHM) and weight fractions. Two ferrous iron sites describe the data up to 4.0 GPa, at higher pressures two additional sites are needed. Dashed lines indicate the α-β structural transition at 6.15 GPa identified by Meusburger, Ende, Talla, et al., 2019 and the low-pressure boundary of the β-γ structural transition which occurs between 12.7 and 16.8 GPa as measured by Pardo, Dobrosavljevic, Perez, et al., 2023. See Table 1 for reported values.

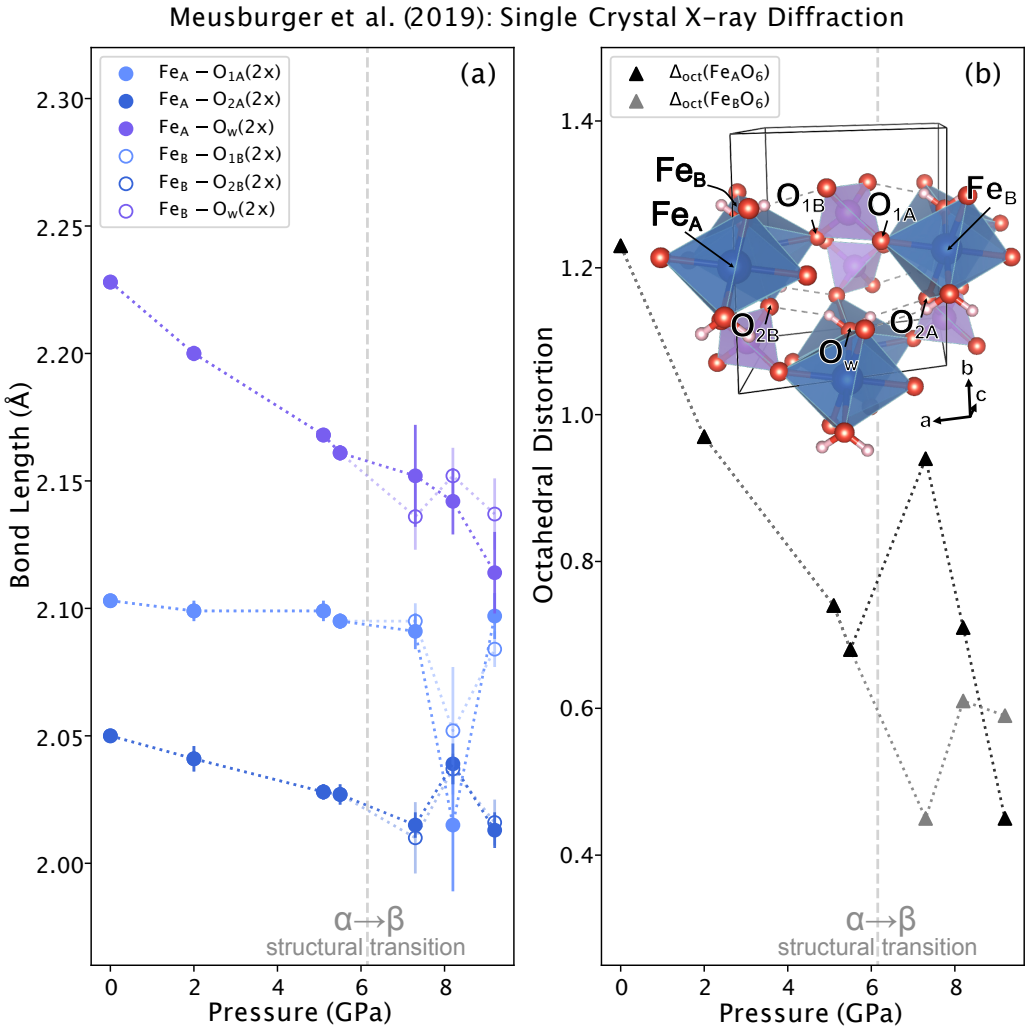

Figure 3.3: Iron-oxygen octahedral bond length and **(b)** octahedral distortion as defined by Brown and Shannon (1973). All data is from Meusburger, Ende, Talla, et al. (2019). Dashed line indicates the α-β structural transition at 6.15 GPa identified by Meusburger, Ende, Talla, et al. (2019), after which a second, structurally distinct octahedral site is created (associated atoms labeled "B"). Szomolnokite's ambient pressure crystal structure is shown in panel **(b)** which consists of chains of octahedra and interconnected tetrahedra. The iron and oxygen labels indicate the atoms associated with the β-phase octahedra.

Nuclear Resonant Inelastic X-ray Scattering (NRIXS) results

NRIXS ambient pressure (1 bar)

Using PHOENIX, the partial phonon density of states (pPDOS) was determined for each compression point (see Figure 3.4a). Parameters calculated from the pPDOS are sensitive to the energy range sampled during data collection. Measuring higher energy-transfers in the NRIXS spectra may detect the presence of high-energy phonons of the sample, while extending the measured energy window also introduces noise if there are in fact no phonons present. For samples like szomolnokite whose pPDOS has never been previously measured, it can be difficult to know a priori the appropriate energy range to sample. In this work we present two methods of determining final parameter values to report at each pressure: 1) a probability distribution of values for each parameter determined from the entire measured energy range, 2) parameter values determined from discrete energy cut-offs in which data at higher energies are ignored. We focus on method (1)'s novel approach to reporting NRIXS derived parameters in the main text. The probability distributions were constructed from random sampling within discretized portions of the pPDOS. The median of each distribution and corresponding interquartile range (the range of the central 50% of the distribution) are reported in Table 2. For more details on method (1)'s sampling approach and comparison with method (2) see supplementary material.

High Pressure NRIXS Parameters

Pressure	Kinetic Energy (meV/atom)[a]	Lamb-Mössbauer Factor[a]	Mean Force Constant (N/m)[a]	Debye Velocity V_D (km/s)	P-wave Velocity V_P (km/s)	S-wave Velocity V_S (km/s)	Adiabatic Bulk Modulus K_S (GPa)[b]	Shear Bulk Modulus G (GPa)[c]	Density ρ (g/cm)[b]
1 bar	14.13 (–0.08, +0.08)	0.5958 (–0.0009, +0.0010)	172 (–9, +11)	2.97(5)	4.89(6)	2.66(4)	44.9(4)	21.9(1.0)	3.09(4)
4.0(5) GPa	14.54 (–0.10, +0.11)	0.6217 (–0.0014, +0.0015)	232 (–15, +19)	3.02(6)	5.61(12)	2.69(6)	72.3(4.5)	24.0(1.6)	3.31(4)
6.5(5) GPa	14.88 (–0.14, +0.19)	0.6503 (–0.0016, +0.0021)	295 (–21, +37)	3.38(8)	5.91(9)	3.01(8)	78.2(3.3)	31.1(2.0)	3.42(4)
9.0(6) GPa	14.75 (–0.12, +0.14)	0.6583 (–0.0012, +0.0011)	269 (–14, +21)	3.46(3)	6.18(9)	3.09(2)	89.6(3.6)	33.6(8)	3.52(4)
14.5(6) GPa	14.92 (–0.19, +0.23)	0.6753 (–0.0016, +0.0016)	297 (–23, +38)	β-phase: 3.44(1) γ-phase: 3.47(1)	β-phase: 6.58(8) γ-phase: 6.58(9)	β-phase: 3.06(2) γ-phase: 3.09(2)	β-phase: 114.1(4.1) γ-phase: 118.0(3.9)	β-phase: 35.7(3) γ-phase: 35.5(3)	β-phase: 3.72(4) γ-phase: 3.82(4)

Table 3.2: High Pressure NRIXS Parameters.

[a]Reported values at each pressure are the median values resulting from Monte-Carlo simulations as described in section 3. Errors are reported in parentheses, calculated from the interquartile range.

[b]Adiabatic bulk modulus and density values derived from equation of state determination using X-ray diffraction measurements (Pardo, Dobrosavljevic, Perez, et al., 2023).

[c]Shear moduli determined using V_S and ρ in PHOENIX.

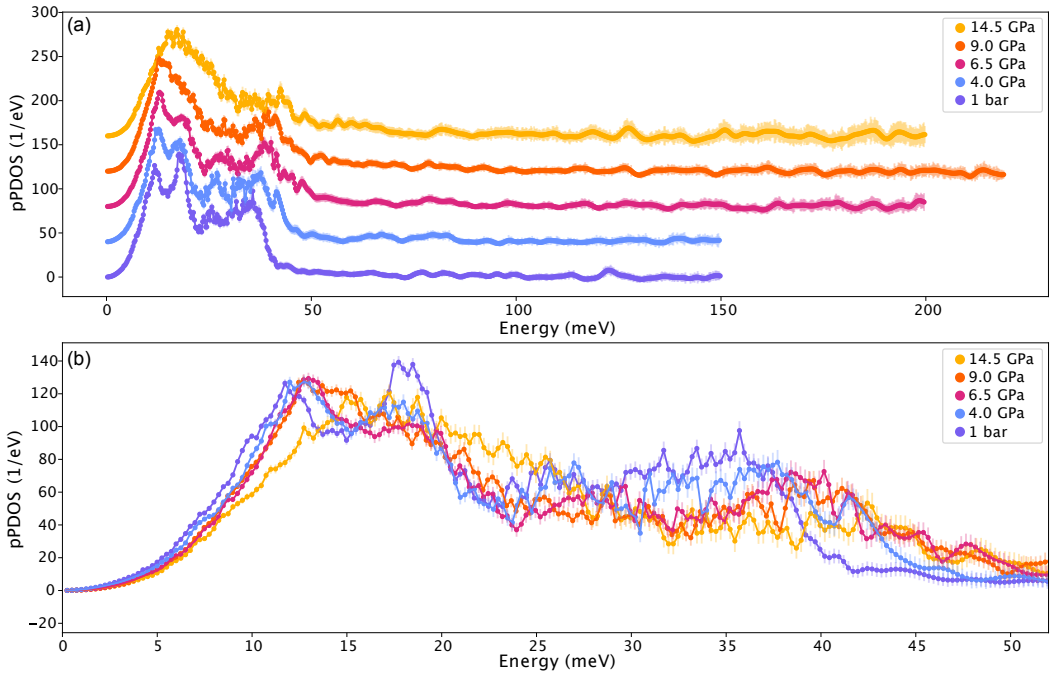

Figure 3.4: The high pressure series of the partial phonon density of states (pPDOS) are plotted in panel **(a)** which are vertically offset for clarity of individual spectra and **(b)** the 0-50 meV range of all pPDOS, not offset for better comparison of the relative changes in vibrational modes

Probability distribution functions are shown in Figure 3.5 as a function of pressure for the Lamb-Mössbauer factor (fraction of scattering events that are recoil-free), kinetic energy (meV per Fe atom), and the mean force constant (average force acting on the ^{57}Fe atoms). Figure 3.6 compares Lamb-Mössbauer factors and mean force constant values at 1 bar for a range of iron-bearing materials, including orthoenstatite, silicate glasses, bcc-Fe, δ-(Al,Fe)OOH oxy-hydroxide, sulfates, and epsomite (Jackson, Hamecher, and Sturhahn, 2009; Dauphas, Roskosz, Alp, Golden, et al., 2012; Gromnitskaya et al., 2013; Solomatova et al., 2017; Morrison et al., 2019; Buchen et al., 2021; Roskosz et al., 2022). Dauphas, Roskosz, Alp, Neuville, et al., 2014 performed NRIXS measurements on both ferrous and ferric silicate glasses (pPDOS-derived parameters later refined by Roskosz et al., 2022), which were also characterized with SMS measurements up to 120 GPa (Solomatova et al., 2017). Dauphas, Roskosz, Alp, Golden, et al., 2012 reports ambient condition NRIXS-derived parameters for potassium- and hydronium-jarosite and goethite, which are compositionally similar to szomolnokite but have higher Lamb-Mössbauer factors and mean force constants due to ferric iron. Interestingly, the Lamb-Mössbauer fac-

tor and mean force constant values of jarosite compositions and szomolnokite are most comparable to ferric and ferrous glasses, respectively, suggesting similar local iron environments. However, clear distinctions of crystalline hydrated sulfates from glasses are revealed in their long-wavelength properties, that is their bulk elastic properties (i.e., K_S, and G) (see section 4).

NRIXS high pressure

At ambient pressure, the two highest intensity peaks in the measured NRIXS spectrum are centered at 12 meV and 18 meV, with the 18 meV peak's intensity greater than the 12 meV peak (see Figure 3.4a). Upon increasing pressure, higher energy modes between 40–50 meV are visibly populated, with modes >45 meV appearing at 6.5 GPa, likely associated with the transition to the lower symmetry triclinic β-phase. The 12 meV peak also shifts towards higher energies from 1 bar to 6.5 GPa, reflecting typical behavior of rising vibrational frequencies with compression, but stagnates between 6.5-9.0 GPa, coincident with the β-transition (see Figure 3.4b). Simultaneously, the maxima of the 18 meV peak decreases in intensity and shows no movement towards higher energies. By 9.0 GPa, vibrational frequencies of the original 12 meV and 18 meV peak positions are populated such that the 18 meV peak maximum is not discernible. The most significant change occurs between 9.0 and 14.5 GPa, where vibrational frequencies <15 meV and between 33–43 meV become less populated, while intermediate frequencies between 15-28 meV become more populated. At 14.5 GPa, the sample may or may not be transformed to the γ-phase since X-ray diffraction data bracket the transition within a few GPa pressure interval (12.7–16.8 GPa, Pardo, Dobrosavljevic, Perez, et al., 2023). The stagnation of the 12 meV peak at the β-transition and subsequent redistribution of phonon intensities at higher pressures suggest a change in compression mechanism that inhibits the vibrational frequency distribution from continuously moving towards higher energies with increasing pressure. In the next paragraph, we quantify these observations.

The resulting interquartile ranges (IQRs) and medians of the probability density function analysis shown in Figure 3.5 suggest that the Lamb-Mössbauer factor, kinetic energy per atom, and mean force constant exhibit an approximately linear pressure-dependent trend to ~6 GPa, at which a change of slope occurs for data higher than 6 GPa. As confirmed by previous X-ray diffraction measurements Meusburger, Ende, Talla, et al., 2019 (; Pardo, Dobrosavljevic, Perez, et al., 2023), szomolnokite undergoes its α-β structural transition (monoclinic $C2/c$ to triclinic $P\bar{1}$) at 6

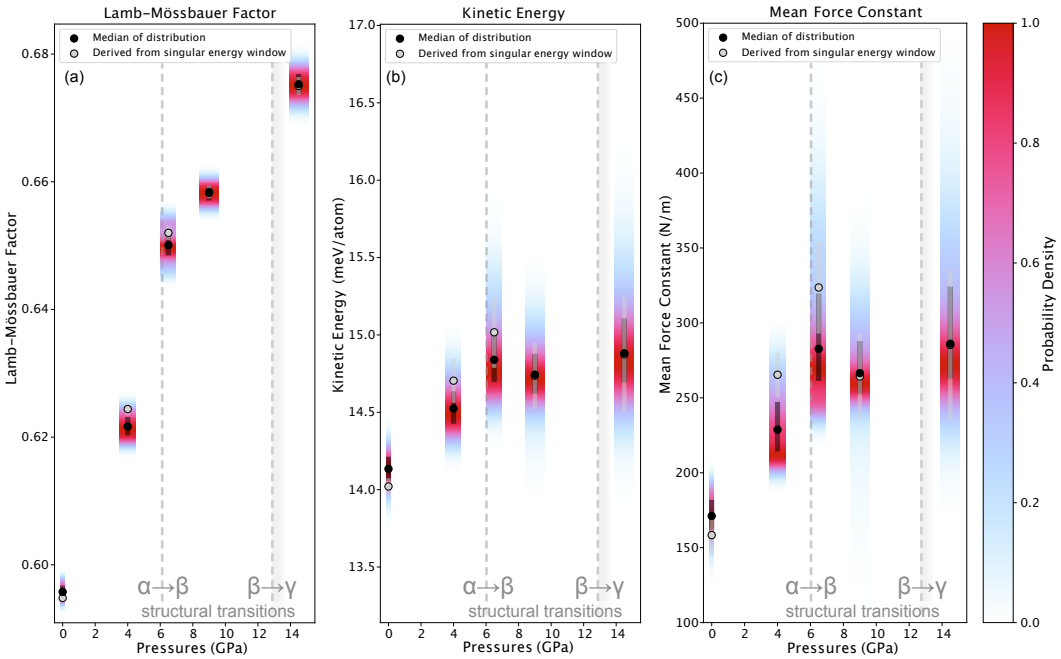

Figure 3.5: Parameters determined from PHOENIX. Panel **(a)** Lamb-Mössbauer factor, **(b)** kinetic energy, and **(c)** mean force constant probability distributions as a function of pressure. The median of each distribution and interquartile range are represented by black circles and black vertical error bar. The value of each parameter derived from a singular energy window is plotted for comparison (light grey circles with error reported by PHOENIX). Dashed lines indicate the α-β structural transition at 6.15 GPa identified by Meusburger, Ende, Talla, et al., 2019 and the low-pressure boundary of the β-γ structural transition which occurs between 12.7 and 16.8 GPa as measured by Pardo, Dobrosavljevic, Perez, et al., 2023. Errors in pressure are determined by in-situ ruby fluorescence and are represented by the width of the probability distribution at each pressure.

GPa. The IQRs for all parameters' probability distributions show increasing trends in the 1 bar–6.5 GPa pressure interval, suggesting an increase in parameter values up to the α-β structural transition. At pressures higher than the β-transition, the IQRs for the kinetic energy and mean force constant are mostly invariant to pressure, suggesting a plateau-like trend. Within the uncertainties considered here, a decrease in kinetic energy and mean force constant between 6.5 and 9.0 GPa could be occurring, which may be related to a crystal lattice softening in the vicinity of the β-phase transition. The simultaneous stagnation of the low-energy vibrational modes in the pPDOS and resulting plateau-like trend of the Debye velocity, determined from the low-energy modes, corroborates lattice softening at a range of length-scales within the crystal lattice. See section 3.2.3 for sound velocity discussion.

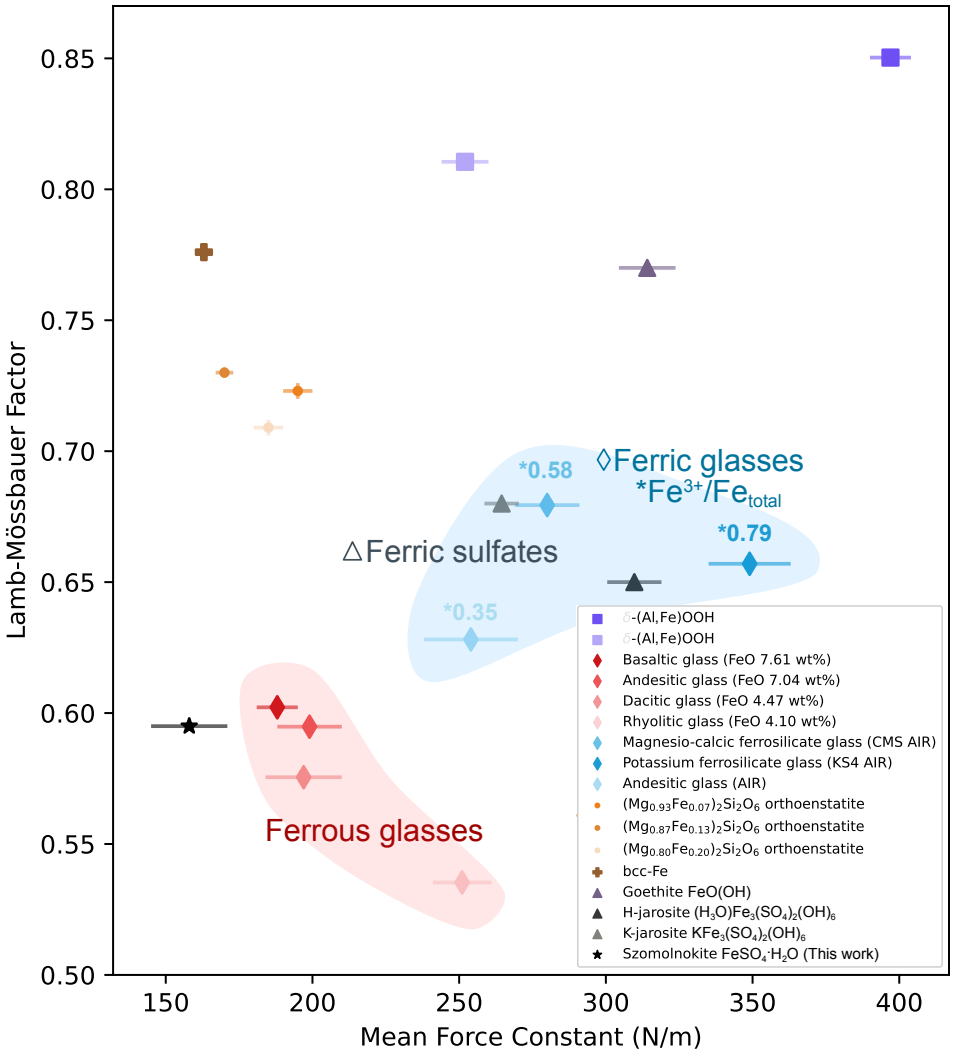

Figure 3.6: Lamb-Mössbauer and mean force constant values for a range of iron-bearing materials. Szomolnokite is plotted as the black star. Purple squares represent the highest and lowest values from two orientations of single crystal δ-(Al,Fe)OOH (Buchen et al., 2021), red diamonds represent ferrous silicate glasses while blue diamonds represent ferric glasses (Roskosz et al., 2022), orange circles represent three orthoenstatite compositions (Jackson, Hamecher, and Sturhahn, 2009), bcc-Fe is plotted as the brown cross (Morrison et al., 2019), and FeOOH and two ferric sulfates are plotted in solid triangles (Dauphas, Roskosz, Alp, Golden, et al., 2012). Red and blue shaded regions are for qualitative visual grouping of the ferrous and ferric compositions, respectively.

Although the highest-pressure compression point at 14.5 GPa may lie within szomolnokite's γ-phase stability field, the IQRs and medians for the kinetic energy and mean force constant are very similar to those at 6.5 GPa. The Lamb-Mössbauer factor continues to increase without overlapping IQRs, with a change in slope near the β-transition. The mean force constant increasing with pressure up to 6.5 GPa is consistent with strengthening of Fe-O bonds in octahedral coordination. In general, all three parameters discussed above indicate a change in compression mechanism at pressure higher than the α-β transition, consistent with the visual behavior of the pPDOS. The trends observed here indicate that although the α-β structural transition is marked by only a slight distortion in the Fe-octahedral site, there is a marked change in the atomic dynamics of szomolnokite.

The possibility that kinetic energy and mean force constant plateau or decrease in the β-phase field could be attributed to changes in the hydrogen-bonding system at the α-β transition as outlined in Meusburger, Ende, Talla, et al., 2019, where distortion of octahedral sites create a second, structurally distinct iron site. Asymmetrical changes in the bonds of the O_{water} and oxygen atoms at the corner-sharing tetrahedra-octahedra sites occur with this distortion, resulting in lengthening of certain O_{water}-O bonds, while decreasing others. Fe-O bond lengths measured in Meusburger, Ende, Talla, et al., 2019 plotted in Figure 3.3a show that there are complex changes in the bond-lengths associated with the iron atoms between 7 and 8 GPa, in that some lengths continue to decrease (Fe_A-O_{2A}), while others discontinuously decrease (Fe_A-O_{1A} and Fe_B-O_{1B}) or sharply increase ($Fe_{A,B}$-O_{water}). The net effect could lead to the plateau-like trend in the mean force constant, discussed above.

We have seen from the discussion above that the transformation of the iron-, oxygen-, and water-bonding system are reflected in the iron-participating lattice vibrations. Interestingly, the isothermal bulk modulus (K_T) exhibits a similar trend to the kinetic energy and mean force constant at the β-phase transition (see 4.5b). At the β-transition, K_T decreases from ~85 GPa to 76 GPa, indicating a decrease in lattice incompressibility. At the pressures studied within the β-phase stability (6.5 and 9.0 GPa), K_T increases from 77.8(2.9) GPa to 89.3(3.5) GPa. Near the γ-phase boundary sampled in this study (14.5 GPa), K_T increases significantly to K_T = 117.7(3.8) GPa (Pardo, Dobrosavljevic, Perez, et al., 2023). The observed plateau-like trend in the ^{57}Fe mean force constants and increase in K_T at 14.5 GPa implies that upon compression, structural changes continue to increase the volumetric incompressibility, while only certain atomic bonding environments exhibit stiffening.

Sound velocities

The Debye velocity V_D, compressional wave velocity V_P, and shear wave velocity V_S were determined using PHOENIX as described in section 2.3. Using a fitting procedure that accounts for many possible fit ranges for a selected energy window, PHOENIX incorporates the statistical error of the measured data points within the fit ranges and reports a probability distribution function (PDF) of the calculated V_D. The most probable Debye velocity is found by fitting the PDF, where the reported value corresponds to the peak of this fit and its uncertainty is the distribution's full-width at half maximum (Morrison et al., 2019). Szomolnokite's acoustic phonon dispersion may only be Debye-like at energies $\lesssim$5 meV, the region in the data that coincides with the tails of the resolution function, and hence the elastic peak removal process. For this reason, two different energy windows were used to carry out the fitting procedure and determine two endmember Debye velocity models: (1.5-6 meV) and (0.5-8 meV). Our reported V_D at each pressure is the average of the combined velocity distributions generated from the reported V_D in these two models and corresponding standard deviations (see supplement for individual fitting results at each pressure). These results are shown in Figure 3.7. Trends in V_D and V_S suggest a moderate increase within the α-phase, then a sharp increase across the β-transition followed by plateau. If the data were densely sampled across the β-phase transition, we may expect V_P to exhibit a decrease in the vicinity of the transition, because V_P is mostly sensitive to the equation of state (equations 1 and 2).

To place these results in context with other similar phases, sound velocities and shear moduli are plotted in Figure 3.8 up to 20 GPa for anhydrous and hydrous silicate glasses, hydrous Phase A, pure water ice, H_2O ice with 0.9 mol% NaCl, and epsomite, measured by Brillouin scattering and ultrasonic interferometry (Sanchez-Valle, Sinogeikin, et al., 2008; Sanchez-Valle and Bass, 2010; Gromnitskaya et al., 2013; Sakamaki et al., 2014; Zhang, Hao, et al., 2019; Shi et al., 2021; Gu et al., 2021; Wei et al., 2022). Notably, szomolnokite's high pressure shear moduli are most similar to the high-pressure ice phases despite being significantly denser. The plateau observed in szomolnokite's high pressure V_S (and G) values compared to V_P at pressures >5 GPa suggest that the shear properties are more greatly affected by the changes in compression mechanisms discussed in section 3.1.

Although sharing similar iron-site specific parameters described in section 3.2.1, szomolnokite has much slower V_P and V_S values at ambient conditions than the hydrous (~0.68 wt% FeO) and anhydrous rhyolitic glass (~0.23 wt% FeO) compo-

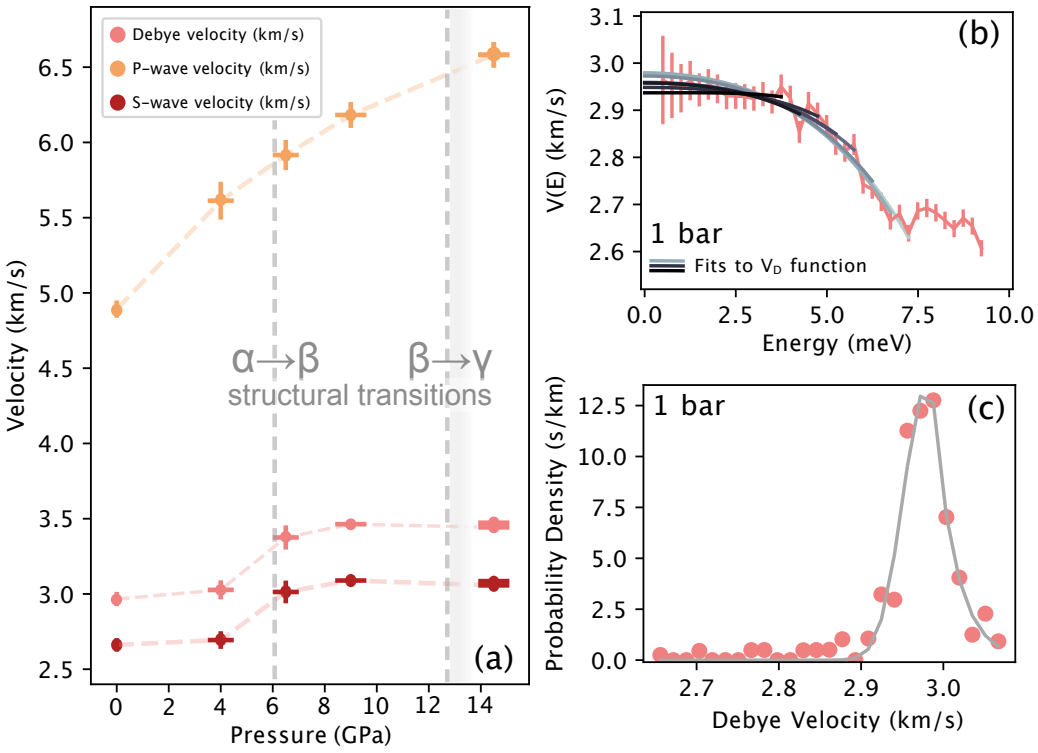

Figure 3.7: Sound velocities and example fitting procedure. Panel **(a)** plots the Debye velocity V_D, P-wave velocity V_P, and S-wave velocity V_S plotted as a function of pressure. Dashed lines indicate the α-β structural transition at 6.15 GPa identified by Meusburger, Ende, Talla, et al., 2019 and the low-pressure boundary of the β-γ structural transition which occurs between 12.7 and 16.8 GPa as measured by Pardo, Dobrosavljevic, Perez, et al. (2023). Panel **(b)** shows an example V_D fitting procedure at 1 bar in which the low energy portion of the pPDOS is fit to polynomial or power law $V(E)$ function. Panel **(c)** plots the resulting 1 bar velocity distribution function generated from the series of fits plotted in panel **(b).** Velocity errors in panel **(a)** are generated by combining two velocity distribution functions resulting from fitting two different energy windows as described in the main text.

sitions. Taking density into consideration (see supplement Figure S20), szomolnokite's shear moduli values are similar to the hydrous rhyolitic glass at 1 bar. By ~3 GPa, szomolnokite's V_P is comparable to the rhyolitic glasses. At higher pressures >5 GPa, szomolnokite's adiabatic bulk modulus is comparable to that of enstatite, Al-bearing enstatite, and diopside glasses, but remains comparatively lower in V_P and V_S. At all pressures Phase A has higher velocities and shear moduli than szomolnokite.

3.4 Discussion

With increasing compression, trends in the kinetic energy and mean force constant imply short-range lattice softening associated with iron atoms in szomolnokite near the α-β transition and possibly into the γ-phase. The appearance of two additional low-quadrupole splitting octahedral sites at pressures greater than the α-β transition suggest minor asymmetries in the electric field gradients of a subset of the iron octahedral sites, consistent with iron-site distortion. The Debye velocity, determined from low-energy acoustic vibrational modes, simultaneously plateaus at the β-transition. Additionally, the bulk modulus K_T decreases at the α-β transition. This behavior suggests that the distortion of iron octahedra, which defines the α-β transformation from the monoclinic structure to the triclinic structure, contributes to the long-range crystal lattice softening evident in the observed elastic properties.

The high-pressure lattice softening and increasing asymmetry in iron's electric field gradient is accompanied by a change in the pressure dependence of sound velocities, most notably V_S and the shear modulus. As the iron-endmember, szomolnokite has exhibited the highest α-β transition pressure compared to other sulfates, and thus incorporation of iron would likely result in V_S discontinuities at greater depths. Currently, tidal amplitude measurements of our solar system's icy satellites are the most-likely source of information on their interior structures (Wahr et al., 2006; Nimmo and Manga, 2009; Hemingway and Mittal, 2019), rather than seismology. Research has focused on modeling the relationship between observed Love numbers and interior properties such as the radius of the mantle/icy shell, density (i.e., average density, density of shell, mantle, ocean, and core), and the shear moduli, *G,* of the interior structures (Wahr et al., 2006). Understanding localized structure, such as identifying structural heterogeneities associated with the Tiger Stripes on the south pole of Enceladus, also relies on knowing the expected range of shear and bulk moduli of the icy satellites (Berne et al., 2022). Challenges exist in deter-

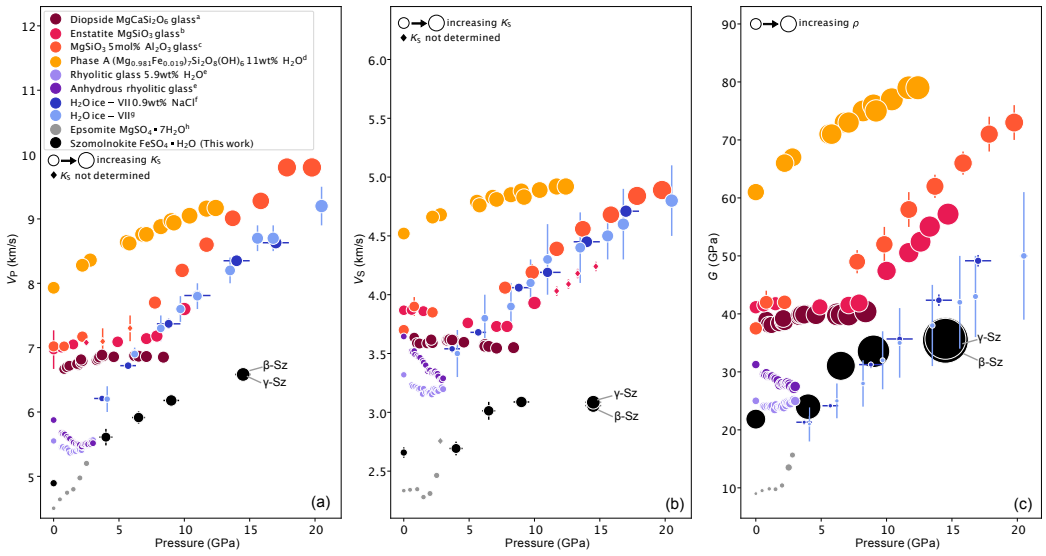

Figure 3.8: P-wave velocity V_P and **(b)** S-wave velocity V_S and **(c)** shear moduli G are plotted for a range of silicate glasses, oxyhydroxide Phase A, high pressure ices, and two sulfates (including this work). Symbol size indicate relative adiabatic bulk modulusK_S values in panels (a) and (b) and density ρ values in panel (c). References are as follows: [a]Sakamaki et al., 2014, [b] Sanchez-Valle and Bass, 2010, [c] Wei et al., 2022, [d]Sanchez-Valle, Sinogeikin, et al., 2008, [e]Gu et al., 2021, [f]Shi et al., 2021, [g]Zhang, Hao, et al., 2019, and [h]Gromnitskaya et al., 2013. Velocity and pressures errors are plotted when reported, most are smaller than the symbol size. For szomolnokite's highest pressure point, two values are reported using elastic parameters for the β-$FeSO_4{\cdot}H_2O$ and γ-$FeSO_4{\cdot}H_2O$ phases. See Figure S20 for adiabatic moduli and density as a function of pressure.

mining the thickness of an icy shell and origins of structural heterogeneities from orbiter measurements, due in part to uncertainties in the shear modulus of the ice-rich crust, and therefore determining the shear moduli of candidate non-ice phases (i.e., hydrous sulfates) plays an important role in interpreting orbiter observations.

Typical properties assigned to icy crusts are $G \cong 3.3$ GPa and $\rho \cong 0.9$ g/cm³ (Gammon et al., 1983; Wahr et al., 2006; Souček et al., 2019; Berne et al., 2022). For pressures <5 GPa, most relevant to the icy satellites in our solar system, szomolnokite's presence would increase both the density and shear modulus (ρ_{sz} = 3.09 g/cm³ and G_{sz} = 21.9 GPa at 1 bar). Addition of epsomite (G_{ep} = 9.0 GPa) would also lead to an increased shear modulus. Thus, an ice-sulfate mixture would have a significantly higher shear modulus than the pure-ice value commonly used (G = 3.3 GPa). At higher pressures relevant to icy, sulfate-rich worlds whose icy crusts/mantles reach pressures >5 GPa, szomolnokite would significantly increase the bulk density, but

not influence the shear modulus as greatly compared to lower pressures. The similar shear moduli but drastically different density between szomolnokite and the high-pressure ice phases compared in this work may influence the inferred structure and dynamics of icy, sulfate-bearing shells, mantles, or cores. Presence of sulfates at depth would affect assumed densities of icy crusts that factor into Love number models, likely increasing observed h Love numbers, for example, independent of icy shell thickness (Moore and Schubert, 2000).

3.5 Conclusions

Measurements of the lattice dynamics, iron-site specific behavior, and crystal structure are highly complementary. Nuclear resonant scattering measurements, in combination with X-ray diffraction results, reveal changes in both iron site-specific and bulk lattice properties in szomolnokite at high pressure, including lattice softening accompanying the α-β transition. The α-β monoclinic-triclinic structural transition observed in szomolnokite has been measured in several other hydrous sulfates, and detected at different pressures. It is unclear how the lattice dynamics and transition pressure would change in mixed-cation sulfate compositions, but current work has demonstrated that the Fe-endmember szomolnokite undergoes the α-β transition at higher pressures than the Mg-endmember, kieserite. Therefore, the α-β transition in an iron-bearing composition that is close to the kieserite end-member may occur at pressures slightly higher than that for kieserite, and include softening of lattice vibrational modes. Structural changes in hydrated sulfates at higher pressures analogous to szomolnokite's γ-phase have yet to be investigated. Nevertheless, such studies are important to better understand this multi-component system, and moving forward, at temperatures relevant to planetary bodies.

Coexistence of hydrous sulfates with varying hydration states, variable temperature, and other dynamic planetary processes are all key factors that need to be considered in applying endmember experimental data to natural environments. We have discussed the presence of sulfates at depth and their effect on assumed densities of icy crusts, which would factor into Love number models of icy satellites. Whether as minor or major components of localized planetary environments or bulk icy satellite interiors, further work is required to better understand the behavior of multi-component systems comprised of hydrous sulfates and other materials.

Chapter 4

HIGH PRESSURE, CRYOGENIC INFRARED SPECTROSCOPY AND THEORETICAL MODELING OF SZOMOLNOKITE

4.1 Introduction

Hydrous sulfates and other sulfate salts have been observed on Earth, Mars, the icy satellites, and even asteroids. Both hydrous and non-hydrous sulfate minerals naturally form through many processes on Earth's surface, including formation as weathering products of pyrite, pyrrhotite, or SO_2-basalt interactions, and have been studied in relation to biological S-cycles, evaporate deposits, hydrothermal systems, mine waste, and as components of igneous rocks from a variety of volcanic systems (Chou, Seal, and Wang, 2013; Dyar et al., 2013; Hao et al., 2014; Machado de Oliveira et al., 2019; McCanta, Dyar, and Treiman, 2014; Rye, 2005). Because of the many hydrous sulfates found in close proximity to each other in natural environments and laboratory experiments on Earth, interpretation of remote observations of Mars and the icy satellites has focused on selecting mixtures of sulfates, sulfides, and hydrous phases that reproduce observed infrared, near-infrared, and visible wavelength spectral features (Bishop, Parente, and Weitz, 2009; Bu et al., 2018; Dalton, Shirley, and Kamp, 2012; Lane, Dyar, and Bishop, 2004; Lichtenberg et al., 2010). These observations have shown that sulfates can host a variety of cations, such as Fe, Mg, Na, Ca, Cu, Mn, and Al, and varying amounts of molecular water and hydroxyl groups. Sulfate cations can be of mixed valence states, and sulfate minerals with different cation valence states can coexist depending on the degree of weathering and environmental conditions. These sulfates may be may be further altered on short timescales (hours to days), generating complex chemical mixtures (McCollom et al., 2013; Wang, Jolliff, et al., 2016).

Spectroscopy measurements taken by the Galileo spacecraft identified hydrous sulfur-bearing material on the surface of Europa, specifically on the trailing hemisphere

which is significantly darker and spectrally distinct from the ice-rich leading hemisphere (Carlson et al., 2009; McEwen, 1986). Spectral laboratory measurements and computational modeling have identified sulfate-ice mixtures as best matches to the observational data (Cerubini et al., 2022; Dalton, Shirley, and Kamp, 2012; King, Fletcher, and Ligier, 2022), however the origin of the sulfur-rich phases on the surface is not fully understood. Recent work has suggested a primarily exogenic sulfur source for the surfaces of Io, Europa, and Ganymede (e.g., Trumbo, Brown, and Hand, 2020). Current work suggests endogenic surface material alteration by exogenic sulfur radiolysis (Carlson et al., 2009; Trumbo, Brown, and Hand, 2020), but cannot rule out at least some quantities of endogenic S, such as localized concentrations of SO_2 (see for example, Becker et al., 2022).

Due to the observed abundance of sulfate on the surface, it has been proposed that hydrated sulfates are primary components of the icy satellite's interior oceans and/or icy mantles and this has motivated work on hydrous sulfates at high pressures (Comodi et al., 2014; Fortes, Brand, et al., 2013; Fortes, Fernandez-Alonso, et al., 2017; Fortes, Wood, Alfredsson, et al., 2006; Nakamura and Ohtani, 2011; Pan, Yong, and Secco, 2020). Candidate sulfates primarily consists of Na- and Mg-bearing sulfates with various hydration states. Much work has a focused on magnesium end member hydrated sulfates, which have been modeled in the interior of Ganymede as a layer of sediments at the top of a silicate mantle (Meusburger, Ende, Matzinger, et al., 2020; Nakamura and Ohtani, 2011). The interior structures of the icy satellites are subjects of ongoing work (e.g., Gomez Casajus et al., 2021), but gravity field and magnetometer data from spacecraft like Galileo have led to the current understanding of interior ice, mantle, and core layers. Europa, the smallest of the Galilean moons, is differentiated and likely composed of an iron-rich core, silicate mantle, ocean, and ice-rich crust (Anderson et al., 1998; Carr et al., 1998; Hussmann, Sotin, and Lunine, 2015). The largest Galilean moon, Ganymede, may have a more complex differentiated interior composed of an iron-rich core, silicate mantle, and a basal ice-rich layer underlying the ocean and ice-rich crust (Hussmann, Sotin, and Lunine, 2015). Depending on the dynamics within and between these layers, it has been proposed that rocky materials and precipitating salts (e.g., sulfates) in the ice-rich crust and ocean should sink towards and through the basal ice layer, potentially cycling sulfur-bearing phases from the surface of the icy crust to the basal ice-rock interface at the top of the silicate mantle (Ligier et al., 2019; Molyneux et al., 2020; Vance et al., 2014). Internal heating could melt the ice at this interface and cause fluid-rock interactions (Ahrens et al., 2022).

Geologic interpretations of surface imaging and dynamical modeling support surface-subsurface exchange within Ganymede and the other icy satellites (Buffo et al., 2020; Howell and Pappalardo, 2018; Prockter et al., 2017), Thus, the observed abundance of hydrated sulfates on their surfaces may be indicative of their presence at depth and validates ongoing high pressure work (Zolotov, 2019). While Na- and Mg-rich sulfates are abundant on the surfaces of the icy satellites and have been the focus of existing high-pressure experimental work, it is frequently observed on Earth and Mars that other 2+ cations can readily substitute in $M^{2+}SO_4 \cdot nH_2O$ (M = Fe, Mg, Cu, Ni, Co, Zn) crystal structures. Iron-bearing compositions may be present in higher concentrations at greater depths, especially when considering additional sources of sulfates such as leaching of chondritic sulfates from an iron-rich core into an overlying mixed ice-rock mantle (Kargel, 1991). Thoroughly characterizing the physical and chemical properties of the endmember components that may comprise these natural environments is thus necessary to better understand their properties at low temperatures and high pressures.

Background

Raman and IR spectra for both synthetic and natural hydrous sulfates have been reported extensively in the literature, demonstrating approaches for identifying individual hydrated sulfates as well as reporting variability in observed vibrational mode intensity and widths for individual minerals across multiple studies (e.g., 37 natural sulfates (Lane, 2007), 14 natural sulfates (Majzlan et al., 2011), synthetic $(Fe_{1-x},Mg_x)SO_4 \cdot H_2O$ (Talla and Wildner, 2019), synthetic $MgSO_4 \cdot 6H_2O$, $Na_2SO_4 \cdot 10H_2O$, $Na_2Mg(SO_4)_2 \cdot 4H_2O$ (Dalton, Shirley, and Kamp, 2012)). Cloutis et al., 2006 performed extensive spectral, compositional, and structural characterization on dozens of OH-bearing and H_2O-bearing sulfates in order to validate and improve band assignments to develop spectral discrimination diagnostics for sulfate compositions.

Szomolnokite in particular has been spectrally characterized at ambient conditions (Cloutis et al., 2006; Lane, Dyar, and Bishop, 2004; Majzlan et al., 2011; Talla and Wildner, 2019), temperatures as low as 7 K (Chio, Sharma, and Muenow, 2007), and high pressures up to 9 GPa (Meusburger, Ende, Talla, et al., 2019). These measurements have included a low temperature Mössbauer study which identified a magnetic order-disorder transition at 29.5 K (Alboom et al., 2009). Most recently, high pressure X-ray diffraction measurements have identified two structural phase transitions occurring at 6 GPa (monoclinic $C2/c$ to triclinic $P\bar{1}$ β-$FeSO_4.H_2O$) and be-

tween 12.7-16.8 GPa (triclinic $P\bar{1}$ to monoclinic $P2_1$ γ-$FeSO_4.H_2O$) (Meusburger, Ende, Talla, et al., 2019; Pardo, Dobrosavljevic, Perez, et al., 2023). Using single crystal X-ray diffraction up to 9 GPa, Meusburger, Ende, Talla, et al. (2019) reported a detailed description of the structural transformation mechanism accompanying szomolnokite's low pressure transition to β-$FeSO_4{\cdot}H_2O$. At ambient conditions, the kieserite-structure type α-$FeSO_4{\cdot}H_2O$ is formed by continuous chains of corner sharing Fe-octahedral units $[FeO_4(H_2O)_2]^{6-}$ parallel to the c-axis, containing only one crystallographic iron site. Octahedral oxygen atoms are shared with SO_4 tetrahedra, creating a 3D network. At the α-β transition pressure, the tilting of the SO_4 tetrahedra and adjacent FeO_6 octahedra create a second structurally unique octahedral site. This lattice distortion is accompanied by a bifurcation of the hydrogen-bonding system, doubling the number of unique hydrogen bridges from two to four. An analogous monoclinic $C2/c$ to triclinic $P\bar{1}$ transition has been observed in other $M^{2+}SO_4{\cdot}H_2O$ (M = Fe, Mg, Ni, Co) kieserite-type compositions (Ende et al., 2020; Meusburger, Ende, Matzinger, et al., 2020; Wildner, Ende, et al., 2021). See Chapters 2 and 3 for more details.

The powder X-ray diffraction experimental data for $FeSO_4{\cdot}H_2O$'s β-γ transition reported by Pardo, Dobrosavljevic, Perez, et al. (2023) did not show any evidence of exsolved high pressure ice phases, and, corroborated by preliminary analysis of high pressure synchrotron infrared spectroscopy data, indicated that H_2O was stable in the crystal structure up to 80 GPa. In this study, we present a full analysis of high-pressure and low-temperature synchrotron infrared spectroscopy measurements up to 23 GPa aimed at 1) identifying changes in vibrational modes due to the two structural transitions occurring within this pressure range and based on these identified spectral features, and 2) determining the temperature dependence of the α-β and β-γ structural transitions. We support our experimental data analysis with preliminary molecular dynamic simulations resulting in a predicted vibrational density of states to aid in interpretation of our data and compare against existing literature.

4.2 Materials and methods

Experimental methods

High pressure and low temperature synchrotron infrared compression and decompression measurements were conducted at beamline 22-IR-1 at the National Synchrotron Light Source II at Brookhaven National Laboratory. Synchrotron Fourier transform infrared (FTIR) spectroscopy measurements were taken using a Bruker

Vertex 80v FTIR spectrometer and a custom IR microscope system with a wide-band MCT detector from 400-5000 cm^{-1}. Temperatures down to 20 K were achieved using an open-flow helium cryostat. Temperature errors are <1 K below 100 K and 2 K above 100 K. The pressure-temperature space sampled in this work is plotted in Figure 4.1, consisting of one ambient temperature, high pressure compression-decompression series, one low-temperature series at 1 bar, and six individual low-temperature, high-pressure series. A set of high-temperature cycling measurements was performed at 300 and 320 K to determine heat sensitivity of the sample, and after measuring five positions throughout the sample pre-, during, and post-heating found no alteration reflected in the measured spectra.

Powdered szomolnokite was loaded into a diamond anvil cell with either a KBr or NaCl pressure medium; one compression series was loaded with a He-pressure medium, described below. For all experiment runs, the powdered sample was carefully pressed into a thin layer to achieve optimal thickness in order to avoid absorption saturation and loss of spectral features. For all high-pressure experiments, a ruby sphere was placed in the sample chamber for in-situ pressure determination and for low temperature, high pressure measurements, an additional ruby was placed on the diamond backplate for temperature correction (Datchi et al., 2007; Dewaele et al., 2008). A reference infrared spectrum (I_0) positioned off-sample in the sample chamber was taken at each pressure-temperature point to remove non-sample absorption features from the measured sample position (I). Absorbance (A) is then calculated by the following relation: $A = -\log_{10}(I_0/I)$, where I/I_0 is the transmittance. All data in this body of work are plotted as A vs. wavenumber (the number of wavelengths per unit of distance: cm^{-1}).

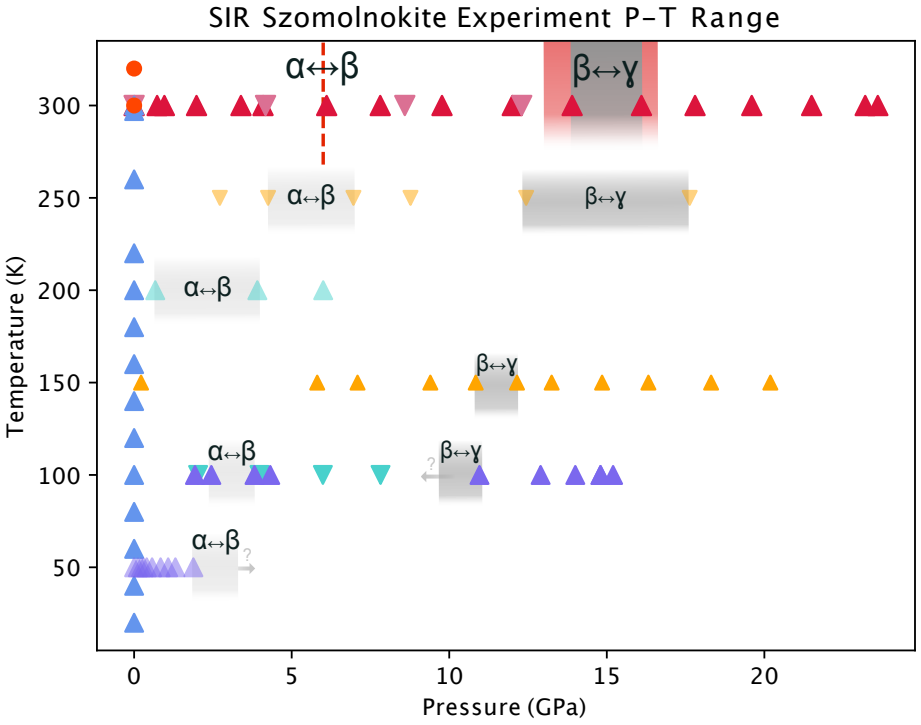

Figure 4.1: The pressure-temperature experiment range presented in this work. Symbol colors indicate compression-decompression cycles completed in one diamond anvil cell loading (i.e., a compression experiment was first conducted at 150 K up to 20 GPa, the sample was then heated to 250 K and decompressed). Upward pointing triangles indicate compression measurements, downward pointing triangles indicate decompression measurements. The upward pointing blue triangle series at 1 bar indicate that the sample was cooled to 20 K and subsequent measurements were taken upon incrementally heating the sample back to 300 K. Red dashed line and shaded region at 300 K indicate the structural transitions pressures measured at ambient temperature using X-ray diffraction (Meusburger, Ende, Talla, et al., 2019; Pardo, Dobrosavljevic, Perez, et al., 2023 Grey shaded regions indicate low-temperature transition pressures constrained in this work.

The 150 K compression/250 K decompression experiment run was gas-loaded with helium at Caltech using 500 μm flat culets. An initial FTIR reference spectrum was taken before cooling. The sample chamber diameter decreased from 205 μm in diameter to 150 μm immediately after helium loading at 0.3 GPa. The sample chamber diameter shrank significantly upon initial cooling to 150 K, so there was no empty anvil space in the chamber to measure a reference spectrum at each pressure. Instead, the only reference spectrum for this sample loading was collected at 0.3 GPa, which was used for all data points of the 150 K/250 K high pressure series. Ruby spectra indicated hydrostatic conditions throughout the entire pressure range. For all experiments, to account for any error in fitted ruby peak positions and observed heterogeneities in low temperature ruby profiles, error in pressure is taken to be 0.2 GPa for all measurements.

Quantum mechanics molecular dynamics

To construct a theoretical vibrational density of states and compare against our measured data, two quantum mechanics molecular dynamics simulations (QM-MD) were performed using the Vienna Ab initio Simulation Package (VASP) with generalized gradient approximation (GGA) of Perdew-Burke Ernzerhof (PBE) functional to describe the exchange-correlation energy. The DFT-D3 correction of (Grimme, Antony, et al., 2010; Grimme and Djukic, 2011) was used to account for van der Waals interactions. For all QM-MD calculations, a Γ-centered 1×1×1 k-point grid was used, and the plane wave energy cutoff was set at 500 eV. All QM-MD simulations used the isochoric-isothermal (NVT) ensemble using a Nosé-Hoover thermostat to set the temperature to 298 K (or 15 K). We chose an NVT ensemble due to the availability of ambient and low temperature single crystal X-ray diffraction data. Lattice parameters were fixed to the unit cell dimensions reported by Meusburger, Ende, Talla, et al. (2019) for the 298 K simulation, while the parameters reported by Wildner, Zakharov, et al. (2022) were used for the 15 K simulation. A single unit cell containing 36 atoms (4 Fe, 4 S, 8 H and 20 O) was used. Given the imposed isochoric restriction, the equilibrium pressures of the simulations (on average 4 kbar at 15 K and 13 kbar at 298 K) resulted from the choice of fixed lattice parameters and temperature, rather than being explicitly set as in the case of isobaric-isothermic (NPT) ensemble.

Each QM-MD simulation consisted of three stages: a heating stage, an equilibration stage, and a final production run at the target temperature. Each stage was simu-

lated with 1 fs time steps for 5, 3 and 60 ps, respectively. Atom trajectories were analyzed from the 60 ps production run stage to obtain the vibrational density of states (VDOS) using the Fourier transform of the velocity autocorrelation function (VACF). Upon inspection of the VACF and VDOS, while all atoms are moving in the simulation, some atoms are being underrepresented in the calculated VDOS. All crystallographic sites are represented, but the O-atoms are the most represented and S-atoms are the least represented. This in turn has affected the relative intensities currently predicted in the VDOS, and we expect that upon resolving this issue, existing portions of low-intensity modes will be filled out and overall noise of the VDOS will be reduced. Furthermore, a complete population of the predicted VDOS will allow for the calculation of the phonon density of states (PDOS). For this reason, we use VDOS to refer to the results of the QM-MD simulations and the phonon density of states to refer to the relevant experimental results, which is experimentally measuring phonons.

2.3 Spectra fitting procedure

All spectra were fit using the free, open-source software Fityk which performs user-guided background subtraction and a non-linear least squares fitting procedure using a starting set of peak parameters (Wojdyr, 2010). Each spectrum was pre-processed for background subtraction and diamond fringe removal in several sections, generally: 500-900 cm^{-1}, 900-1800 cm^{-1}, and 2500-4000 cm^{-1}. Diamond fringes (the interference of light between the faces of the diamond culet) were subtracted from each spectrum by taking the Fourier transform of the data and removing the fringe frequency interval.This method is successful starting at the wavenumber region of the ν_3 sulfate bands to the O-H stretching region (>1050 cm^{-1}). Below these wavenumbers, there are several sample peaks with widths on the order of the diamond fringe width and are thus affected by fringe removal. However, the diamond fringes shift in phase as a function of pressure, and they shift more rapidly than the sample features as a function of pressure. When viewing all spectra from temperature or pressure series on the same axes, it is clear which features results from diamond fringes, and which from the sample. Therefore, we can clearly identify sample features below 1050 cm^{-1} and fit these narrow features individually, masking out all other data. See the supplementary materials for greater detail on diamond fringe removal.

Peak shapes were fit with either Gaussian or Voigt profiles. Final fit parameters were taken as starting fit parameters for subsequent spectra, either the next compression

or decompression point or temperature. Where it is clear that multiple vibrational modes are overlapping, the minimum number of peaks was chosen to fit each observed grouping, and the resulting fit was chosen such that changes in peak position, height, and width were minimized. In taking this conservative approach we aim to report changes in spectra as a function pressure pressure/temperature that are due to changes in sample vibrations and not inconsistency with the reference spectrum, background subtraction, or non-unique models. Therefore, we report a set of vibrational mode positions that are self-consistent within each pressure-temperature series.

4.3 Results

Theoretical results and interpretation of mode assignments at 1 bar

The total predicted vibrational density of states (VDOS) at ambient conditions (1 bar, 300 K) is plotted in Figure 4.2 (see caveats stated in 2.1). The individual vibrational contributions from the Fe, S, O, and H atoms are also plotted below the total VDOS. Oxygen and iron vibrations dominate the <400 cm^{-1} lower wavenumbers with smaller contributions from sulfur and hydrogen vibrations. Iron has a small contribution at ~1500 cm^{-1} and an even smaller contribution at ~3600 cm^{-1}, suggesting a coupling with H_2O-related vibrations which dominate those regions. Hydrogen vibrational modes exhibit broad distributions in the 3000 cm^{-1} region and 1500 cm^{-1}, supporting the presence of many vibrations in each wavenumber region. Upon closer inspection of individual vibrations, our theoretical work predicts the presence of IR-active water-libration modes at ~835 cm^{-1}, which we experimentally observe and has been previously identified in experimental work (ranging from 816-850 cm^{-1}) as H_2O librations and purported as a monohydrate sulfate diagnostic peak (Lane, 2007, Lane, Bishop, et al., 2015, Talla and Wildner, 2019). Throughout the <850 cm^{-1} region, a series of water libration modes are observed (with a peak at ~530 cm^{-1}), associated with all or various subsets of the H_2O groups, again supporting multiple hydrogen-bonding environments at ambient conditions.

At low wavenumbers between 90-350 cm^{-1}, the predicted VDOS is in good agreement with the experimentally measured ^{57}Fe partial projected phonon density of states (pPDOS) of szomolnokite, shown in Figure 4.3 (Pardo, Dobrosavljevic, Sturhahn, et al., 2023). General band assignments for the Fe^{2+}-O, S-O, SO_4 and H_2O IR-active modes and their predicted positions are indicated underneath the spectra in Figure 4.3. The four predicted maxima approximately centered at 90, 140, 210 and 275

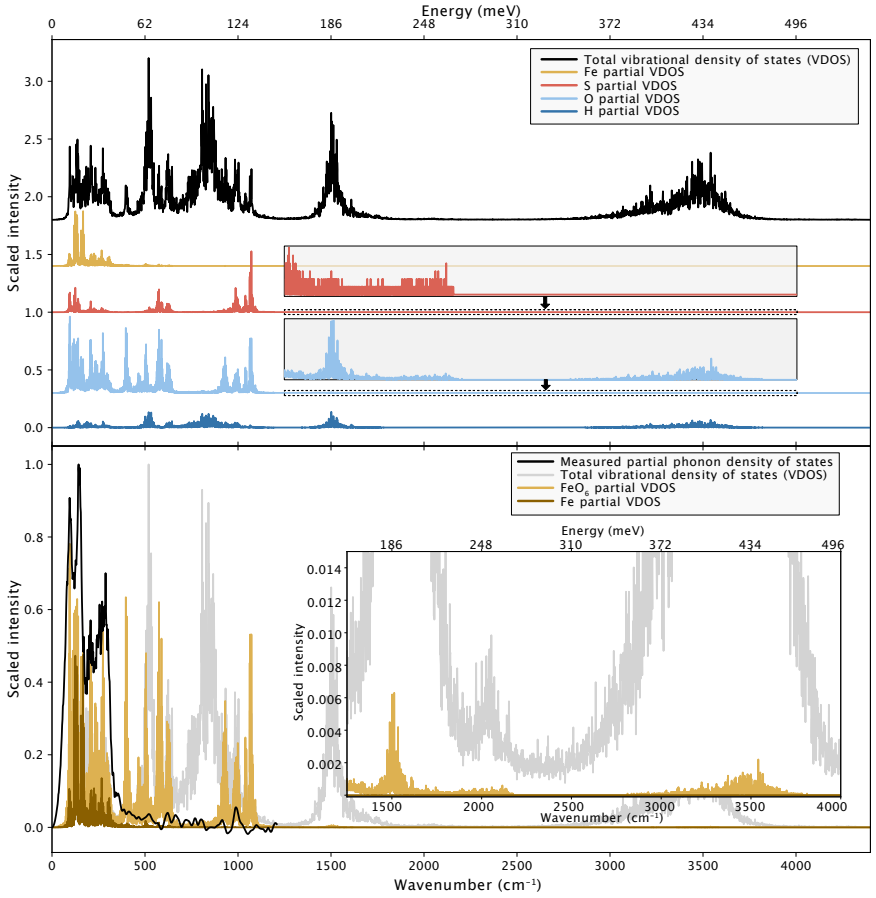

Figure 4.2: Calculated vibrational density of states and measured phonon density of states. **Top:** Calculated vibrational density of states (VDOS) and the individual atomic contributions. **Bottom:** The measured ^{57}Fe partial phonon density of states (pPDOS), the calculated contributions from individual iron atoms and FeO_6 octahedra, and the total VDOS. Intensities for the predicted individual atomic contributions and FeO_6 contributions are unaltered; the predicted total VDOS and measured pPDOS are scaled for visualization purposes. The relative individual contributions to the total VDOS may be affected by the underrepresentation of particular atoms as discussed in the text.

cm^{-1} line up almost exactly with the measured maxima, and the absolute maximum within the 0-400 cm^{-1} region for both the pPDOS and VDOS are centered at ~140 cm^{-1}. Inspection of the individual predicted vibrations in this region confirm they are a combination of predominantly Fe^{2+}-O and S-O vibrations. Although parabolic, the predicted relative intensities in the wavenumber region <90 cm^{-1} do not match the experimentally measured pPDOS.

Within the FTIR measured wavenumber region, factor group analysis (the method of determining unique vibrational modes based on a collection of atoms' structure and symmetry) of low symmetry, anharmonic environments predicts up to three ν_3 (asymmetric stretching), one ν_1 (symmetric stretching), three ν_4 (asymmetric bending), and two ν_2 SO_4 (symmetric bending) modes; and one ν_2 H_2O (bending), one ν_1 H_2O (symmetric stretching), and one ν_3 H_2O (asymmetric stretching) modes (Grodzicki and Piszczek, 1998; Majzlan et al., 2011). The infrared data do not extend to the Fe-O dominated wavenumber region, but are in good agreement with predicted positions of high intensity modes <1020 cm^{-1}. In the 400-800 cm^{-1} region, four distinct peaks are visible at ~535, 605, 625, 665 cm^{-1}. Three degenerate ν_4 SO_4 modes are predicted in this region (due to asymmetry in the tetrahedral bonding environment), but four modes have been previously observed (e.g., Lane, 2007; Talla and Wildner, 2019). Lane (2007) assigns the first three to ν_4 SO_4 and the highest wavenumber mode to a CO_2 contaminant; other studies have assigned all to ν_4 SO_4 or left them unassigned. When the lowest wavenumber mode is observed, it is ubiquitously broader and more intense than the high wavenumber peaks, which all have similar profiles. Importantly, our QM-MD simulations predict a strong H_2O libration at 530 cm^{-1}. Thus, given the comparative profiles of these four peaks and QM-MD results, we assign the 533 cm^{-1} mode to ν_L H_2O and the 605, 625, and 665 cm^{-1} modes to the three degenerate ν_4 SO_4 modes.

While the observed ν_1 SO_4 mode at 1018 cm^{-1} is predicted by the VDOS, the measured sulfate ν_3 region at ~1100 cm^{-1} is not well-predicted. Even including predicted IR-active bands of extremely low intensity (<0.1% of the maximum predicted intensity for all IR-active modes), the portion of measured bands between 1100-1250 cm^{-1} is not represented. As discussed in section 2.1, further improvements of the VDOS construction to include underrepresented atoms should increase the intensity of S-participating vibrations, which are concentrated in this 1100-1250 cm^{-1} region. Furthermore, the ν_3 SO_4 mode is triply degenerate; in ideal, highly symmetric and harmonic systems, only one ν_3 mode exists at ~1100 cm^{-1}, which is

predicted by the current VDOS. The two degenerate ν_3 modes may be better sampled as improvements to the VDOS construction are implemented. The broadness of the experimentally observed distribution of ν_3 SO_4 modes is similar to other work, and we assign three ν_3 SO_4 modes to the experimentally measured 1100-1250 cm^{-1} region.

Reference	ν_1 SO_4 stretch	ν_2 SO_4 bend	ν_3 SO_4 bending	ν_4 SO_4 bend	ν_1, ν_3 H_2O stretch	ν_2 H_2O bending	H_2O Librations
Adler and Kerr, 1965 FTIR	1016	Spectral region not measured	1093 1136 1164*	Spectral region not measured			
Cloutis et al., 2006 Reflectance	1018	427	1087 1099 1163 1227* 1266*	565 606 629 667 690	3390 3268	1681 1637	833
Chio, Sharma, and Muenow, 2007 Raman	1018	423 492	1073 1095 1194	615 623 661	3137 3246 3333 3410	1478 1630 1735	850
Lane, 2007 Mid-IR thermal emission FTIR	1018	361	1149 1195 1226	554 606 626	– – –		846
Majzlan et al., 2011 FTIR	1014	Spectral region not measured	1050 1071 1141*	Spectral region not measured	3078* 3232 3290* 3394*	1490 1651	816
Meusburger, Ende, Talla, et al., 2019 FTIR	1000*	Spectral region not measured	1075* 1160*	Not observed	3140* 3230* 3340* 3440*	1480 1535* 1650 1740	850*
Talla and Wildner, 2019 Raman	1018	423 494	1071 1090 1195 1283	617 623	3247 3368	1478	850*
FTIR	1015	Spectral region not measured	1100* 1133 1170*	600* 620* 665*	3150* 3245 3340* 3391	1496 1630*	535* 831
This work FTIR	1016	Spectral region not measured	1083 1133 1191	603 624 667	3122 3260 3374 3434	1432 1490 1642	533 831

Table 4.1: Reported vibrational modes for szomolnokite at 1 bar. All units are in wavenumbers (cm^{-1}). Modes with an asterisk (*) were visually identified in the published spectrum and their position was approximated from a digitized plot of the data.

The predicted IR-active H_2O ν_2 bending mode lies within the general vicinity of the measured peak at ~1490 cm^{-1}. Although not IR-active, the VDOS does predict a distribution of low-intensity vibrational modes under the secondary peak at 1430 cm^{-1} and the broad feature at ~1650-1750 cm^{-1}. The higher wavenumber feature is observed in our data and in all other szomolnokite IR and Raman measurements, as well as other kieserite-type structure minerals spectra discussed in section 1.2, and has been interpreted as additional H_2O ν_2 bending-related modes originating from coupling of H_2O molecules with each other, and coupling of H_2O molecules with

quasi-internal modes of iron octahedra and sulfate tetrahedra (Chio, Sharma, and Muenow, 2007; Grodzicki and Piszczek, 1998). We assign this mode ν_{2-C}(coupled bending mode). This coupling hypothesis may explain the broad feature at ~1650-1750, but not the 1430 cm^{-1} feature observed in our data. See Table 4.2 for published IR, Raman, and reflectance-identified modes.

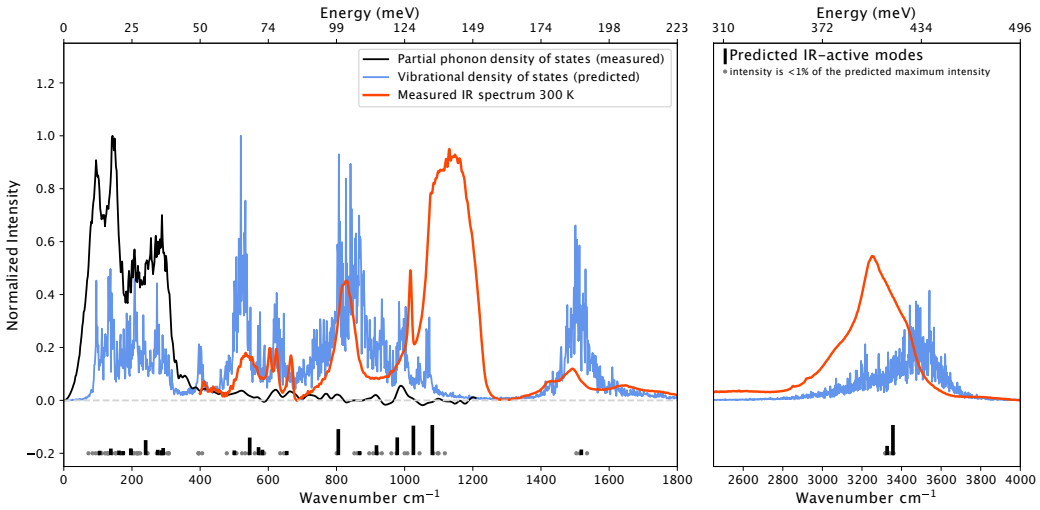

Figure 4.3: Comparison of QM-MD simulation calculated VDOS (blue), the measured ^{57}Fe pPDOS (black), and measured IR spectrum (red). The region between 1800-2500 cm^{-1} contains noise from the diamonds and is not plotted. IR-active modes predicted from the QM-MD simulations are plotted below the spectra.

In the O-H stretching 3000-3500 cm^{-1} region, a broad distribution of vibrational modes is predicted, nominally forming two maxima at 3250 cm^{-1} and 3400 cm^{-1} (right shoulder). Consistent with previous band assignments, the measured maximum at 3250 cm^{-1} is attributed to the symmetric O-H stretching mode ν_1, while the right shoulder of the observed distribution is attributed to the antisymmetric stretching mode ν_3. A previously reported peak positioned between the ν_1 and ν_3 modes has not been assigned to a particular band in the literature, but the low-wavenumber population of modes centered at ~3100 cm^{-1} has been attributed to a H_2O ν_2 overtone ($2\nu_2$), whose intensity is magnified by Fermi resonance with the H_2O ν_1 mode (Chio, Sharma, and Muenow, 2007).

While the $2\nu_2$-ν_1 Fermi resonance can explain the observed and predicted population of vibrational modes at wavenumbers lower than the ν_1 symmetric stretching peak, it cannot explain the ubiquitously observed peak between the ν_1 and ν_3 modes, nor the additional split 1430-1490 cm^{-1} ν_2 observed at lower wavenumbers. Using

our QM-MD simulations, we offer an explanation to these latter features. We extracted oxygen-oxygen distances between hydrogen bridges (O_{water}-O) in the crystal unit cell at 298 K and 15 K (Figure 4.4). At 300 K, four individual distance distributions best-fit the total distribution, implying four unique bonding environments, even though there is only one crystallographically unique O_{water} site. These O_{water}-O distances have been related to observed stretching frequencies, where shorter distances exhibit exponentially lower wavenumber band positions compared to longer O_{water}-O distances (Libowitzky, 1999). One, structurally and environmentally unique water site would theoretically give rise to one symmetric and one antisymmetric stretching mode. The predicted distribution of O_{water}-O distances implies greater than two O-H stretching frequencies ranging from ~2650-3500 cm^{-1}, according to the Libowitzky, 1999 O_{water}-O distance-frequency dependence model. Meusburger, Ende, Talla, et al., 2019's reported O_{water}-O distances for szomolnokite at 1 bar ranged from 2.75 Å to 3.24 Å, corresponding 3250 cm^{-1} and 3600 cm^{-1} stretching frequencies, respectively. Libowitzky, 1999 additionally presents a H-O distance-frequency dependence model. Recent neutron diffraction experiments constrained the hydrogen positions of rozenite ($FeSO_4 \cdot 4H_2O$), measuring distances up to 2.55 Å and down to 1.76 Å, which would correspond to O-H stretching frequencies between 3050 and 3500 cm^{-1} (Meusburger, Hudson-Edwards, et al., 2022).

While Fermi resonance between the $2\nu_2$-ν_1 H_2O may certainly contribute to the observed distribution of modes in the 3000 cm^{-1} region, the results of our QM-MD simulations and existing experimental data support the need for more than one set of ν_1 and ν_3 modes in order to fit the O-H stretching region accurately. Four unique O-H bonds may exhibit up to eight unique stretching modes, but accurately deconvolving eight peak profiles within the measured broad distribution is infeasible. In our ambient condition data (300 K, 1 bar), szomolnokite's O-H stretching region is well fit by four peaks, a strategy employed in previous studies (e.g., Chio, Sharma, and Muenow, 2007; Meusburger, Ende, Talla, et al., 2019; see Table 1). Therefore, we assign the four fitted peaks to two sets of ν_1 and ν_3 modes in the 3000-3500 cm^{-1} region arising from a distribution of hydrogen bonding environments within the crystal structure. In the bending mode region, we assign an additional H_2O ν_2 mode that we assign as ν_{2b} at 1430 cm^{-1} (see Figure 4.5).

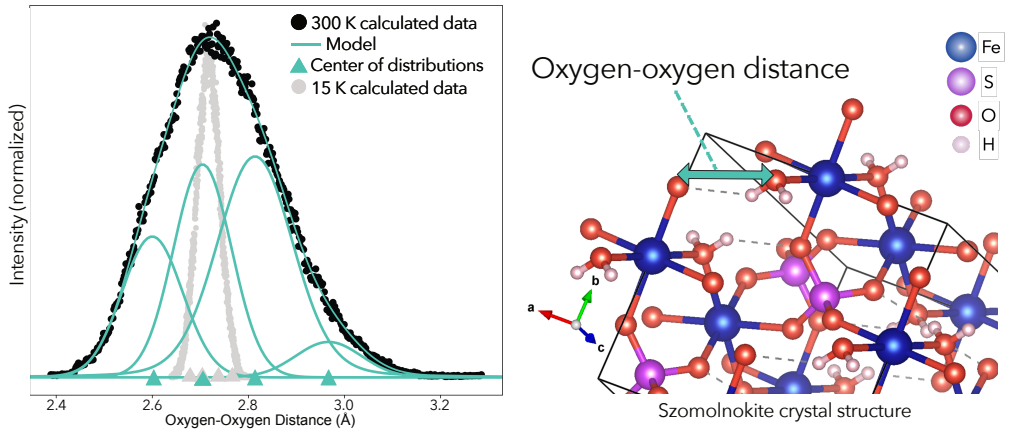

Figure 4.4: Oxygen-oxygen distance distributions for the hydrogen bonded O-O_{water} atoms for the calculated 300 K and 15 K molecular dynamic simulations. **Left:** Four Gaussian-type distributions best-fit the 300 K and 15 K distributions. **Right:** The szomolnokite crystal structure with an arrow indicating the O-O_{water} distance.

Synchrotron FTIR results

3.2.1 Low temperature (1 bar): 300 K to 20 K

We assign all modes as discussed in section 3.1 and labeled in Figure 4.5. Upon cooling to 20 K, a slight temperature dependence is exhibited by all identified vibrational modes plotted in Figure 4.5 (600-1700 cm^{-1}) and Figure 4.6 (3000-3500 cm^{-1}). The largest changes occur in the intensities of individual modes relative to others. For example, the 850 cm^{-1} H_2O libration mode, ν_1 SO_4, and ν_1 H_2O peaks all significantly increase in intensity relative to the rest of the spectrum. The relative increase in intensity of the ν_{2-C} H_2O 1650 cm^{-1} peak at low temperature has also been observed in szomolnokite and other kieserite-type structures (Grodzicki and Piszczek, 1998). At 20 K, the ν_1, ν_3, ν_{1b}, ν_{3b} modes are better resolved (see Figure 4.6). Additionally, a broad, low-intensity fifth peak may be identified at ~2850 cm^{-1}, likely associated with the $2\nu_2$-ν_1 resonance peak discussed in section 3.1. Wildner, Ende, et al. (2021) performed single crystal X-ray diffraction measurements down to 15 K and did not observe any phase transition to occur in szomolnokite. Wildner et al. (2021) note that the thermal pressure effect of cooling the sample to 15 K is equivalent to pressures of 0.7 GPa at 300 K, suggesting a lower bound in pressure for the $\alpha - \beta$ transition (i.e., the $\alpha - \beta$ transition must occur above 0.7 GPa at temperatures $\geq$15 K).

Using Mössbauer spectroscopy, Alboom et al. (2009) have reported a magnetic order-disorder transition occurring in szomolnokite at 29.6 K at 1 bar. This transition is potentially reflected in the deviation in peak positions in our data visible between the 60, 40, and 20 K data points for the sulfate ν_1 and ν_3 modes in Figure 4.5 and the ν_{1b} mode in Figure 4.6. Upon heating the sample back up to ambient temperature, the peak intensities return to approximately the same intensities pre-cooling, except for the sulfate ν_3 modes which are lower in intensity. Because Mössbauer spectroscopy is much more sensitive to Fe-site changes than X-ray diffraction, it is not surprising that Wildner, Ende, et al. (2021) did not observe any indication of the magnetic transition in their low-temperature data. However, Alboom et al. (2009) concluded that the asymmetry of the local ^{57}Fe electric field gradient quantified in the Mössbauer data is strongly affected by the proximity of H_2O molecules, suggesting a connection between changes in hyperfine parameters during the magnetic transition and H_2O bonds.

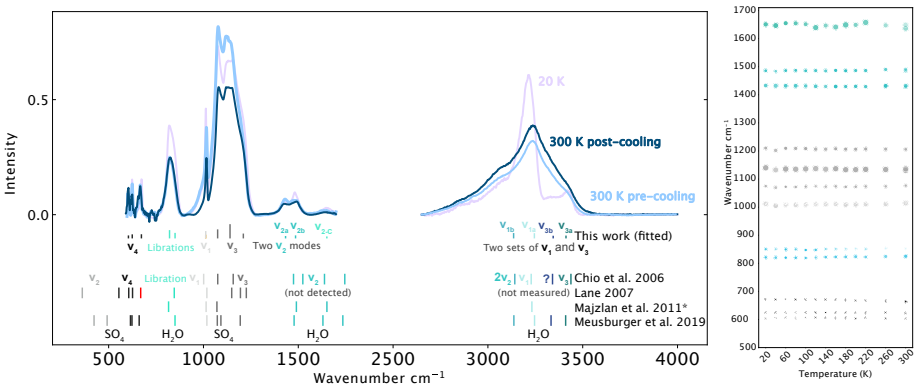

Figure 4.5: Low temperature spectra and peak positions. **Left:** Select spectra from the low temperature series plotted on the **left** demonstrating spectral changes occurring between 297 K and 20 K, and the reversal of spectral changes upon raising the sample temperature back to 300 K. Assigned modes from existing data are plotted below; this work's updated assignments plotted above (see Table 1 description) **Right:** Peak positions as a function of temperature in the 500-1700 cm^{-1} region. Symbol sizes represents the full-width half maximum of each peak. Symbol opacity represents the peak's height, relative to itself across the temperature series.

Ambient temperature (300 K), high pressure, 1 bar to 23 GPa

Figure 4.7 plots all data from the ambient temperature, high pressure series spanning 1 bar to 23 GPa. In general, as modes mover towards higher wavenumbers the associated bond becomes stronger and more energetic, whereas movement towards lower

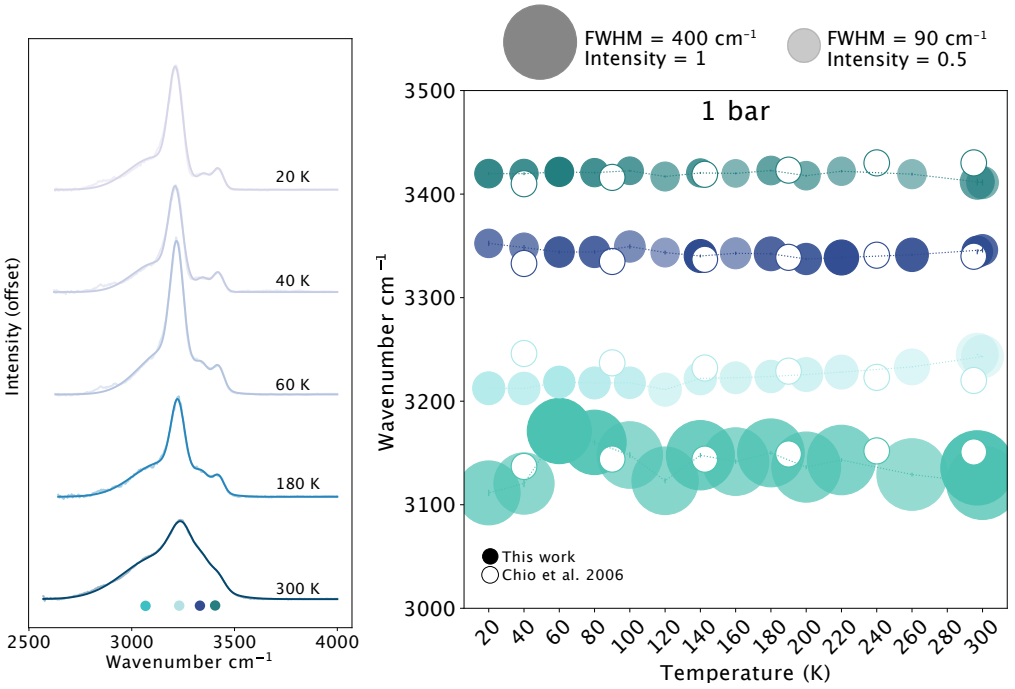

Figure 4.6: Select spectra from the low temperature series demonstrating spectral changes occurring between 300 K and 20 K for the H_2O stretching region. Right: fitted peak positions for the ν_{1a}, ν_{1b}, ν_{3a}, and ν_{3b} modes. Symbol sizes represent the full-width half maximum (FWHM) of each peak. Symbol opacity represents the peak's height, relative to itself across the pressure series, as indicated by the example data points above the figure.

wavenumbers indicates a weakening of bond. These trends are complicated in the presence of phase transitions and changes in bonding characteristics, as discussed below. Upon increasing pressure to 4 GPa, all SO_4 modes shift to higher wavenumbers, except for the highest wavenumber ν_3 mode which is static within error. The behavior of the H_2O-related mode positions is more complicated: the 535 cm^{-1} ν_L and 835 cm^{-1} ν_L modes increase by 6 and 14 cm^{-1}, respectively, bending modes ν_{2a} is static and ν_{2b} decreases by 6 cm^{-1}, the ν_{2-C} mode increases by 10 cm^{-1}, and stretching modes ν_{1b} and ν_{3a} are nominally static, while ν_{1a} and ν_{3b} decrease by 40 and 20 cm^{-1}, respectively.

At the α-β transition pressure (6 GPa), two significant spectral changes occur that are diagnostic of the structural transition: the H_2O ν_{2-C} mode disappears and the negative pressure dependence of the H_2O $\nu_{1a}$and ν_{1b} mode positions significantly increases in rate compared to their antisymmetric ν_{3a} and ν_{3b} counterparts. As described in Meusburger, Ende, Talla, et al. (2019), the α-β structural transition is

marked by the bifurcation of the hydrogen-bonding system caused by the tilting of the tetrahedra and octahedra, which in turn creates a second octahedral site. In the FTIR data, these structural changes are most reflected in the H_2O-related modes. The downward shift of the ν_{1a} and ν_{1b} modes indicates increased hydrogen-coordination within the crystal structure: as the hydrogen atom becomes more strongly coordinated with nearby atoms, the O_{water}-H bond becomes less energetic, driving the $\nu_{1a}$and ν_{1b} modes to lower wavenumbers. With increasing pressure approaching the β-γ transition, both of the antisymmetric modes display an initial shift towards lower wavenumbers before inflecting at ~9 GPa and moving back towards higher wavenumbers. It should be noted that the ν_{2a} and ν_{2b} stretching modes exhibit a reversed inflection behavior at a smaller scale, moving towards high wavenumbers then lower wavenumbers over the range of ~10 cm^{-1}. The loss of the H_2O ν_{2-C} mode suggests a decoupling of the H_2O ν_2 bending mode(s) with the other H_2O molecules and/or octahedra/tetrahedra. This may be related to the reduction in symmetry from the monoclinic $C2/c$ α-phase to the triclinic $P\bar{1}$ β-phase. This symmetry-related coupling is further supported by the reappearance of the ν_{2-C} upon increasing pressure into the higher symmetry monoclinic $P2_1$ γ-phase stability field.

The β-γ structural transition was reported to occur between 12.7-16.8 GPa (Pardo, Dobrosavljevic, Perez, et al., 2023). Using the reappearance of the ν_{2-C} mode discussed above and the significant deviations in peak positions of multiple modes as diagnostics of the structural phase transition, we now bracket the β-γ transition between 14-16 GPa at ambient temperature. Between 14 and 16 GPa, the 535 cm^{-1} ν_L mode broadens and jumps towards higher wavenumbers before narrowing and increasing intensity through 23 GPa. The lowest wavenumber SO_4 ν_4 mode stagnates across the remaining pressure range, but the higher wavenumber ν_4 modes both begin to rapidly move towards higher wavenumbers. The 835 cm^{-1} ν_L mode significantly drops in intensity but does not exhibit significant deviations in its center frequency pressure-dependence. The SO_4 ν_1 mode similarly decreases intensity while steadily moving towards higher wavenumbers. Simultaneously, a second peak centered ~25 cm^{-1} lower appears and grows in intensity. This could be attributed to a second, structurally distinct tetrahedral site with its own set of ν_1 and ν_3 modes. This is supported by the broadening of the ν_3 distribution. Although we still fit only three modes due to the inability to resolve individual peaks, additional peaks belonging to new SO_4 ν_3 could fit the data.

The new ν_{2-C} mode at ~1575 cm^{-1} continues to grow in intensity but its center fre-

quency does not show significant pressure dependence. Conversely, the ν_2 bending modes both shift to low wavenumbers abruptly at 20 GPa, then move back towards higher wavenumbers. This behavior is preceded by the sharp shifts toward lower wavenumbers of all four ν_1 and ν_3 stretching modes at 16 GPa, with the symmetric stretch ν_{1a} and ν_{1b} modes exhibiting the most extreme movement. The ν_{1a} then upshifts slightly before stagnating for the remainder of the compression points, while ν_{1b} simply stagnates at ~2800 cm^{-1}. Antisymmetric modes ν_{3a} and ν_{3b} behave similarly to ν_{1a}, but at high wavenumbers. Four decompression measurements were taken between 17 GPa and 1 bar. The 1 bar post-experiment decompression spectra are plotted in each panel in Figure 4.7. Peak positions exhibit hysteresis with decreasing pressure, but by 1 bar the changes described in this section are reversible and peaks return to their approximate pre-compression positions. Peak positions at the four decompression measurement pressures for the H_2O stretching modes are plotted in Figure 4.7d.

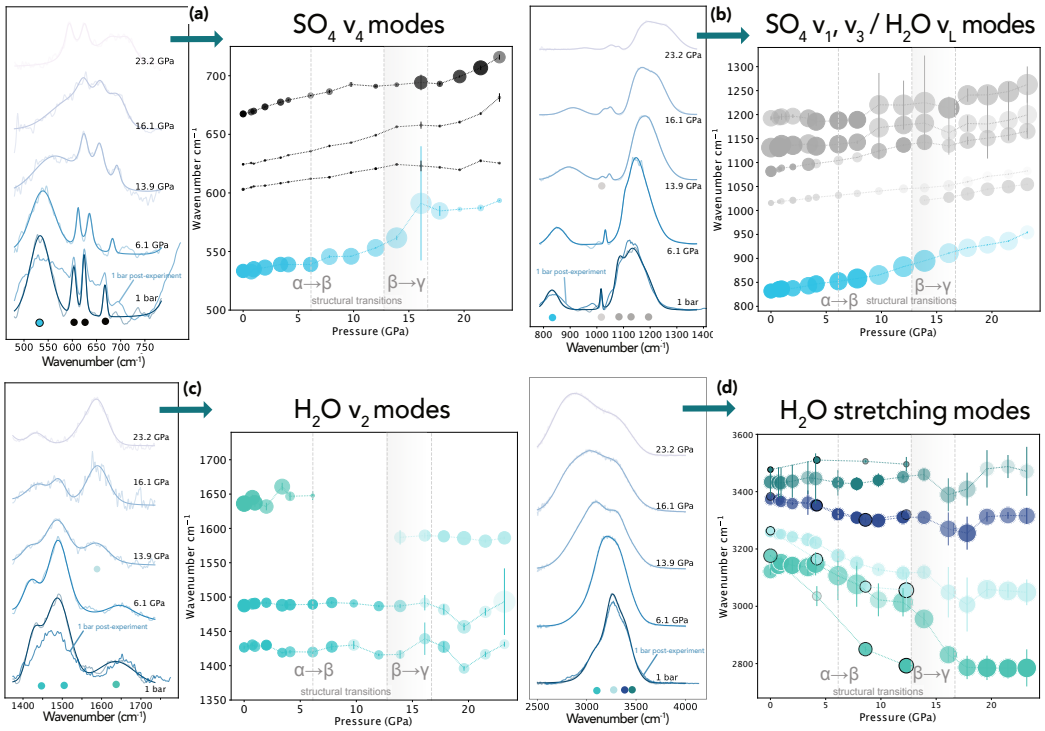

Figure 4.7: Select regions from select spectra of the 300 K high pressure series and the fitted peak positions as a function of pressure. Dashed line and shaded region indicate the structural transitions determined by Meusburger, Ende, Talla, et al. (2019) and Pardo, Dobrosavljevic, Perez, et al. (2023) Symbol sizes represent the full-width half maximum of each peak. Symbol opacity represents the peak's height, relative to itself across the pressure series.

High pressure, low temperature: 50 to 250 K and 1 bar to 18 GPa

Figures 8-14 contain the measured spectra for each low temperature compression and decompression series performed between 50 and 250 K (see section 3.2.2 for discussion of 300 K compression and decompression series). From our analysis of the ambient temperature high pressure series discussed in section 3.2.2, we focus on using the changes in H_2O-associated modes as a diagnostic of the α-β and β-γ structural transitions. Table 2 summarizes the transition pressure range for each low temperature compression/decompression series. See Figure 4.1 for a schematic of these results.

Temperature	α-β transition pressure	β-γ transition pressure
300 K Pardo, Dobrosavljevic, Perez, et al., 2023 XRD	5.0-6.6 GPa*	12.7-16.8 GPa
300 K (compression)	4.1-6.1 GPa	13.9-16.1 GPa
250 K (decompression)	4.3-7.0 GPa	12.4-17.6 GPa
200 K (compression)	0.7-3.9 GPa	Pressure range not sampled
150 K (compression)	<5 GPa	10.8-12.2 GPa
100 K (compression)	Pressure range not sampled	<12 GPa
100 K (decompression)	2.0-4.0 GPa	Pressure range not sampled
100 K (compression)	2.5-3.8 GPa	Pressure range not sampled
50 K (compression)	>2.0 GPa, partially observed	Pressure range not sampled

Table 4.2: Summary of transition pressures for the α-β= and β-γ structural transitions at 300 K reported by X-ray diffraction and the low-temperature transition pressures determined by FTIR in this work (see text for discussion). For experiments that did not cover the pressure range in which either the α-β or β-γ transition occurs, "Pressure range not sampled" is stated.
Meusburger, Ende, Talla, et al., 2019 determined the α-β transition at 6.15 GPa.

Decompression series at 250 K (Figure 4.8a): Note that this decompression series was performed after the 150 K compression series. At ambient temperature, we observed the vibrational modes exhibit hysteresis behavior upon decompression and thus expect the 250 K series to include some level of hysteresis. This decompression series (and 150 K compression series) was performed in the He-loaded DAC described in section 2.1, thus the use of a single reference spectrum (at 0.3 GPa) made it difficult to resolve many features. Nevertheless, the significant shift in H_2O stretching region maximum between 12.4-17.6 GPa is indicative of the reversal of the γ-β transition. The slight decrease in the symmetric stretching mode wavenumber position observed in the β-phase stability field prior to shifting to higher wavenumbers in the γ-phase is similar to what we observed during the α-β transition at 300 K.

Compression series at 200 K (Figure 4.8b, 4.9): The 200 K compression series samples fewer compression points and differs from the 300 K data in that the ν_{1a}

and ν_{1b} modes center positions are very closely spaced, but the ν_{1b} mode is still broader than ν_{1a} like in the 300 K data. Movement towards lower wavenumbers is greater between 0.7 and 3.9 GPa than 3.9 and 6.0 GPa (see Figure 4.8b). This is also accompanied by an increased splitting of the 835 cm^{-1} ν_L modes, which we assign as indications of the α-β transition (see Figure 4.10).

Compression series at 150 K (Figure 4.8c, 4.10): These measurements were conducted in the same DAC as the 250 K decompression series. Due to the coarse sampling in the low pressure interval (<5 GPa), the 150 K compression series does not appear to resolve spectral indications of the α-β transition. At higher pressures, the β-γ transition can be identified. Between 10.8 and 12.2 GPa, the H_2O ν_{1b} mode reaches a minimum wavenumber position before moving back towards higher wavenumbers. Simultaneously, the ν_{3b} mode begins to shift towards lower wavenumbers. This is accompanied by a minimum in intensity in the 535 cm^{-1} ν_L mode, which then narrows and increases in intensity upon increasing pressure. Significant changes in the relative intensities of the 835 cm^{-1} ν_L and ν_2 modes occur, along with slight shifts in wavenumber that within error are more abrupt than the preceding compression points. These spectral features are the strongest indications the β-γ transition is occurring between 10.8 and 12.2 GPa.

Interestingly, three 835 cm^{-1} ν_L modes are identified, and a second ν_L mode was an identified in the 200 K series, suggesting that low temperatures may allow multiple libration modes to be resolved from the broad 835 cm^{-1} ν_L observed at ambient temperature. For the 150 K series, the lowest wavenumber ν_L modes in the 835 cm^{-1} region may be an artifact of the reference spectrum. Additionally, we can only resolve the ν_{2-C} mode at ~1650 cm^{-1} at 14.8 and 16.3 GPa, but due to the high noise in the spectrum it is possible it appears by 12.2 GPa at 150 K.

100 K series

Decompression series at 100 K (Figure 4.8f, S7): These measurements followed the 200 K compression series in the same DAC. We observe a merging of the ν_{1a} and ν_{1b} modes at 4 GPa, which was similarly observed in the 300 K compression series at the identified α-β transition. The reversal of the α-β transition occurring between 4 and 2 GPa is further supported by the following observations at 2 GPa: appearance of the ν_{2-C} mode, as well as the marked broadening and relative intensity changes exhibited by the two identified 835 cm^{-1} ν_L modes (see Figure 4.8 panel d).

Compression series at 100 K (Figure 4.8e, 4.11, 4.12): Two 100 K compression

series were performed within 1.9-4.3 GPa and 12.9-15.2 GPa intervals in the same DAC (see Figure 4.1). The high-pressure interval was completed upon compressing the sample to 4.3 GPa, warming to ambient temperature and subsequently increasing pressure to 10.8 GPa, then cooling to 100 K (which simultaneously increased the pressure to 12.9 GPa). The α-β transition is identified at 2.5-3.8 GPa, using the marked changes in relative intensity exhibited by the following modes: 535 cm^{-1} ν_L, the two 835 cm^{-1} ν_L modes, and ν_{2a} and ν_{2b}. It should be noted that the ν_{2-C} mode is observable throughout the 1.9-4.3 GPa interval, unlike the 100 K decompression series within the same pressure range. The fourth, highest wavenumber peak in the ν_3 SO_4 region observed in both pressure intervals is likely attributed to the SO_4 Reststrahlen band, also identified in the 100 K decompression and 150 K compression series. Reststrahlen bands arise from reflectivity phenomena and depend on sample properties such as grain size, and always occur at slightly higher wavenumbers than the strongest absorption band (Rubens and Nichols, 1897). Reststrahlen bands are a general phenomena and have been identified in several hydrous sulfates spectral studies (Cloutis et al., 2006; Talla and Wildner, 2019; Witzke, Arnold, and Stöffler, 2007). No significant changes indicate the occurrence of the β-γ within the 12.9-15.2 interval.

Compression series at 50 K (Figure 4.8g, 4.13): The 50 K series between 1 bar and 2 GPa is extremely well sampled and shows no indication that the α-β transition has occurred. As observed in higher temperature series upon increasing pressure approaching the transition, the two 535 cm^{-1} ν_L modes and two 835 cm^{-1} ν_L modes broaden, but no significant changes in relative intensity are observed. The ν_{3b} becomes more intense with increasing pressure, similar to what occurs in the ambient temperature series just below the α-β transition. Therefore we identify the α-β transition to occur at >2 GPa at 50 K.

4.4 Conclusions

Our QM-MD simulations support the complexity of hydrogen bonding and generation of wide distributions of bonding environments observed in our experimental data. We offer multiple, vibrationally-unique H_2O sites as an explanation for the number of H_2O-related modes observed in the literature that exceed the expected amount (i.e., four modes are observed in the H_2O-stretching region and two in the H_2O-bending region). Our high pressure and low temperature data indicate that the H_2O related modes are the most affected by the structural transitions and thus their

center position, broadness, and relative intensities have been used as a diagnostic for identifying szomolnokite's α-β and β-γ structural transitions and constructing a schematic *P-T* diagram illustrating the temperature dependence of these transitions. Structurally, the tilting of the iron octahedra/sulfate tetrahedra are the largest changes in the crystal lattice that occur during the α-β monoclinic-triclinic transition, but the corresponding changes in hydrogen bonds may alter the subsequent compression mechanisms (Meusburger, Ende, Talla, et al., 2019; Nazzareni et al., 2010). Hydrogen-bond related lattice stiffening has been identified in other sulfate compositions, like Jarosite, in which a continuous structural transition is attributed to stiffening of intralayer hydrogen bonds (Klein et al., 2018). We observe several changes in the H_2O vibrational modes compression behavior as a function of pressure, indicating both stiffening and softening related to the structural transitions. The results of this work support the ability to use FTIR data as structural phase transition identification.

At low temperatures, our data suggest the transformation to the denser β and γ-phase occurs at lower pressures, compared to 300 K. This behavior indicates a positive Clapeyron slope for both phase transitions. Due to the cooler, interior temperature profiles of the icy satellites, the β and γ-phase transitions would occur at shallower depths compared to warmer planetary bodies. Local environments that are warmer compared to their surroundings, for example an impact site, may then remain more buoyant as the α and β phases remain structurally stable to greater depths. The reversibility behavior observed in our post-experiment 1 bar measurements imply full reversibility of the structural transitions. Specifically, throughout the entire pressure-temperature range sampled here, all modes associated with the water molecules were preserved upon compression and decompression. Hydrous sulfates, and in particular monohydrated sulfates, may act as stable water-carriers into the deep interiors of icy, sulfur-rich planetary bodies and participate in volatile cycling upon recycling to the surface.

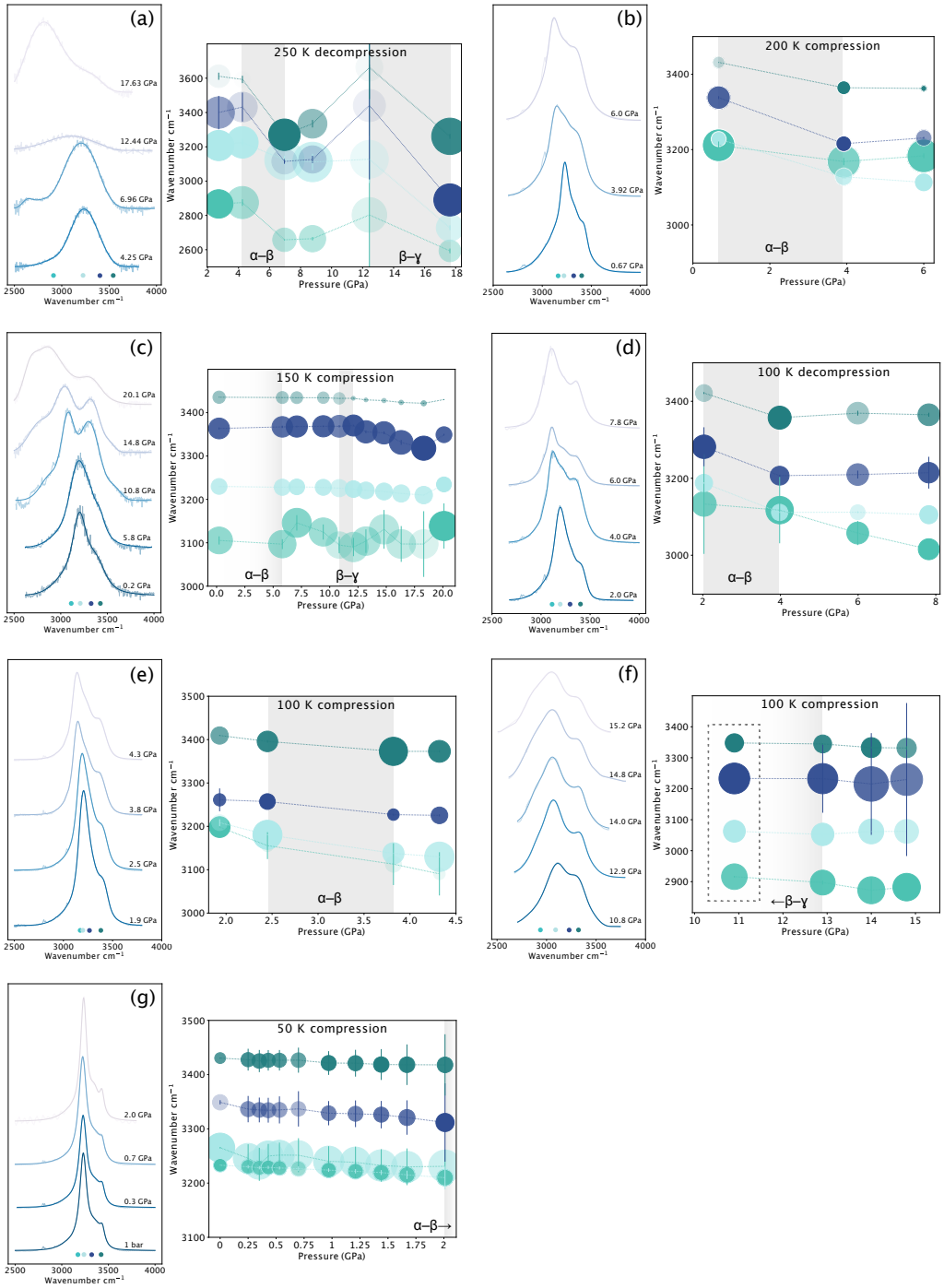

Figure 4.8: H_2O stretching region for each low temperature, high pressure dataset and the fitted peak positions. Symbol sizes represent the full-width half maximum of each peak. Symbol opacity represents the peak's height, relative to itself. For specific mode assignments, see Figure 4.5.

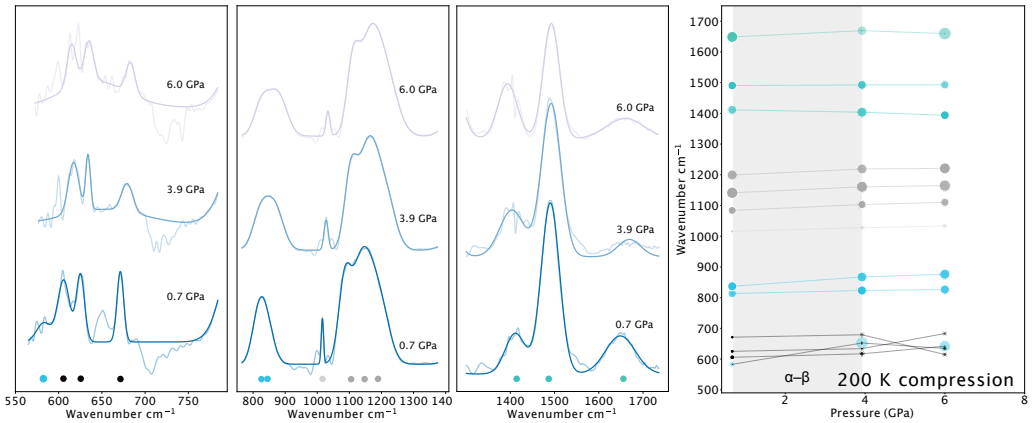

Figure 4.9: Select spectra from the 550-1700 cm^{-1} region for the 200 K high pressure dataset and the fitted peak positions for all data. Symbol sizes represent the full-width half maximum of each peak. Symbol opacity represents the peak's height, relative to itself.

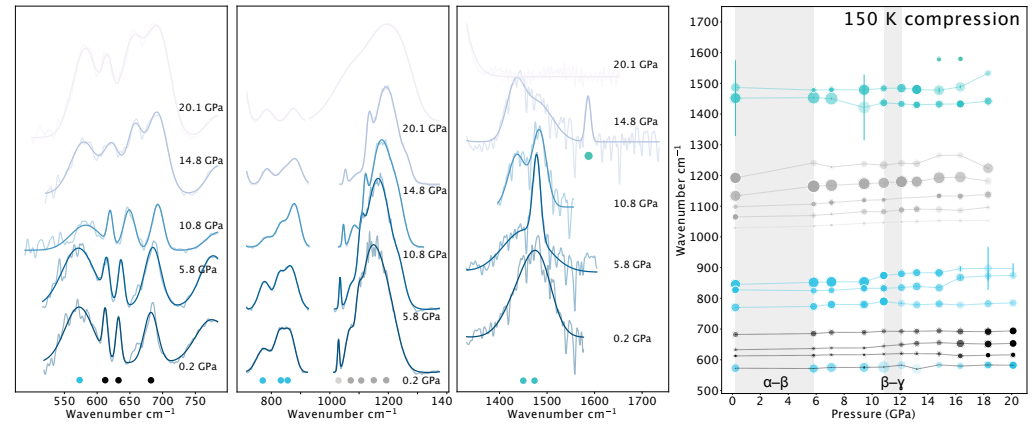

Figure 4.10: Select spectra from the 550-1700 cm^{-1} region for the 150 K high pressure dataset and the fitted peak positions for all data. Symbol sizes represent the full-width half maximum of each peak. Symbol opacity represents the peak's height, relative to itself.

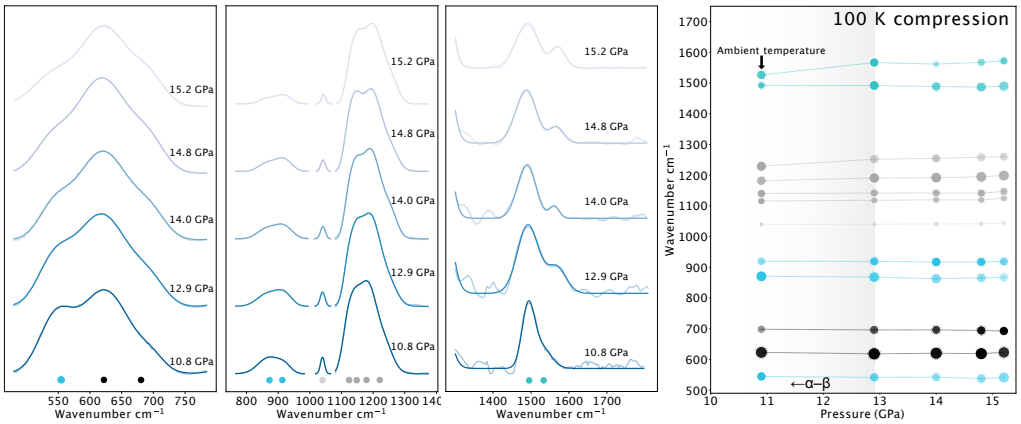

Figure 4.11: Select spectra from the 550-1700 cm^{-1} region for the 100 K high pressure dataset and the fitted peak positions for all data. Symbol sizes represent the full-width half maximum of each peak. Symbol opacity represents the peak's height, relative to itself.

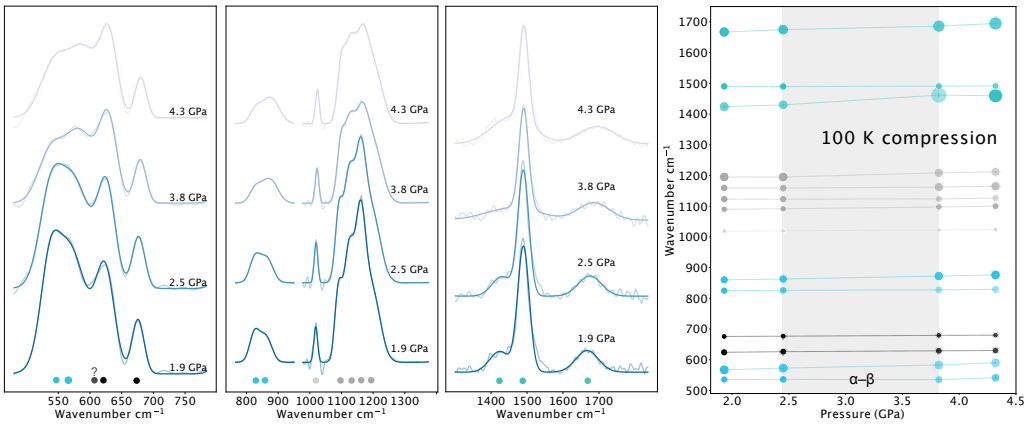

Figure 4.12: Select spectra from the 550-1700 cm^{-1} region for the 100 K high pressure dataset and the fitted peak positions for all data. Symbol sizes represent the full-width half maximum of each peak. Symbol opacity represents the peak's height, relative to itself.

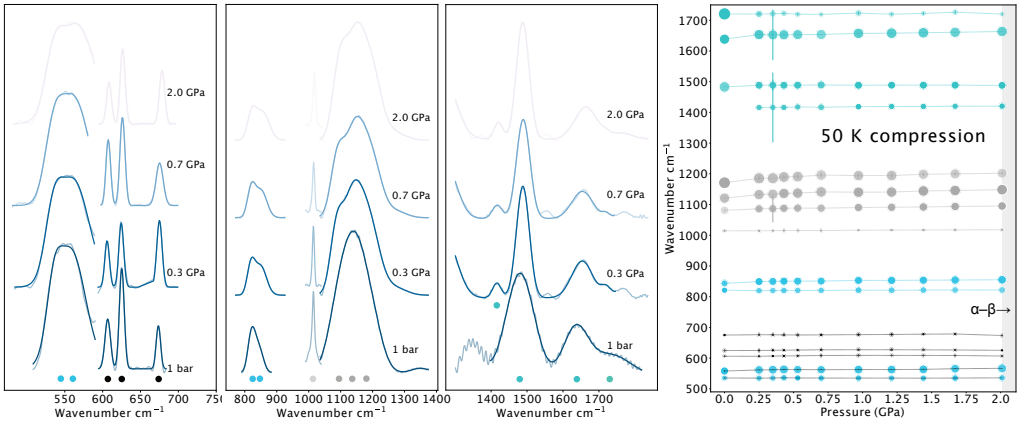

Figure 4.13: Select spectra from the 550-1700 cm^{-1} region for the 50 K high pressure dataset and the fitted peak positions for all data. Symbol sizes represent the full-width half maximum of each peak. Symbol opacity represents the peak's height, relative to itself.

Chapter 5

CONCLUSION

In this thesis, I have utilized a suite of complementary techniques to experimentally measure the structural, elastic, electronic, and vibrational properties of the hydrous iron endmember sulfate szomolnokite. Through X-ray diffraction, nuclear resonant inelastic X-ray scattering (NRIXS), synchrotron Mössbauer spectroscopy (SMS), and synchrotron Fourier transform infrared spectroscopy (FTIR), this multitechnique investigation has constructed a comprehensive description of szomolnokite's material properties at high pressures and low temperatures relevant to hydrous, sulfur-rich planetary environments. Our X-ray diffraction measurements described in Chapter 2 have revealed two structural phase transitions occurring between 5.0 and 6.6 GPa (monoclinic α-triclinic β) and between 12.7 and 16.8 GPa (triclinic β-monoclinic γ); the latter phase being stable up to the highest experimental pressure, 80 GPa. In order to derive the elastic parameters of each phase, we fit 3rd order Birch-Murnaghan equations of state to determine the isothermal bulk modulus K_T, K_T' and density as a function of pressure. I refit published data of kieserite ($MgSO_4 \cdot H_2O$) and blödite ($Na_2Mg(SO_4)_2 \cdot 4H_2O$) in order to compare the elastic parameters with szomolnokite and demonstrate the importance of reporting and comparing K_T and K_T' of high-pressure phases at the pressures where they are stable. Through the identification of these structural transitions, equation of state analysis, and ultimately high-pressure comparisons of the elastic parameters of relevant sulfate phases, I emphasize the necessity of measuring the properties of endmember hydrous sulfates so that their individual effects within a bulk material are understood.

In Chapter 3, I delve further into understanding the lattice vibrational response and effects on the iron electronic environments due to the structural transitions via NRIXS and SMS high pressure measurements. In interpreting our data, I take advantage of existing single crystal X-ray diffraction data that identifies the structural

distortion responsible for breaking the monoclinic α symmetry that transforms the structure into the lower symmetry triclinic β-phase. Tilting of the iron octahedra generates the creation of a second, structurally unique octahedral site that is accompanied by a bifurcation of the hydrogen bonding system, essentially creating varying hydrogen bond lengths. We find distinct features and pressure-dependent behavior in our NRIXS and SMS data that successfully identify alterations in both iron site-specific and bulk lattice properties associated with the phase transitions, including lattice softening concurrent with the α-β transition and decreased iron-coordination environment symmetry across both the β and γ phases.

Motivated by our goal to assess szomolnokite's ability to retain molecular water within its crystal structure at high pressure and low temperatures, in Chapter 4 I present the results of the synchrotron FTIR measurements which confirm the retention of water up to 23 GPa and to temperatures as low as 20 K. Furthermore, the spectral behavior indicates that both structural phases transitions are reversible, a phenomenon not yet studied in existing high-pressure hydrous sulfate work. Strongly supported by quantum-mechanics molecular dynamics simulations performed by William Palfey, I explain the experimentally observed H_2O-related features that have been insufficiently identified in the literature by the existence of two, vibrationally unique water sites in szomolnokite's crystal structure that generate two sets of H_2O stretching modes and two bending modes. Informed by the structural knowledge detailing the hydrogen-bond related changes occurring during the α-β transition, in this thesis I develop a spectral diagnostic for observing the α-β and β-γ transformations at ambient and low temperatures that primarily relies upon the identified H_2O stretching, bending, and librational modes. I determine that both the α-β and β-γ transitions likely possess a positive Clapeyron slope, thus occurring at lower pressures at lower temperatures. By utilizing volume-pressure-temperature dependence information from X-ray diffraction measurements, future work will perform a mode Grüneisen parameter analysis using the center frequencies derived from the high pressure and low temperature FTIR datasets. In combination with the measured phonon density of states and obtainment of the predicted phonon density of states from the calculated VDOS, the thermoelastic parameters from both experimental and computational results will be assessed.

By performing this multi-dataset cross-analysis and enabling these complementary techniques to inform one another we construct a more robust, mutually supportive set of results that deepen our understanding of szomolnokite's behavior under planetary

interior conditions. As an iron-endmember monohydrated sulfate, szomolnokite serves as a prime anchor point for the characterization of the complex chemical systems in which we find hydrous sulfates. As discussed in the introduction, hydrous sulfates often co-exist, host multiple cations, and host multiple cations of different valence states. The effect of ferric iron on the high-pressure elastic properties of mixed-valence iron-bearing hydrated sulfates like römerite ($Fe^{2+}Fe^{3+}_2(SO_4)_4 \cdot 14H_2O$), is an unexplored avenue of research. For icy satellite environments like Europa in which radiolytic chemistry results in coexisting sulfide and sulfate phases, mixed valence minerals may form and as discussed in Chapter 1, be cycled into the interior of the icy crust and possibly greater depths. The stability of hydrous, mixed valence minerals under high pressures and low temperatures and the relative effects ferrous and ferric iron have on the properties of these phases is an open question. As described in this thesis, in combination with X-ray diffraction, both SMS and NRIXS provide the experimental solution for revealing this information.

Iron-bearing sulfates possess the unique ability to be probed via nuclear resonance spectroscopy and when combined with X-ray diffraction allow for the determination of seismic wave velocities at high pressure. With growing interest and successful spacecraft missions to Saturn and Jupiter's icy moons underway, proposed missions like NASA's Europa Lander have spurred the development of seismometers in anticipation of future lander missions (Pappalardo et al., 2013; Burke et al., 2020; Marusiak et al., 2021). Thus, measuring the high-pressure seismic wave velocities and elastic properties of candidate sulfur-bearing materials and sulfur-ice mixtures will be important for interpreting lander observations in the coming decades.

In addition to seismic observations, future missions to the icy satellites will aid in better constraining the temperature profiles of their enigmatic interiors. Whichever candidate phase is experimentally probed, it will be important for future investigations to choose experimental pressure-temperature pathways that best represent the conditions of the ice-rich crust, internal ice-rich layer(s), and rocky/ice mantle. The work presented in this thesis has extended the stability of szomolnokite to temperatures as low as 50 K at 2 GPa and 100 K at 15 GPa, and pressures as high as 80 GPa at 300 K. At ambient pressure, high temperatures (>300 K) have driven the dehydration of polyhydrated ferrous sulfates, but have demonstrated the stability of monohydrates (i.e., szomolnokite) to >500 K (Brown, Bish, and Bishop, 2008). Existing work discussed in Chapter 1 has also supported the preferred stability of lower-hydration sulfates at pressures <5 GPa and temperatures up to 500 K even

in the presence of water ice (e.g., Nakamura and Ohtani, 2011). Considering the potential cycling pathways between icy satellite surfaces and their deep interiors, the combined effects of a particular temperature-depth profile, the presence of other phases, and abundance of water originating from the surrounding ice-rich environment (or proximal ocean) must be considered for future work.

Whether as primary components of sulfur- and ice-rich planetary bodies, or as minor phases in localized environments on planets like Earth and Mars, hydrated sulfates like szomolnokite have significant discovery potential for improving our understanding of this diverse array of natural systems and further experimental measurements are required to fully elucidate their material properties under extreme conditions.

Bibliography

Adler, H. H. and P. F. Kerr (Feb. 1965). "Variations in infrared spectra, molecular symmetry and site symmetry of sulfate minerals." In: *American Mineralogist* 50.1, pp. 132–147. ISSN: 0003-004X.

Ahrens, C., A. Solomonidou, K. Stephan, K. Kalousova, N. Ligier, T. McCord, and C. Hibbiitts (Jan. 1, 2022). *Physical Chemistry and Thermal Evolution of Ices at Ganymede*. Contribution to a larger work. https://ntrs.nasa.gov/citations/20210014758.

Alboom, A. V., V. G. De Resende, E. De Grave, and J. A. M. Gómez (Apr. 2009). "Hyperfine interactions in szomolnokite ($FeSO_4 \cdot H_2O$)." In: *Journal of Molecular Structure* 924-926, pp. 448–456. ISSN: 00222860. DOI: 10.1016/j.molstruc.2008.10.049.

Anderson, J. D., G. Schubert, R. A. Jacobson, E. L. Lau, W. B. Moore, and W. L. Sjogren (Sept. 25, 1998). "Europa's differentiated internal structure: Inferences from four Galileo encounters." In: *Science* 281.5385, pp. 2019–2022. ISSN: 0036-8075, 1095-9203. DOI: 10.1126/science.281.5385.2019.

Barsukov, V. L., V. P. Volkov, and I. L. Khodakovsky (1982). "The crust of Venus: Theoretical models of chemical and mineral composition." In: *Journal of Geophysical Research* 87 (S01), A3. ISSN: 0148-0227. DOI: 10.1029/JB087iS01p000A3.

Bataleva, Y., Y. Palyanov, and Y. Borzdov (Aug. 29, 2018). "Sulfide Formation as a Result of Sulfate Subduction into Silicate Mantle (Experimental Modeling under High P,T-Parameters)." In: *Minerals* 8.9, p. 373. ISSN: 2075-163X. DOI: 10.3390/min8090373.

Becker, T. M., S. K. Trumbo, P. M. Molyneux, K. D. Retherford, A. R. Hendrix, L. Roth, U. Raut, J. Alday, and M. A. McGrath (June 1, 2022). "Mid-ultraviolet Hubble Observations of Europa and the Global Surface Distribution of SO_2." In: *The Planetary Science Journal* 3.6, p. 129. ISSN: 2632-3338. DOI: 10.3847/PSJ/ac69eb.

Bénard, A., K. Klimm, A. B. Woodland, R. J. Arculus, M. Wilke, R. E. Botcharnikov, N. Shimizu, O. Nebel, C. Rivard, and D. A. Ionov (Dec. 2018). "Oxidising agents in sub-arc mantle melts link slab devolatilisation and arc magmas." In: *Nature Communications* 9.1, p. 3500. ISSN: 2041-1723. DOI: 10.1038/s41467-018-05804-2.

Berne, A., M. Simons, J. T. Keane, and R. S. Park (Dec. 16, 2022). *Inferring the Mean Effective Elastic Thickness of the Outer Ice Shell of Enceladus from Diurnal Crustal Deformation*. preprint. Preprints. DOI: 10.22541/essoar.167117599.96425607/v1.

Bishop, J. L., M. Parente, and C. M. Weitz (Nov. 19, 2009). "Mineralogy of Juventae Chasma: Sulfates in the light-toned mounds, mafic minerals in the bedrock, and hydrated silica and hydroxylated ferric sulfate on the plateau." In: *Journal of Geophysical Research* 114, E00D09. ISSN: 0148-0227. DOI: 10.1029/2009JE003352.

Brand, H. E. A., A. D. Fortes, I. G. Wood, and L. Vočadlo (May 1, 2010). "Equation of state and pressure-induced structural changes in mirabilite ($Na_2SO_4{\cdot}10H_2O$) determined from ab initio density functional theory calculations." In: *Physics and Chemistry of Minerals* 37.5, pp. 265–282. ISSN: 1432-2021. DOI: 10.1007/s00269-009-0331-1.

Brown, A., D. Bish, and J. Bishop (2008). "Dehydration of ferrous sulfates monitored by XRD-implications for CHEMIN". In: *39th Annual Lunar and Planetary Science Conference*. Issue: 1391, p. 1008.

Brown, I. D. and R. D. Shannon (May 1, 1973). "Empirical bond-strength–bond-length curves for oxides." In: *Acta Crystallographica Section A* 29.3, pp. 266–282. ISSN: 0567-7394. DOI: 10.1107/S0567739473000689.

Bu, C., G. Rodriguez Lopez, C. A. Dukes, O. Ruesch, L. A. McFadden, and J.-Y. Li (Sept. 2018). "Search for sulfates on the surface of Ceres." In: *Meteoritics & Planetary Science* 53.9, pp. 1946–1960. ISSN: 1086-9379, 1945-5100. DOI: 10.1111/maps.13024.

Buchen, J., W. Sturhahn, T. Ishii, and J. M. Jackson (Aug. 17, 2021). "Vibrational anisotropy of δ-(Al,Fe)OOH single crystals as probed by nuclear resonant inelastic X-ray scattering." In: *European Journal of Mineralogy* 33.4, pp. 485–502. ISSN: 1617-4011. DOI: 10.5194/ejm-33-485-2021.

Buffo, J. J., B. E. Schmidt, C. Huber, and C. C. Walker (Oct. 2020). "Entrainment and Dynamics of Ocean-Derived Impurities Within Europa's Ice Shell." In: *Journal of Geophysical Research: Planets* 125.10. ISSN: 2169-9097, 2169-9100. DOI: 10.1029/2020JE006394.

Burke, K., D. DellaGiustina, S. Bailey, B. Avenson, S. Otterbacher, and V. Bray (2020). "The Seismometer to Investigate Ice and Ocean Structure (SIIOS)". In: *AGU Fall Meeting Abstracts*. Vol. 2020, P044–0018.

Carlson, R. W., W. M. Calvin, J. B. Dalton, G. B. Hansen, R. L. Hudson, R. E. Johnson, T. B. McCord, and M. H. Moore (Jan. 1, 2009). *Europa's Surface Composition*. Pages: 283 Publication Title: Europa ADS Bibcode: 2009euro.book..283C.

Carr, M. H., M. J. S. Belton, C. R. Chapman, M. E. Davies, P. Geissler, R. Greenberg, A. S. McEwen, B. R. Tufts, R. Greeley, R. Sullivan, J. W. Head, R. T. Pappalardo, K. P. Klaasen, T. V. Johnson, J. Kaufman, D. Senske, J. Moore, G.

Neukum, G. Schubert, J. A. Burns, P. Thomas, and J. Veverka (Jan. 1998). "Evidence for a subsurface ocean on Europa." In: *Nature* 391.6665, pp. 363–365. ISSN: 0028-0836, 1476-4687. DOI: 10.1038/34857.

Cartwright, R. J., T. A. Nordheim, D. P. Cruikshank, K. P. Hand, J. E. Roser, W. M. Grundy, C. B. Beddingfield, and J. P. Emery (Oct. 20, 2020). "Evidence for Sulfur-bearing Species on Callisto's Leading Hemisphere: Sourced from Jupiter's Irregular Satellites or Io?" In: *The Astrophysical Journal* 902.2, p. L38. ISSN: 2041-8213. DOI: 10.3847/2041-8213/abbdae.

Cerubini, R., A. Pommerol, Z. Yoldi, and N. Thomas (Feb. 2022). "Near-infrared reflectance spectroscopy of sublimating salty ice analogues. Implications for icy moons." In: *Planetary and Space Science* 211, p. 105391. ISSN: 00320633. DOI: 10.1016/j.pss.2021.105391.

Chio, C. H., S. K. Sharma, and D. W. Muenow (Jan. 2007). "The hydrates and deuterates of ferrous sulfate ($FeSO_4$): a Raman spectroscopic study." In: *Journal of Raman Spectroscopy* 38.1, pp. 87–99. ISSN: 03770486, 10974555. DOI: 10.1002/jrs.1623.

Chou, I.-M., R. R. Seal, and A. Wang (Jan. 2013). "The stability of sulfate and hydrated sulfate minerals near ambient conditions and their significance in environmental and planetary sciences." In: *Journal of Asian Earth Sciences* 62, pp. 734–758. ISSN: 13679120. DOI: 10.1016/j.jseaes.2012.11.027.

Chowdhury, P. and R. Dasgupta (Sept. 2019). "Effect of sulfate on the basaltic liquidus and Sulfur Concentration at Anhydrite Saturation (SCAS) of hydrous basalts – Implications for sulfur cycle in subduction zones." In: *Chemical Geology* 522, pp. 162–174. ISSN: 00092541. DOI: 10.1016/j.chemgeo.2019.05.020.

Cloutis, E., F. Hawthorne, S. Mertzman, K. Krenn, M. Craig, D. Marcino, M. Methot, J. Strong, J. Mustard, and D. Blaney (Sept. 2006). "Detection and discrimination of sulfate minerals using reflectance spectroscopy." In: *Icarus* 184.1, pp. 121–157. ISSN: 00191035. DOI: 10.1016/j.icarus.2006.04.003.

Comodi, P., S. Nazzareni, T. Balic-Zunic, A. Zucchini, and M. Hanfland (Feb. 1, 2014). "The high-pressure behavior of blödite: A synchrotron single-crystal X-ray diffraction study." In: *American Mineralogist* 99.2, pp. 511–518. ISSN: 0003-004X. DOI: 10.2138/am.2014.4640.

Dalton, J. B. and K. M. Pitman (Sept. 2012). "Low temperature optical constants of some hydrated sulfates relevant to planetary surfaces." In: *Journal of Geophysical Research: Planets* 117 (E9). ISSN: 01480227. DOI: 10.1029/2011JE004036.

Dalton, J. B., J. H. Shirley, and L. W. Kamp (Mar. 2012). "Europa's icy bright plains and dark linea: Exogenic and endogenic contributions to composition and surface properties." In: *Journal of Geophysical Research: Planets* 117 (E3). ISSN: 01480227. DOI: 10.1029/2011JE003909.

Datchi, F., A. Dewaele, P. Loubeyre, R. Letoullec, Y. Le Godec, and B. Canny (Dec. 2007). "Optical pressure sensors for high-pressure–high-temperature studies in a diamond anvil cell." In: *High Pressure Research* 27.4, pp. 447–463. ISSN: 0895-7959, 1477-2299. DOI: 10.1080/08957950701659593.

Dauphas, N., M. Roskosz, E. Alp, D. Golden, C. Sio, F. Tissot, M. Hu, J. Zhao, L. Gao, and R. Morris (Oct. 2012). "A general moment NRIXS approach to the determination of equilibrium Fe isotopic fractionation factors: Application to goethite and jarosite." In: *Geochimica et Cosmochimica Acta* 94, pp. 254–275. ISSN: 00167037. DOI: 10.1016/j.gca.2012.06.013.

Dauphas, N., M. Roskosz, E. Alp, D. Neuville, M. Hu, C. Sio, F. Tissot, J. Zhao, L. Tissandier, E. Médard, and C. Cordier (July 2014). "Magma redox and structural controls on iron isotope variations in Earth's mantle and crust." In: *Earth and Planetary Science Letters* 398, pp. 127–140. ISSN: 0012821X. DOI: 10.1016/j.epsl.2014.04.033.

Dewaele, A., M. Torrent, P. Loubeyre, and M. Mezouar (Sept. 3, 2008). "Compression curves of transition metals in the Mbar range: Experiments and projector augmented-wave calculations." In: *Physical Review B* 78.10, p. 104102. ISSN: 1098-0121, 1550-235X. DOI: 10.1103/PhysRevB.78.104102.

Dobrosavljevic, V. V., D. Zhang, W. Sturhahn, J. Zhao, T. S. Toellner, S. Chariton, V. B. Prakapenka, O. S. Pardo, and J. M. Jackson (Apr. 2022). "Melting and phase relations of Fe-Ni-Si determined by a multi-technique approach." In: *Earth and Planetary Science Letters* 584, p. 117358. ISSN: 0012821X. DOI: 10.1016/j.epsl.2021.117358.

Dorogokupets, P. I. and A. R. Oganov (Oct. 2006). "Equations of state of Al, Au, Cu, Pt, Ta, and W and revised ruby pressure scale." In: *Doklady Earth Sciences* 410.1, pp. 1091–1095. ISSN: 1028-334X, 1531-8354. DOI: 10.1134/S1028334X06070208.

Dyar, M. D., E. Breves, E. Jawin, G. Marchand, M. Nelms, V. O'Connor, S. Peel, Y. Rothstein, E. C. Sklute, M. D. Lane, J. L. Bishop, and S. A. Mertzman (Nov. 1, 2013). "Mössbauer parameters of iron in sulfate minerals." In: *American Mineralogist* 98.11, pp. 1943–1965. ISSN: 0003-004X. DOI: 10.2138/am.2013.4604.

Ende, M., T. Kirkkala, M. Loitzenbauer, D. Talla, M. Wildner, and R. Miletich (May 4, 2020). "High-Pressure Behavior of Nickel Sulfate Monohydrate: Isothermal Compressibility, Structural Polymorphism, and Transition Pathway." In: *Inorganic Chemistry* 59.9, pp. 6255–6266. ISSN: 0020-1669, 1520-510X. DOI: 10.1021/acs.inorgchem.0c00370.

Fei, Y., D. Virgo, B. O. Mysen, Y. Wang, and H. K. Mao (1994). "Temperature-dependent electron delocalization in (Mg,Fe)SiO_3 perovskite." In: *American Mineralogist* 79, pp. 826–937.

Finkelstein, G. J., J. M. Jackson, W. Sturhahn, D. Zhang, E. E. Alp, and T. S. Toellner (Aug. 2017). "Single-crystal equations of state of magnesiowüstite at high

pressures." In: *American Mineralogist* 102.8, pp. 1709–1717. ISSN: 0003-004X. DOI: 10.2138/am-2017-5966.

Fortes, A. D., H. E. A. Brand, L. Vočadlo, A. Lindsay-Scott, F. Fernandez-Alonso, and I. G. Wood (Apr. 1, 2013). "$P - V - T$ equation of state of synthetic mirabilite ($Na_2SO_4 \cdot 10D_2O$) determined by powder neutron diffraction." In: *Journal of Applied Crystallography* 46.2, pp. 448–460. ISSN: 0021-8898. DOI: 10.1107/S0021889813001362.

Fortes, A. D., I. G. Wood, L. Vočadlo, H. E. A. Brand, and K. S. Knight (Aug. 1, 2007). "Crystal structures and thermal expansion of α-$MgSO_4$ and β-$MgSO_4$ from 4.2 to 300 K by neutron powder diffraction." In: *Journal of Applied Crystallography* 40.4. Publisher: International Union of Crystallography (IUCr), pp. 761–770. ISSN: 1600-5767. DOI: 10.1107/S0021889807029937.

Fortes, A. D., F. Fernandez-Alonso, M. Tucker, and I. G. Wood (Feb. 1, 2017). "Isothermal equation of state and high-pressure phase transitions of synthetic meridianiite ($MgSO_4 \cdot 11D_2O$) determined by neutron powder diffraction and quasielastic neutron spectroscopy." In: *Acta Crystallographica Section B Structural Science, Crystal Engineering and Materials* 73.1, pp. 33–46. ISSN: 2052-5206. DOI: 10.1107/S2052520616018254.

Fortes, A. D., I. G. Wood, M. Alfredsson, L. Vočadlo, and K. S. Knight (July 24, 2006). "The thermoelastic properties of MgSO47D2O (epsomite) from powder neutron diffraction and ab initio calculation." In: *European Journal of Mineralogy* 18.4, pp. 449–462. ISSN: 0935-1221. DOI: 10.1127/0935-1221/2006/0018-0449.

Franz, H. B., P. L. King, and F. Gaillard (2019). "Sulfur on Mars from the Atmosphere to the Core". In: *Volatiles in the Martian Crust*. Elsevier, pp. 119–183. ISBN: 978-0-12-804191-8. DOI: 10.1016/B978-0-12-804191-8.00006-4.

Fujii, T., H. Ohfuji, and T. Inoue (May 2016). "Phase relation of $CaSO_4$ at high pressure and temperature up to 90 GPa and 2300 K." In: *Physics and Chemistry of Minerals* 43.5, pp. 353–361. ISSN: 0342-1791, 1432-2021. DOI: 10.1007/s00269-016-0799-4.

Gaillard, F. and B. Scaillet (Mar. 2009). "The sulfur content of volcanic gases on Mars." In: *Earth and Planetary Science Letters* 279.1, pp. 34–43. ISSN: 0012821X. DOI: 10.1016/j.epsl.2008.12.028.

Gammon, P. H., H. Kiefte, M. J. Clouter, and W. W. Denner (1983). "Elastic Constants of Artificial and Natural Ice Samples by Brillouin Spectroscopy." In: *Journal of Glaciology* 29.103, pp. 433–460. ISSN: 0022-1430, 1727-5652. DOI: 10.3189/S0022143000030355.

Giester, G., C. L. Lengauer, and G. J. Redhammer (Dec. 1, 1994). "Characterization of the $FeSO_4 \cdot H_2O$-$CuSO_4 \cdot H_2O$ solid-solution series, and the nature of poitevinite, $(Cu,Fe)SO_4 \cdot H_2O$." In: *The Canadian Mineralogist* 32.4, pp. 873–884. ISSN: 0008-4476.

Gomez Casajus, L., M. Zannoni, D. Modenini, P. Tortora, F. Nimmo, T. Van Hoolst, D. Buccino, and K. Oudrhiri (Apr. 2021). "Updated Europa gravity field and interior structure from a reanalysis of Galileo tracking data." In: *Icarus* 358, p. 114187. ISSN: 00191035. DOI: 10.1016/j.icarus.2020.114187.

Grimme, S., J. Antony, S. Ehrlich, and H. Krieg (2010). "A consistent and accurate ab initio parametrization of density functional dispersion correction (DFT-D) for the 94 elements H-Pu." In: *The Journal of chemical physics* 132.15. Publisher: American Institute of Physics, p. 154104.

Grimme, S. and J.-P. Djukic (2011). "Cation-cation "attraction": When London dispersion attraction wins over Coulomb repulsion." In: *Inorganic Chemistry* 50.6. Publisher: ACS Publications, pp. 2619–2628.

Grodzicki, A. and P. Piszczek (1998). "A new interpretation of abnormal shift of water molecules' bending vibration frequencies in kieserite family monohydrates." In: *Journal of Molecular Structure* 443, pp. 141–147.

Gromnitskaya, E., O. Yagafarov, A. Lyapin, V. Brazhkin, I. Wood, M. Tucker, and A. Fortes (Mar. 1, 2013). "The high-pressure phase diagram of synthetic epsomite ($MgSO_4{\cdot}7H_2O$ and $MgSO_4{\cdot}7D_2O$) from ultrasonic and neutron powder diffraction measurements." In: *Physics and Chemistry of Minerals* 40. DOI: 10.1007/s00269-013-0567-7.

Gu, J. T., S. Fu, J. E. Gardner, S. Yamashita, T. Okuchi, and J.-F. Lin (July 1, 2021). "Nonlinear effects of hydration on high-pressure sound velocities of rhyolitic glasses." In: *American Mineralogist* 106.7, pp. 1143–1152. ISSN: 0003-004X, 1945-3027. DOI: 10.2138/am-2021-7597.

Hao, T.-w., P.-y. Xiang, H. R. Mackey, K. Chi, H. Lu, H.-k. Chui, M. C. Van Loosdrecht, and G.-H. Chen (Nov. 2014). "A review of biological sulfate conversions in wastewater treatment." In: *Water Research* 65, pp. 1–21. ISSN: 00431354. DOI: 10.1016/j.watres.2014.06.043.

Hemingway, D. J. and T. Mittal (Nov. 2019). "Enceladus's ice shell structure as a window on internal heat production." In: *Icarus* 332, pp. 111–131. ISSN: 00191035. DOI: 10.1016/j.icarus.2019.03.011.

Hibbitts, C., K. Stockstill-Cahill, B. Wing, and C. Paranicas (July 2019). "Color centers in salts - Evidence for the presence of sulfates on Europa." In: *Icarus* 326, pp. 37–47. ISSN: 00191035. DOI: 10.1016/j.icarus.2019.02.022.

Howell, S. M. and R. T. Pappalardo (May 28, 2018). "Band Formation and Ocean-Surface Interaction on Europa and Ganymede." In: *Geophysical Research Letters* 45.10, pp. 4701–4709. ISSN: 0094-8276, 1944-8007. DOI: 10.1029/2018GL077594.

Hussmann, H., C. Sotin, and J. Lunine (2015). "Interiors and Evolution of Icy Satellites". In: *Treatise on Geophysics*. Elsevier, pp. 605–635. ISBN: 978-0-444-53803-1. DOI: 10.1016/B978-0-444-53802-4.00178-0.

Ismailova, L., E. Bykova, M. Bykov, V. Cerantola, C. McCammon, T. Boffa Ballaran, A. Bobrov, R. Sinmyo, N. Dubrovinskaia, K. Glazyrin, H.-P. Liermann, I. Kupenko, M. Hanfland, C. Prescher, V. Prakapenka, V. Svitlyk, and L. Dubrovinsky (July 2016). "Stability of Fe,Al-bearing bridgmanite in the lower mantle and synthesis of pure Fe-bridgmanite." In: *Science Advances* 2.7, e1600427. ISSN: 2375-2548. DOI: 10.1126/sciadv.1600427.

Jackson, J. M., E. A. Hamecher, and W. Sturhahn (June 29, 2009). "Nuclear resonant X-ray spectroscopy of (Mg,Fe)SiO3 orthoenstatites." In: *European Journal of Mineralogy* 21.3, pp. 551–560. ISSN: 0935-1221. DOI: 10.1127/0935-1221/2009/0021-1932.

Jackson, J. M., W. Sturhahn, G. Shen, J. Zhao, M. Y. Hu, D. Errandonea, J. D. Bass, and Y. Fei (Jan. 2005). "A synchrotron Mössbauer spectroscopy study of (Mg,Fe)SiO_3 perovskite up to 120 GPa." In: *American Mineralogist* 90.1, pp. 199–205. ISSN: 0003-004X. DOI: 10.2138/am.2005.1633.

Kargel, J. S. (Dec. 1991). "Brine volcanism and the interior structures of asteroids and icy satellites." In: *Icarus* 94.2, pp. 368–390. ISSN: 00191035. DOI: 10.1016/0019-1035(91)90235-L.

King, O., L. N. Fletcher, and N. Ligier (Mar. 1, 2022). "Compositional Mapping of Europa Using MCMC Modeling of Near-IR VLT/SPHERE and Galileo/NIMS Observations." In: *The Planetary Science Journal* 3.3, p. 72. ISSN: 2632-3338. DOI: 10.3847/PSJ/ac596d.

King, P. L. and S. M. McLennan (Apr. 1, 2010). "Sulfur on Mars." In: *Elements* 6.2, pp. 107–112. ISSN: 1811-5209, 1811-5217. DOI: 10.2113/gselements.6.2.107.

Klein, R. A., J. P. S. Walsh, S. M. Clarke, Y. Guo, W. Bi, G. Fabbris, Y. Meng, D. Haskel, E. E. Alp, R. P. Van Duyne, S. D. Jacobsen, and D. E. Freedman (Sept. 26, 2018). "Impact of Pressure on Magnetic Order in Jarosite." In: *Journal of the American Chemical Society* 140.38, pp. 12001–12009. ISSN: 0002-7863, 1520-5126. DOI: 10.1021/jacs.8b05601.

Knittle, E., W. Phillips, and Q. Williams (Oct. 1, 2001). "An infrared and Raman spectroscopic study of gypsum at high pressures." In: *Physics and Chemistry of Minerals* 28.9, pp. 630–640. ISSN: 1432-2021. DOI: 10.1007/s002690100187.

Lane, M. D. (Jan. 1, 2007). "Mid-infrared emission spectroscopy of sulfate and sulfate-bearing minerals." In: *American Mineralogist* 92.1, pp. 1–18. ISSN: 0003-004X. DOI: 10.2138/am.2007.2170.

Lane, M. D., J. L. Bishop, M. D. Dyar, T. Hiroi, S. A. Mertzman, D. L. Bish, P. L. King, and A. D. Rogers (Jan. 1, 2015). "Mid-infrared emission spectroscopy and visible/near-infrared reflectance spectroscopy of Fe-sulfate minerals." In: *American Mineralogist* 100.1, pp. 66–82. ISSN: 0003-004X. DOI: 10.2138/am-2015-4762.

Lane, M. D., M. D. Dyar, and J. L. Bishop (2004). "Spectroscopic evidence for hydrous iron sulfate in the Martian soil." In: *Geophysical Research Letters* 31.19, p. L19702. ISSN: 0094-8276. DOI: 10.1029/2004GL021231.

Li, J.-L., E. M. Schwarzenbach, T. John, J. J. Ague, S. Tassara, J. Gao, and B. A. Konecke (Mar. 2021). "Subduction zone sulfur mobilization and redistribution by intraslab fluid–rock interaction." In: *Geochimica et Cosmochimica Acta* 297, pp. 40–64. ISSN: 00167037. DOI: 10.1016/j.gca.2021.01.011.

Libowitzky, E. (1999). "Correlation of O-H stretching frequencies and O-H…O hydrogen bond lengths in minerals." In: *Monatshefte für Chemie / Chemical Monthly* 130, pp. 1047–1059.

Lichtenberg, K. A., R. E. Arvidson, R. V. Morris, S. L. Murchie, J. L. Bishop, D. Fernandez Remolar, T. D. Glotch, E. Noe Dobrea, J. F. Mustard, J. Andrews-Hanna, and L. H. Roach (June 10, 2010). "Stratigraphy of hydrated sulfates in the sedimentary deposits of Aram Chaos, Mars." In: *Journal of Geophysical Research* 115, E00D17. ISSN: 0148-0227. DOI: 10.1029/2009JE003353.

Ligier, N., C. Paranicas, J. Carter, F. Poulet, W. Calvin, T. Nordheim, C. Snodgrass, and L. Ferellec (Nov. 2019). "Surface composition and properties of Ganymede: Updates from ground-based observations with the near-infrared imaging spectrometer SINFONI/VLT/ESO." In: *Icarus* 333, pp. 496–515. ISSN: 00191035. DOI: 10.1016/j.icarus.2019.06.013.

Liu, Y., M. Santosh, T. Yuan, H. Li, and T. Li (Apr. 2016). "Reduction of buried oxidized oceanic crust during subduction." In: *Gondwana Research* 32, pp. 11–23. ISSN: 1342937X. DOI: 10.1016/j.gr.2015.02.014.

Machado de Oliveira, C., T. Gesser Müller, L. Patricio Ferreira, M. A. Prado Cechinel, M. Peterson, and F. Raupp-Pereira (Feb. 2019). "Valorization of iron pyrite from coal mining in southern Brazil." In: *Journal of Environmental Chemical Engineering* 7.1, p. 102931. ISSN: 22133437. DOI: 10.1016/j.jece.2019.102931.

Majzlan, J., C. N. Alpers, C. B. Koch, R. B. McCleskey, S. C. Myneni, and J. M. Neil (May 2011). "Vibrational, X-ray absorption, and Mössbauer spectra of sulfate minerals from the weathered massive sulfide deposit at Iron Mountain, California." In: *Chemical Geology* 284.3, pp. 296–305. ISSN: 00092541. DOI: 10.1016/j.chemgeo.2011.03.008.

Marquardt, H., S. Speziale, H. J. Reichmann, D. J. Frost, and F. R. Schilling (Oct. 15, 2009). "Single-crystal elasticity of $(Mg_{0.9}Fe_{0.1})O$ to 81 GPa." In: *Earth and Planetary Science Letters* 287.3, pp. 345–352. ISSN: 0012-821X. DOI: 10.1016/j.epsl.2009.08.017.

Marusiak, A. G., N. C. Schmerr, D. N. DellaGiustina, B. Avenson, S. H. Bailey, V. J. Bray, J. I. Brodbeck, C. G. Carr, P. H. Dahl, N. Habib, et al. (2021). "The deployment of the seismometer to investigate ice and ocean structure (SIIOS) in northwest Greenland: An analog experiment for icy ocean world seismic deploy-

ments." In: *Seismological Research Letters* 92.3. Publisher: GeoScienceWorld, pp. 2036–2049.

McCammon, C. (June 1, 1997). "Perovskite as a possible sink for ferric iron in the lower mantle." In: *Nature* 387.6634, pp. 694–696. ISSN: 1476-4687. DOI: 10.1038/42685.

McCanta, M. C., M. D. Dyar, and A. H. Treiman (Feb. 1, 2014). "Alteration of Hawaiian basalts under sulfur-rich conditions: Applications to understanding surface-atmosphere interactions on Mars and Venus." In: *American Mineralogist* 99.2, pp. 291–302. ISSN: 0003-004X. DOI: 10.2138/am.2014.4584.

McCollom, T. M., M. Robbins, B. Moskowitz, T. S. Berquó, N. Jöns, and B. M. Hynek (Apr. 2013). "Experimental study of acid-sulfate alteration of basalt and implications for sulfate deposits on Mars." In: *Journal of Geophysical Research: Planets* 118.4, pp. 577–614. ISSN: 2169-9097, 2169-9100. DOI: 10.1002/jgre.20044.

McEwen, A. S. (1986). "Exogenic and endogenic albedo and color patterns on Europa." In: *Journal of Geophysical Research* 91 (B8), p. 8077. ISSN: 0148-0227. DOI: 10.1029/JB091iB08p08077.

Meusburger, J., M. Ende, D. Talla, M. Wildner, and R. Miletich (Sept. 2019). "Transformation mechanism of the pressure-induced $C2/c$-to-$P\bar{1}$ transition in ferrous sulfate monohydrate single crystals." In: *Journal of Solid State Chemistry* 277, pp. 240–252. ISSN: 00224596. DOI: 10.1016/j.jssc.2019.06.004.

Meusburger, J., K. A. Hudson-Edwards, C. C. Tang, E. T. Connolly, R. A. Crane, and A. D. Fortes (2022). "Low-temperature crystallography and vibrational properties of rozenite, a candidate mineral component of the polyhydrated sulfate deposits on Mars." In: (in press). DOI: https://doi.org/10.2138/am-2022-8502.

Meusburger, J. M., M. Ende, P. Matzinger, D. Talla, R. Miletich, and M. Wildner (Jan. 2020). "Polymorphism of Mg-monohydrate sulfate kieserite under pressure and its occurrence on giant icy Jovian satellites." In: *Icarus* 336, p. 113459. ISSN: 00191035. DOI: 10.1016/j.icarus.2019.113459.

Molyneux, P. M., J. D. Nichols, T. M. Becker, U. Raut, and K. D. Retherford (Sept. 2020). "Ganymede's Far-Ultraviolet Reflectance: Constraining Impurities in the Surface Ice." In: *Journal of Geophysical Research: Planets* 125.9. ISSN: 2169-9097, 2169-9100. DOI: 10.1029/2020JE006476.

Moore, W. and G. Schubert (Sept. 2000). "The Tidal Response of Europa." In: *Icarus* 147.1, pp. 317–319. ISSN: 00191035. DOI: 10.1006/icar.2000.6460.

Morrison, R. A., J. M. Jackson, W. Sturhahn, J. Zhao, and T. S. Toellner (Sept. 2019). "High pressure thermoelasticity and sound velocities of Fe-Ni-Si alloys." In: *Physics of the Earth and Planetary Interiors* 294, p. 106268. ISSN: 00319201. DOI: 10.1016/j.pepi.2019.05.011.

Murphy, C. A., J. M. Jackson, and W. Sturhahn (May 2013). "Experimental constraints on the thermodynamics and sound velocities of hcp-Fe to core pressures." In: *Journal of Geophysical Research: Solid Earth* 118.5, pp. 1999–2016. ISSN: 21699313. DOI: 10.1002/jgrb.50166.

Muth, M. J. and P. J. Wallace (Oct. 1, 2021). "Slab-derived sulfate generates oxidized basaltic magmas in the southern Cascade arc (California, USA)." In: *Geology* 49.10, pp. 1177–1181. ISSN: 0091-7613, 1943-2682. DOI: 10.1130/G48759.1.

Nachon, M., S. M. Clegg, N. Mangold, S. Schröder, L. C. Kah, G. Dromart, A. Ollila, J. R. Johnson, D. Z. Oehler, J. C. Bridges, S. Le Mouélic, O. Forni, R. Wiens, R. B. Anderson, D. L. Blaney, J. Bell, B. Clark, A. Cousin, M. D. Dyar, B. Ehlmann, C. Fabre, O. Gasnault, J. Grotzinger, J. Lasue, E. Lewin, R. Léveillé, S. McLennan, S. Maurice, P.-Y. Meslin, W. Rapin, M. Rice, S. W. Squyres, K. Stack, D. Y. Sumner, D. Vaniman, and D. Wellington (Sept. 2014). "Calcium sulfate veins characterized by ChemCam/Curiosity at Gale Crater, Mars: calcium SULFATE VEINS aT GALE CRATER." In: *Journal of Geophysical Research: Planets* 119.9, pp. 1991–2016. ISSN: 21699097. DOI: 10.1002/2013JE004588.

Nakamura, R. and E. Ohtani (Jan. 2011). "The high-pressure phase relation of the $MgSO_4$–H_2O system and its implication for the internal structure of Ganymede." In: *Icarus* 211.1, pp. 648–654. ISSN: 00191035. DOI: 10.1016/j.icarus.2010.08.029.

Nazzareni, S., P. Comodi, L. Bindi, and L. Dubrovinsky (Apr. 1, 2010). "The crystal structure of gypsum-II determined by single-crystal synchrotron X-ray diffraction data." In: *American Mineralogist* 95.4, pp. 655–658. ISSN: 0003-004X. DOI: 10.2138/am.2010.3452.

Nimmo, F. and M. Manga (2009). "Geodynamics of Europa's icy shell." In: *Europa*. Publisher: University of Arizona Press Tucson, pp. 381–404.

Pan, Y., W. Yong, and R. A. Secco (Nov. 16, 2020). "Electrical Conductivity of Aqueous Magnesium Sulfate at High Pressure and Low Temperature With Application to Ganymede's Subsurface Ocean." In: *Geophysical Research Letters* 47.21. ISSN: 0094-8276, 1944-8007. DOI: 10.1029/2020GL090192.

Pappalardo, R., S. Vance, F. Bagenal, B. Bills, D. Blaney, D. Blankenship, W. Brinckerhoff, J. Connerney, K. Hand, T. Hoehler, J. Leisner, W. Kurth, M. McGrath, M. Mellon, J. Moore, G. Patterson, L. Prockter, D. Senske, B. Schmidt, E. Shock, D. Smith, and K. Soderlund (Aug. 2013). "Science Potential from a Europa Lander." In: *Astrobiology* 13.8, pp. 740–773. ISSN: 1531-1074, 1557-8070. DOI: 10.1089/ast.2013.1003.

Pardo, O. S., V. V. Dobrosavljevic, T. Perez, W. Sturhahn, Z. Liu, G. R. Rossman, and J. M. Jackson (Mar. 1, 2023). "X-ray diffraction reveals two structural transitions in szomolnokite." In: *American Mineralogist* 108.3, pp. 476–484. ISSN: 0003-004X, 1945-3027. DOI: 10.2138/am-2022-8147.

Pardo, O. S., V. V. Dobrosavljevic, W. Sturhahn, T. S. Toellner, B. Strozewski, and J. M. Jackson (May 1, 2023). *Lattice dynamics, sound velocities, and atomic environments of szomolnokite at high pressure*. preprint. In Review. DOI: 10.21203/rs.3.rs-2861032/v1.

Perez, T., G. J. Finkelstein, O. Pardo, N. V. Solomatova, and J. M. Jackson (Feb. 8, 2020). "A Synchrotron Mössbauer Spectroscopy Study of a Hydrated Iron-Sulfate at High Pressures." In: *Minerals* 10.2, p. 146. ISSN: 2075-163X. DOI: 10.3390/min10020146.

Pistorius, W. F. T. (1960). "Lattice Constants of $FeSO_4 \cdot H_2O$ (artificial szomolnokite) and $NiSO_4 \cdot H_2O$." In: *Bulletin des Sociétés Chimiques Belges* 69.11, pp. 570–574. ISSN: 00379646. DOI: 10.1002/bscb.19600691106.

Prescher, C. and V. B. Prakapenka (July 3, 2015). "DIOPTAS: a program for reduction of two-dimensional X-ray diffraction data and data exploration." In: *High Pressure Research* 35.3, pp. 223–230. ISSN: 0895-7959, 1477-2299. DOI: 10.1080/08957959.2015.1059835.

Prockter, L. M., J. H. Shirley, J. B. Dalton, and L. Kamp (Mar. 2017). "Surface composition of pull-apart bands in Argadnel Regio, Europa: Evidence of localized cryovolcanic resurfacing during basin formation." In: *Icarus* 285, pp. 27–42. ISSN: 00191035. DOI: 10.1016/j.icarus.2016.11.024.

Ratschbacher, B. C., J. M. Jackson, T. S. Toellner, C. E. Bucholz, W. Sturhahn, and N. V. Solomatova (Jan. 3, 2023). "Fe^{3+}/Fe^{T} ratios of amphiboles determined by high spatial resolution single-crystal synchrotron Mössbauer spectroscopy." In: *American Mineralogist* 108.1, pp. 70–86. ISSN: 0003-004X, 1945-3027. DOI: 10.2138/am-2022-8115.

Roskosz, M., N. Dauphas, J. Hu, M. Y. Hu, D. R. Neuville, D. Brown, W. Bi, N. X. Nie, J. Zhao, and E. E. Alp (Mar. 2022). "Structural, redox and isotopic behaviors of iron in geological silicate glasses: A NRIXS study of Lamb-Mössbauer factors and force constants." In: *Geochimica et Cosmochimica Acta* 321, pp. 184–205. ISSN: 00167037. DOI: 10.1016/j.gca.2022.01.021.

Rubens, H. and E. F. Nichols (1897). "Heat rays of great wave length." In: *Physical Review (Series I)* 4.4. Publisher: APS, p. 314.

Rye, R. O. (Feb. 2005). "A review of the stable-isotope geochemistry of sulfate minerals in selected igneous environments and related hydrothermal systems." In: *Chemical Geology* 215.1, pp. 5–36. ISSN: 00092541. DOI: 10.1016/j.chemgeo.2004.06.034.

Sakamaki, T., Y. Kono, Y. Wang, C. Park, T. Yu, Z. Jing, and G. Shen (Apr. 2014). "Contrasting sound velocity and intermediate-range structural order between polymerized and depolymerized silicate glasses under pressure." In: *Earth and Planetary Science Letters* 391, pp. 288–295. ISSN: 0012821X. DOI: 10.1016/j.epsl.2014.02.008.

Sanchez-Valle, C. and J. D. Bass (July 2010). "Elasticity and pressure-induced structural changes in vitreous $MgSiO_3$-enstatite to lower mantle pressures." In: *Earth and Planetary Science Letters* 295.3, pp. 523–530. ISSN: 0012821X. DOI: 10.1016/j.epsl.2010.04.034.

Sanchez-Valle, C., S. V. Sinogeikin, J. R. Smyth, and J. D. Bass (Nov. 2008). "Sound velocities and elasticity of DHMS phase A to high pressure and implications for seismic velocities and anisotropy in subducted slabs." In: *Physics of the Earth and Planetary Interiors* 170.3, pp. 229–239. ISSN: 00319201. DOI: 10.1016/j.pepi.2008.07.015.

Schwarzenbach, E. M., M. J. Caddick, M. Petroff, B. C. Gill, E. H. G. Cooperdock, and J. D. Barnes (Dec. 2018). "Sulphur and carbon cycling in the subduction zone mélange." In: *Scientific Reports* 8.1, p. 15517. ISSN: 2045-2322. DOI: 10.1038/s41598-018-33610-9.

Shi, W., N. Sun, X. Li, Z. Mao, J. Liu, and V. B. Prakapenka (2021). "Single-Crystal Elasticity of High-Pressure Ice up to 98 GPa by Brillouin Scattering." In: *Geophysical Research Letters* 48.8, e2021GL092514. DOI: https://doi.org/10.1029/2021GL092514.

Singh, D., P. Singh, N. Roy, and S. Mukherjee (Jan. 2022). "Investigation of mineral assemblages in a newly identified endorheic playa near Huygens basin on Mars and their astrobiological implications." In: *Icarus* 372, p. 114757. ISSN: 00191035. DOI: 10.1016/j.icarus.2021.114757.

Siriwardane, R. V., J. A. Poston Jr, E. P. Fisher, M.-S. Shen, and A. L. Miltz (Nov. 1999). "Decomposition of the sulfates of copper, iron (II), iron (III), nickel, and zinc: XPS, SEM, DRIFTS, XRD, and TGA study." In: *Applied Surface Science* 152.3, pp. 219–236. ISSN: 01694332. DOI: 10.1016/S0169-4332(99)00319-0.

Sklute, E. C., H. B. Jensen, A. D. Rogers, and R. J. Reeder (Apr. 2015). "Morphological, structural, and spectral characteristics of amorphous iron sulfates." In: *Journal of Geophysical Research: Planets* 120.4, pp. 809–830. ISSN: 2169-9097, 2169-9100. DOI: 10.1002/2014JE004784.

Solomatova, N. V., J. M. Jackson, W. Sturhahn, G. R. Rossman, and M. Roskosz (Aug. 2017). "Electronic environments of ferrous iron in rhyolitic and basaltic glasses at high pressure: Silicate Glasses at High Pressure." In: *Journal of Geophysical Research: Solid Earth* 122.8, pp. 6306–6322. ISSN: 21699313. DOI: 10.1002/2017JB014363.

Souček, O., M. Běhounková, O. Čadek, J. Hron, G. Tobie, and G. Choblet (Aug. 2019). "Tidal dissipation in Enceladus' uneven, fractured ice shell." In: *Icarus* 328, pp. 218–231. ISSN: 00191035. DOI: 10.1016/j.icarus.2019.02.012.

Sturhahn, W. (Feb. 11, 2004). "Nuclear resonant spectroscopy." In: *Journal of Physics: Condensed Matter* 16.5, S497–S530. ISSN: 0953-8984, 1361-648X. DOI: 10.1088/0953-8984/16/5/009.

Sturhahn, W. (2020). *MINeral physics UTIlity (MINUTI) open-source software package.* Comp. software. www.nrixs.com.

Talla, D. and M. Wildner (Dec. 1, 2019). "Investigation of the kieserite–szomolnokite solid-solution series, (Mg,Fe)$SO_4 \cdot H_2O$, with relevance to Mars: Crystal chemistry, FTIR, and Raman spectroscopy under ambient and Martian temperature conditions." In: *American Mineralogist* 104.12, pp. 1732–1749. ISSN: 0003-004X, 1945-3027. DOI: 10.2138/am-2019-6983.

Toby, B. H. (Mar. 2006). "R factors in Rietveld analysis: How good is good enough?" In: *Powder Diffraction* 21.1, pp. 67–70. ISSN: 0885-7156, 1945-7413. DOI: 10.1154/1.2179804.

Toby, B. H. and R. B. Von Dreele (Apr. 1, 2013). "GSAS-II: the genesis of a modern open-source all purpose crystallography software package." In: *Journal of Applied Crystallography* 46.2, pp. 544–549. ISSN: 0021-8898. DOI: 10.1107/S0021889813003531.

Toellner, T. S., E. E. Alp, T. Graber, R. W. Henning, S. D. Shastri, G. Shenoy, and W. Sturhahn (Mar. 1, 2011). "Synchrotron Mössbauer spectroscopy using high-speed shutters." In: *Journal of Synchrotron Radiation* 18.2, pp. 183–188. ISSN: 0909-0495. DOI: 10.1107/S090904951003863X.

Toellner, T. (2000). "Monochromatization of synchrotron radiation for nuclear resonant scattering experiments." In: *Hyperfine Interactions* 125.1, pp. 3–28. ISSN: 03043834. DOI: 10.1023/A:1012621317798.

Trumbo, S. K., M. E. Brown, and K. P. Hand (Nov. 23, 2020). "Endogenic and Exogenic Contributions to Visible-wavelength Spectra of Europa's Trailing Hemisphere." In: *The Astronomical Journal* 160.6, p. 282. ISSN: 1538-3881. DOI: 10.3847/1538-3881/abc34c.

Vance, S., M. Bouffard, M. Choukroun, and C. Sotin (June 2014). "Ganymede's internal structure including thermodynamics of magnesium sulfate oceans in contact with ice." In: *Planetary and Space Science* 96, pp. 62–70. ISSN: 00320633. DOI: 10.1016/j.pss.2014.03.011.

Vu, T. H., M. Choukroun, R. Hodyss, and P. V. Johnson (Oct. 2020). "Probing Europa's subsurface ocean composition from surface salt minerals using in-situ techniques." In: *Icarus* 349, p. 113746. ISSN: 00191035. DOI: 10.1016/j.icarus.2020.113746.

Wahr, J. M., M. T. Zuber, D. E. Smith, and J. I. Lunine (Dec. 2006). "Tides on Europa, and the thickness of Europa's icy shell: tides on Europa." In: *Journal of Geophysical Research: Planets* 111 (E12), n/a–n/a. ISSN: 01480227. DOI: 10.1029/2006JE002729.

Wang, A., L. A. Haskin, S. W. Squyres, B. L. Jolliff, L. Crumpler, R. Gellert, C. Schröder, K. Herkenhoff, J. Hurowitz, N. J. Tosca, W. H. Farrand, R. Anderson, and A. T. Knudson (Feb. 2006). "Sulfate deposition in subsurface regolith in Gu-

sev crater, Mars." In: *Journal of Geophysical Research: Planets* 111 (E2), n/a–n/a. ISSN: 01480227. DOI: 10.1029/2005JE002513.

Wang, A., B. L. Jolliff, Y. Liu, and K. Connor (Apr. 2016). "Setting constraints on the nature and origin of the two major hydrous sulfates on Mars: Monohydrated and polyhydrated sulfates." In: *Journal of Geophysical Research: Planets* 121.4, pp. 678–694. ISSN: 2169-9097, 2169-9100. DOI: 10.1002/2015JE004889.

Wei, X., L. Dong, F. Li, Q. Zhou, C. Zhang, M. Guo, Y. Wei, X. Zhang, L. Li, X. Li, and Z. Liu (Aug. 24, 2022). "Effect of Al_2O_3 on Sound Velocity of $MgSiO_3$ Glass at High Pressure." In: *Minerals* 12.9, p. 1069. ISSN: 2075-163X. DOI: 10.3390/min12091069.

Wendt, L., C. Gross, T. Kneissl, M. Sowe, J.-P. Combe, L. LeDeit, P. C. McGuire, and G. Neukum (May 2011). "Sulfates and iron oxides in Ophir Chasma, Mars, based on OMEGA and CRISM observations." In: *Icarus* 213.1, pp. 86–103. ISSN: 00191035. DOI: 10.1016/j.icarus.2011.02.013.

Wildner, M. and G. Giester (July 1991). "The crystal structures of kieserite-type compounds. I. Crystal structures of $Me(II)SO_4 \cdot H_2O$ (Me = Mn, Fe, Co, Ni, Zn)." In: *Neues Jahrbuch für Mineralogie - Journal of Mineralogy and Geochemistry* 7, pp. 296–306.

Wildner, M., M. Ende, J. M. Meusburger, R. Kunit, P. Matzinger, D. Talla, and R. Miletich (Oct. 26, 2021). "$CoSO_4 \cdot H_2O$ and its continuous transition compared to the compression properties of isostructural kieserite-type polymorphs." In: *Zeitschrift für Kristallographie - Crystalline Materials* 236.8, pp. 225–237. ISSN: 2194-4946, 2196-7105. DOI: 10.1515/zkri-2021-2038.

Wildner, M., B. A. Zakharov, N. E. Bogdanov, D. Talla, E. V. Boldyreva, and R. Miletich (Mar. 2022). "Crystallography relevant to Mars and Galilean icy moons: crystal behavior of kieserite-type monohydrate sulfates at extraterrestrial conditions down to 15 K." In: *IUCrJ* 9.2, pp. 194–203. DOI: 10.1107/S2052252521012720.

Wirth, R., F. Kaminsky, S. Matsyuk, and A. Schreiber (Aug. 2009). "Unusual micro- and nano-inclusions in diamonds from the Juina Area, Brazil." In: *Earth and Planetary Science Letters* 286.1, pp. 292–303. ISSN: 0012821X. DOI: 10.1016/j.epsl.2009.06.043.

Witzke, A., G. Arnold, and D. Stöffler (Mar. 2007). "Spectral detectability of Ca- and Mg-sulfates in Martian bright soils in the 4–5μm wavelength range." In: *Planetary and Space Science* 55.4, pp. 429–440. ISSN: 00320633. DOI: 10.1016/j.pss.2006.08.003.

Wojdyr, M. (Oct. 1, 2010). "*Fityk*: A general-purpose peak fitting program." In: *Journal of Applied Crystallography* 43.5, pp. 1126–1128. ISSN: 0021-8898. DOI: 10.1107/S0021889810030499.

Zhang, D., J. M. Jackson, W. Sturhahn, J. Zhao, E. E. Alp, and M. Y. Hu (Mar. 1, 2022). "Measurements of the Lamb-Mössbauer factor at simultaneous high-pressure-temperature conditions and estimates of the equilibrium isotopic fractionation of iron." In: *American Mineralogist* 107.3, pp. 421–431. ISSN: 0003-004X, 1945-3027. DOI: 10.2138/am-2021-7884.

Zhang, H., O. Tóth, X.-D. Liu, R. Bini, E. Gregoryanz, P. Dalladay-Simpson, S. De Panfilis, M. Santoro, F. A. Gorelli, and R. Martoňák (Apr. 21, 2020). "Pressure-induced amorphization and existence of molecular and polymeric amorphous forms in dense SO_2." In: *Proceedings of the National Academy of Sciences* 117.16, pp. 8736–8742. ISSN: 0027-8424, 1091-6490. DOI: 10.1073/pnas.1917749117.

Zhang, J. S., M. Hao, Z. Ren, and B. Chen (May 13, 2019). "The extreme acoustic anisotropy and fast sound velocities of cubic high-pressure ice polymorphs at Mbar pressure." In: *Applied Physics Letters* 114.19, p. 191903. ISSN: 0003-6951, 1077-3118. DOI: 10.1063/1.5096989.

Zolotov, M. (Aug. 28, 2019). "Chemical Weathering on Venus". In: *Oxford Research Encyclopedia of Planetary Science*. Oxford University Press. ISBN: 978-0-19-064792-6. DOI: 10.1093/acrefore/9780190647926.013.146.

SUPPLEMENTARY MATERIALS TO CHAPTER 2

Table S1. Refined lattice parameters

Pressure (GPa)	Pressure error^ (GPa)	*a* (Å)	*a error* (Å)	*b* (Å)	*b error* (Å)	c (Å)	*c error* (Å)	α* (°)	α error (°)	β (°)	β error (°)	γ* (°)	γ error (°)	Volume (Å^3)	Volume error (Å^3)
0.000[#]	0.000	7.086	0.002	7.550	0.000	7.779	0.002	90.000	0.000	118.663	0.003	90.000	0.000	365.146	0.026
0.39	0.06	7.077	0.002	7.526	0.000	7.741	0.003	90.000	0.000	118.701	0.005	90.000	0.000	361.679	0.045
0.51	0.00	7.079	0.002	7.523	0.000	7.737	0.003	90.000	0.000	118.787	0.005	90.000	0.000	361.133	0.053
1.47	0.03	7.061	0.002	7.479	0.000	7.665	0.003	90.000	0.000	118.838	0.005	90.000	0.000	354.609	0.035
2.23	0.09	7.049	0.003	7.450	0.000	7.624	0.003	90.000	0.000	118.867	0.006	90.000	0.000	350.616	0.043
3.09	0.07	7.019	0.007	7.411	0.001	7.582	0.008	90.000	0.000	118.908	0.014	90.000	0.000	345.259	0.103
4.96	0.09	7.012	0.007	7.337	0.001	7.468	0.008	90.000	0.000	118.946	0.014	90.000	0.000	336.222	0.133
6.56[a]	0.09	6.982	0.003	7.310	0.002	7.399	0.006	90.079	0.008	119.151	0.009	90.684	0.006	164.886	0.033
8.83	0.10	6.940	0.003	7.279	0.002	7.272	0.009	90.162	0.009	119.154	0.011	91.473	0.006	160.351	0.022
10.05	0.11	6.913	0.005	7.248	0.004	7.230	0.011	90.371	0.016	119.085	0.018	91.645	0.009	158.190	0.032
11.38	0.17	6.910	0.004	7.220	0.003	7.188	0.006	90.033	0.013	119.395	0.011	92.051	0.008	156.072	0.031
12.73	0.32	6.869	0.007	7.194	0.005	7.151	0.011	89.841	0.019	119.034	0.023	92.235	0.010	154.335	0.040
16.79[b]	0.34	6.746	0.005	7.051	0.001	6.910	0.006	90.000	0.000	118.226	0.011	90.000	0.000	289.620	0.034
18.33	0.00	6.705	0.006	7.032	0.001	6.861	0.007	90.000	0.000	117.858	0.013	90.000	0.000	285.995	0.038
19.53	0.07	6.673	0.009	7.029	0.001	6.824	0.009	90.000	0.000	117.630	0.018	90.000	0.000	283.590	0.059
20.48	0.11	6.663	0.006	7.019	0.001	6.805	0.007	90.000	0.000	117.571	0.013	90.000	0.000	282.123	0.035
22.52	0.09	6.631	0.004	7.009	0.001	6.768	0.004	90.000	0.000	117.302	0.008	90.000	0.000	279.521	0.024
25.22	0.02	6.561	0.007	7.001	0.001	6.660	0.008	90.000	0.000	116.805	0.015	90.000	0.000	273.056	0.049
28.23	0.04	6.518	0.005	6.984	0.001	6.606	0.005	90.000	0.000	116.522	0.010	90.000	0.000	269.055	0.032
30.73	0.10	6.479	0.003	6.959	0.001	6.563	0.004	90.000	0.000	116.402	0.008	90.000	0.000	265.053	0.026
32.49	0.08	6.451	0.004	6.954	0.001	6.526	0.004	90.000	0.000	116.221	0.008	90.000	0.000	262.635	0.030
34.16	0.18	6.434	0.008	6.959	0.001	6.476	0.009	90.000	0.000	116.298	0.018	90.000	0.000	259.942	0.055
36.74	0.06	6.412	0.007	6.954	0.001	6.454	0.008	90.000	0.000	116.123	0.016	90.000	0.000	258.377	0.052
39.83	0.16	6.380	0.007	6.942	0.001	6.419	0.007	90.000	0.000	116.122	0.015	90.000	0.000	255.291	0.052

Table S1: Table continued on next page.

Table S1. Refined lattice parameters.

Pressure (GPa)	Pressure error^ (GPa)	*a* (Å)	*a error* (Å)	*b* (Å)	*b error* (Å)	c (Å)	*c error* (Å)	α* (°)	α error (°)	β (°)	β error (°)	γ* (°)	γ error (°)	Volume (Å^3)	Volume error (Å^3)
42.51	0.14	6.309	0.004	6.919	0.001	6.387	0.004	90.000	0.000	115.568	0.009	90.000	0.000	251.486	0.034
45.08	0.17	6.274	0.005	6.901	0.001	6.351	0.005	90.000	0.000	115.437	0.011	90.000	0.000	248.332	0.034
48.36	0.36	6.252	0.004	6.885	0.001	6.326	0.005	90.000	0.000	115.498	0.010	90.000	0.000	245.790	0.034
50.14	0.32	6.231	0.005	6.878	0.001	6.314	0.005	90.000	0.000	115.553	0.010	90.000	0.000	244.147	0.036
53.54	0.34	6.197	0.005	6.853	0.001	6.275	0.005	90.000	0.000	115.446	0.011	90.000	0.000	240.607	0.037
54.73	0.12	6.171	0.005	6.844	0.001	6.254	0.005	90.000	0.000	115.449	0.010	90.000	0.000	238.486	0.033
58.35	0.19	6.153	0.005	6.838	0.001	6.241	0.005	90.000	0.000	115.494	0.011	90.000	0.000	237.048	0.036
61.94	0.15	6.122	0.005	6.821	0.001	6.202	0.005	90.000	0.000	115.272	0.011	90.000	0.000	234.211	0.035
64.62	0.15	6.124	0.004	6.803	0.001	6.200	0.005	90.000	0.000	115.365	0.010	90.000	0.000	233.400	0.033
67.41	0.06	6.086	0.004	6.802	0.001	6.168	0.005	90.000	0.000	115.278	0.010	90.000	0.000	230.869	0.036
71.10	0.01	6.065	0.006	6.777	0.001	6.136	0.006	90.000	0.000	115.128	0.012	90.000	0.000	228.344	0.043
80.40	0.17	6.005	0.004	6.751	0.001	6.081	0.004	90.000	0.000	115.085	0.009	90.000	0.000	223.263	0.037
82.85	0.00	6.000	0.005	6.733	0.001	6.076	0.005	90.000	0.000	115.134	0.011	90.000	0.000	222.241	0.043

Table S1: (Table continued from previous page) Refined lattice parameters.
Unit-cell parameters and errors determined from GSAS-II. Errors were artificially increased for equation of state fitting.
[a]Onset of the $P\bar{1}$ phase. Lattice parameters are transformed into the monoclinic setting
[b]Onset of the $P2_1$ phase.
*Fixed at 90° except for data in the transformed $P\bar{1}$ phase from 6.56-12.73 GPa.
#For the ambient pressure measurement powdered szomolnokite was loaded into a Kapton tube.
^Pressure errors determined from two tungsten XRD measurements taken before XRD data collection on the sample and immediately after. The only exception is the last compression point (82.85 GPa), where only one XRD measurement was collected on tungsten.

Table S2. Refined lattice parameters of the *P*2/*m* space group

Pressure (GPa)	Pressure error^ (GPa)	*a* (Å)	*a* error (Å)	*b* (Å)	*b* error (Å)	c (Å)	*c* error (Å)	α (°)	α error (°)	β (°)	β error (°)	γ (°)	γ error (°)	Volume (Å^3)	Volume error (Å^3)
16.79	0.34	6.745	0.006	7.051	0.001	6.911	0.007	90.000	0.000	118.225	0.013	90.000	0.000	289.608	0.038
18.33	0.00	6.705	0.006	7.031	0.001	6.862	0.007	90.000	0.000	117.860	0.013	90.000	0.000	285.980	0.035
19.53	0.07	6.672	0.007	7.025	0.001	6.827	0.008	90.000	0.000	117.633	0.015	90.000	0.000	283.473	0.044
20.48	0.11	6.663	0.006	7.019	0.001	6.805	0.007	90.000	0.000	117.572	0.013	90.000	0.000	282.122	0.035
22.52	0.09	6.632	0.006	7.009	0.001	6.769	0.007	90.000	0.000	117.314	0.013	90.000	0.000	279.546	0.036
25.22	0.02	6.563	0.006	7.001	0.000	6.661	0.006	90.000	0.000	116.837	0.013	90.000	0.000	273.058	0.029
28.23	0.04	6.518	0.005	6.984	0.001	6.606	0.005	90.000	0.000	116.535	0.010	90.000	0.000	269.027	0.033
30.73	0.10	6.479	0.003	6.959	0.001	6.563	0.004	90.000	0.000	116.401	0.008	90.000	0.000	265.041	0.026
32.49	0.08	6.451	0.004	6.954	0.001	6.526	0.004	90.000	0.000	116.215	0.008	90.000	0.000	262.651	0.030
34.16	0.18	6.434	0.008	6.962	0.001	6.476	0.008	90.000	0.000	116.304	0.017	90.000	0.000	260.050	0.048
36.74	0.06	6.408	0.007	6.959	0.001	6.448	0.007	90.000	0.000	116.114	0.015	90.000	0.000	258.196	0.046
39.83	0.16	6.368	0.008	6.938	0.001	6.405	0.008	90.000	0.000	116.050	0.016	90.000	0.000	254.235	0.045
42.51	0.14	6.309	0.004	6.918	0.001	6.387	0.004	90.000	0.000	115.574	0.009	90.000	0.000	251.470	0.034
45.08	0.17	6.274	0.005	6.900	0.001	6.352	0.005	90.000	0.000	115.454	0.010	90.000	0.000	248.294	0.032
48.36	0.36	6.252	0.004	6.884	0.001	6.327	0.005	90.000	0.000	115.504	0.010	90.000	0.000	245.789	0.034
50.14	0.32	6.232	0.005	6.878	0.001	6.314	0.005	90.000	0.000	115.554	0.010	90.000	0.000	244.177	0.036
53.54	0.34	6.197	0.005	6.852	0.001	6.275	0.005	90.000	0.000	115.452	0.011	90.000	0.000	240.588	0.037
54.73	0.12	6.171	0.005	6.845	0.001	6.254	0.005	90.000	0.000	115.461	0.010	90.000	0.000	238.508	0.032
58.35	0.19	6.153	0.005	6.839	0.001	6.241	0.005	90.000	0.000	115.500	0.011	90.000	0.000	237.033	0.037
61.94	0.15	6.131	0.004	6.816	0.001	6.208	0.004	90.000	0.000	115.331	0.009	90.000	0.000	234.463	0.033
64.62	0.15	6.125	0.005	6.802	0.001	6.200	0.005	90.000	0.000	115.370	0.010	90.000	0.000	233.379	0.033
67.41	0.06	6.089	0.004	6.796	0.001	6.174	0.004	90.000	0.000	115.376	0.009	90.000	0.000	230.844	0.032
71.10	0.01	6.065	0.006	6.777	0.001	6.136	0.006	90.000	0.000	115.128	0.012	90.000	0.000	228.344	0.043
80.40	0.17	6.005	0.004	6.751	0.001	6.081	0.005	90.000	0.000	115.091	0.010	90.000	0.000	223.278	0.038
82.85	0.00	6.000	0.005	6.731	0.001	6.078	0.005	90.000	0.000	115.170	0.011	90.000	0.000	222.132	0.039

Table S2: Refined lattice parameters of the *P*2/*m* space group.

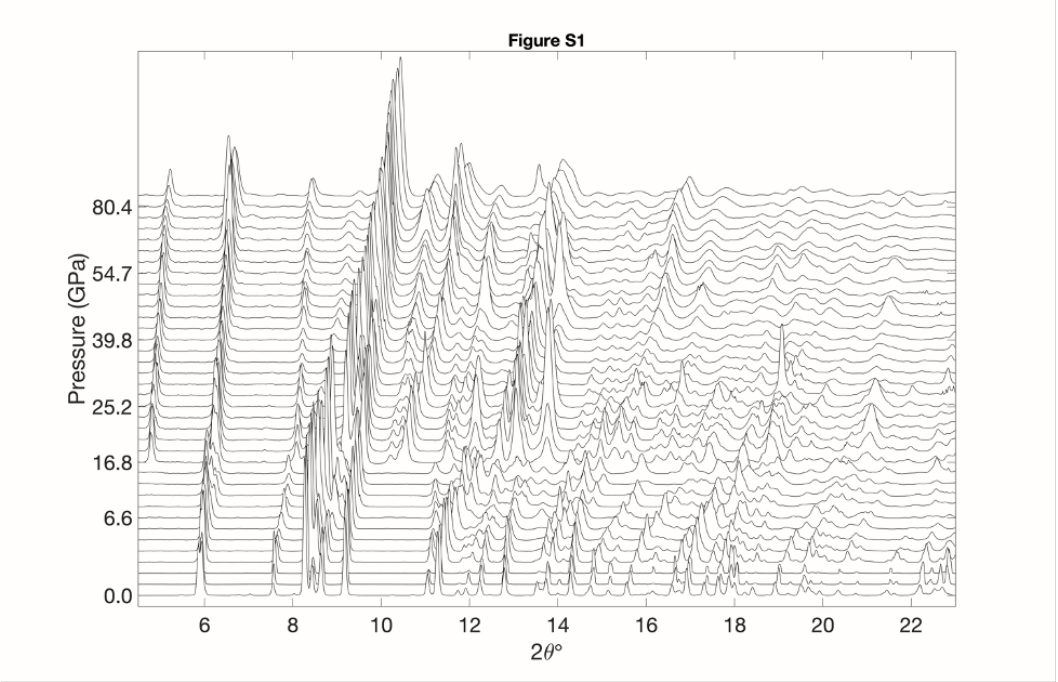

Figure S1: Each pattern has undergone background removal and normalization such that the maximum intensity is equal to one. Each pattern has been plotted as a function of 2θ and set to a uniform height. Patterns are stacked vertically with pressure increasing along the y-axis.

Table S3. Refined lattice parameters of the $P\bar{1}$ space group

Pressure (GPa)	Pressure error^ (GPa)	*a* (Å)	*a error* (Å)	*b* (Å)	*b error* (Å)	c (Å)	*c error* (Å)	α (°)	α error (°)	β (°)	β error (°)	γ (°)	γ error (°)	Volume (Å^3)	Volume error (Å^3)
6.56	0.09	5.024	0.003	5.084	0.002	7.399	0.006	109.480	0.008	109.845	0.009	92.626	0.006	164.886	0.025
8.83	0.10	4.964	0.003	5.093	0.002	7.272	0.009	109.263	0.009	110.037	0.011	92.734	0.006	160.351	0.023
10.05	0.11	4.936	0.005	5.080	0.004	7.230	0.011	109.037	0.016	110.192	0.018	92.712	0.009	158.190	0.034
11.38	0.17	4.906	0.004	5.085	0.003	7.188	0.006	109.454	0.013	110.245	0.011	92.516	0.008	156.073	0.032
12.73	0.32	4.876	0.007	5.069	0.005	7.151	0.011	109.316	0.019	109.866	0.023	92.654	0.010	154.334	0.034

Table S3: Refined lattice parameters of the $P\bar{1}$ space group.

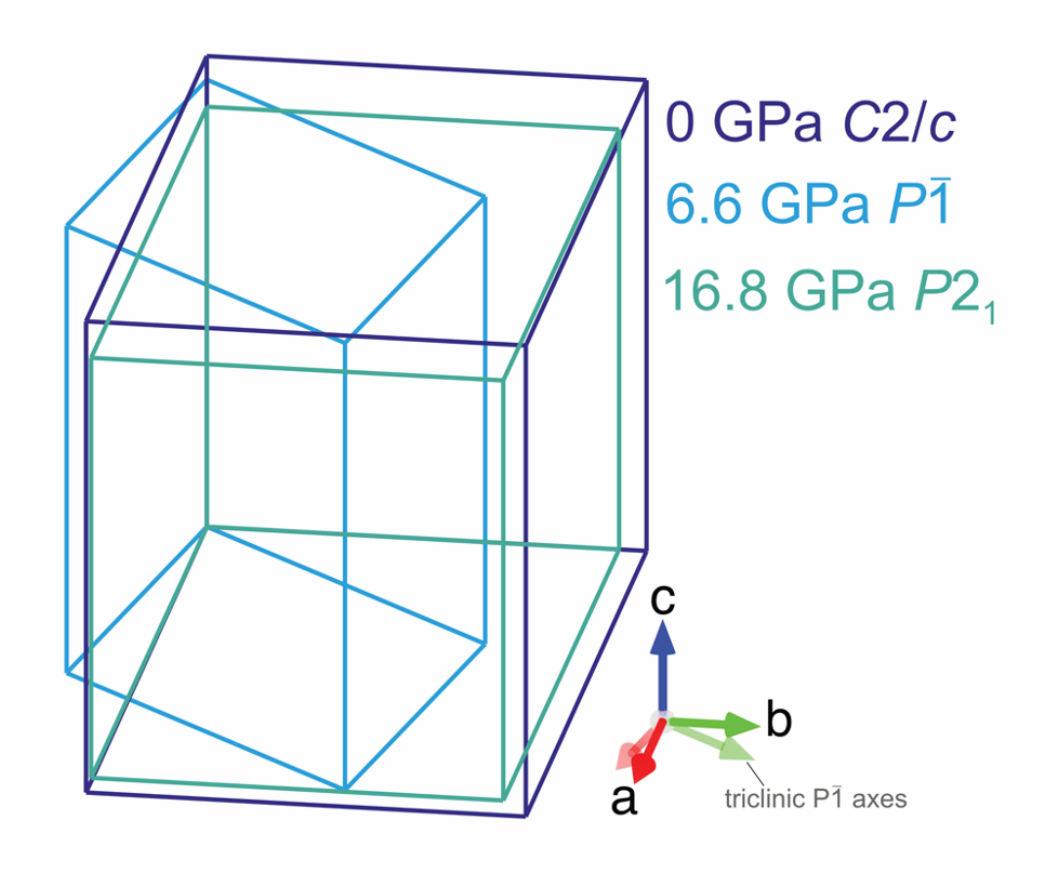

Figure S2: Relative unit cell size and orientation of the three space groups identified within our experimental pressure regime at the lowest pressure of stability. Cells are centered with the assumption that corner Fe-atoms are at the origin. Note the orientation difference between the monoclinic space groups and the mid-pressure triclinic space group. This difference in size and orientation motivates the transformation of the triclinic lattice to a monoclinic setting such that angles α and β are ~90º and the monoclinic setting volume is exactly twice the volume of the triclinic setting. This transformation was carried out using the transformation matrix from Giester, Lengauer, and Redhammer (1994) following Meusburger, Ende, Talla, et al. (2019).

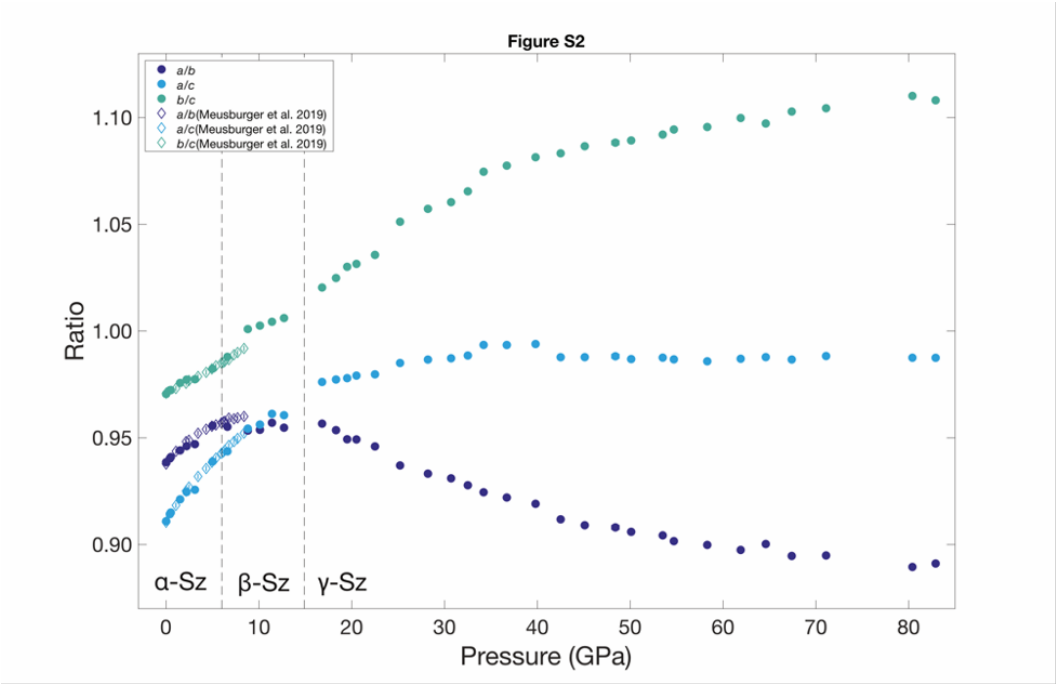

Figure S3: Axial ratios *a*/*b*, *a*/*c*, and *b*/*c* are plotted as a function of pressure for this study as well as those reported by Meusburger, Ende, Talla, et al. (2019). The *b*/*c* ratio continues to increase across the entire pressure range of this experiment. The *a*/*b* ratio increases, then plateaus in the triclinic stability field. After the $P\bar{1}$ to $P2_1$ transition, the *a*/*b* ratio decreases until the last pressure measured. The *a*/*c* ratio increases until plateauing at ~20 GPa.

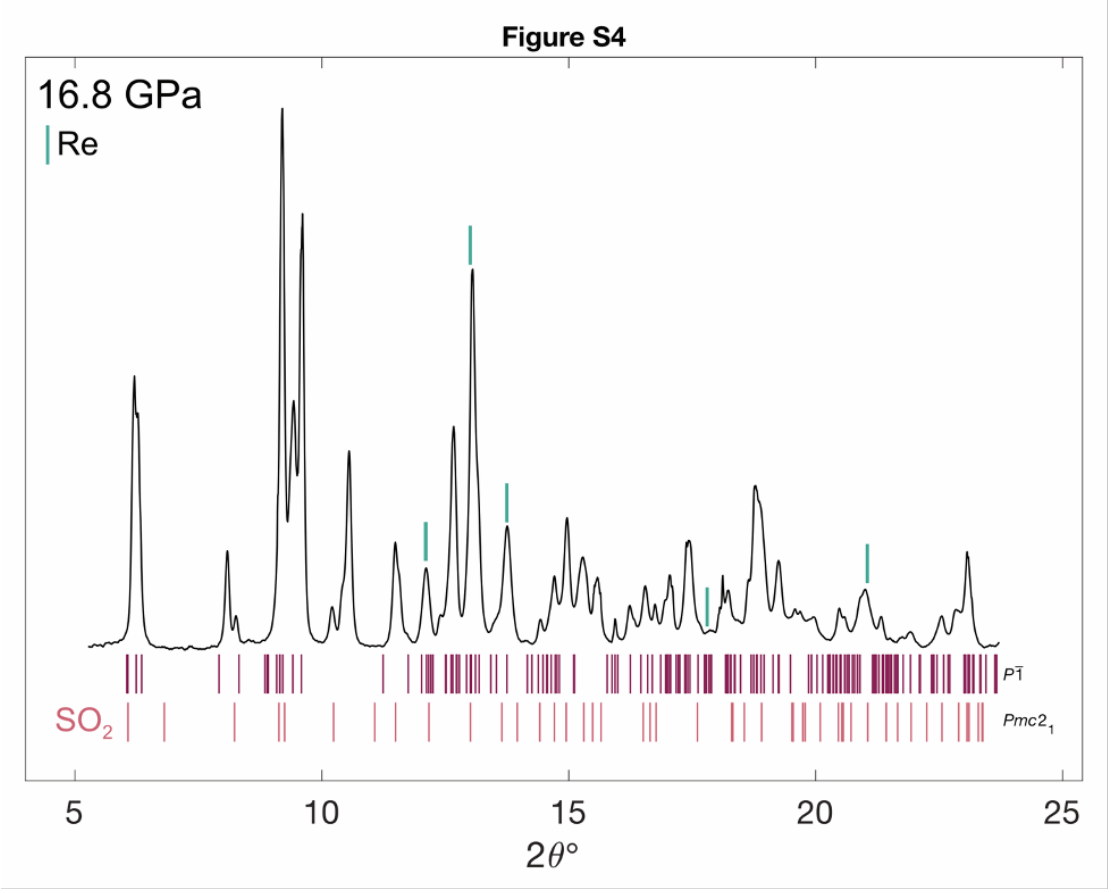

Figure S4: 16.8 GPa XRD pattern assuming that at this pressure szomolnokite remains in the triclinic $P\bar{1}$ phase with the addition of SO_2. Reflections of high pressure SO_2 are taken from a theoretical study by Zhang, Tóth, et al. (2020). Note the absence of reflection corresponding to the new peaks at ~10.5º 2θ.

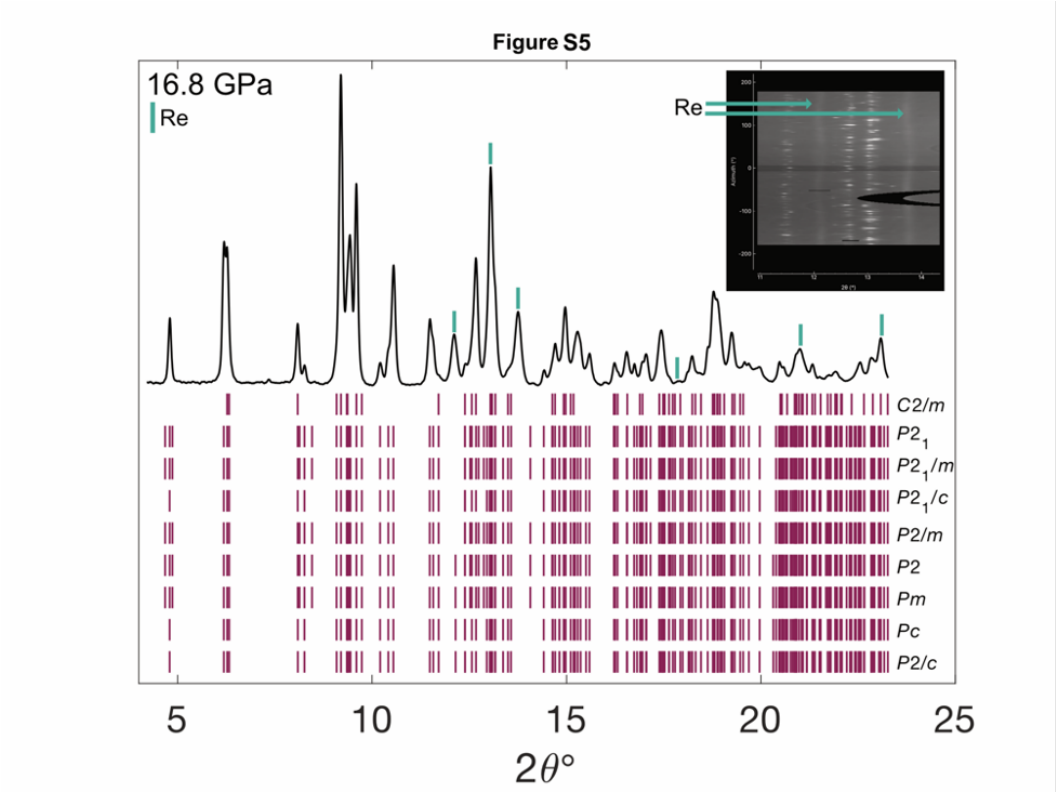

Figure S5: 16.8 GPa XRD pattern with eight candidate primitive monoclinic space groups and one face-centered space group: *C*2/*m*, *P*2$_1$, *P*2$_1$/*m*, *P*2/*m*, *P*2/*c*, *P*2$_1$/*c*, *P*2, *Pm*, and *Pc*. The *C*2/*m* space group lacks reflections associated with the new peaks at this pressure including peaks at ~5º and ~11º 2θ. Re peaks are indicated as the green reflections located above each Re peak. Top right inset shows the raw image zoomed into ~11º-14º 2θ. Green arrows point to the isolated Re peaks.

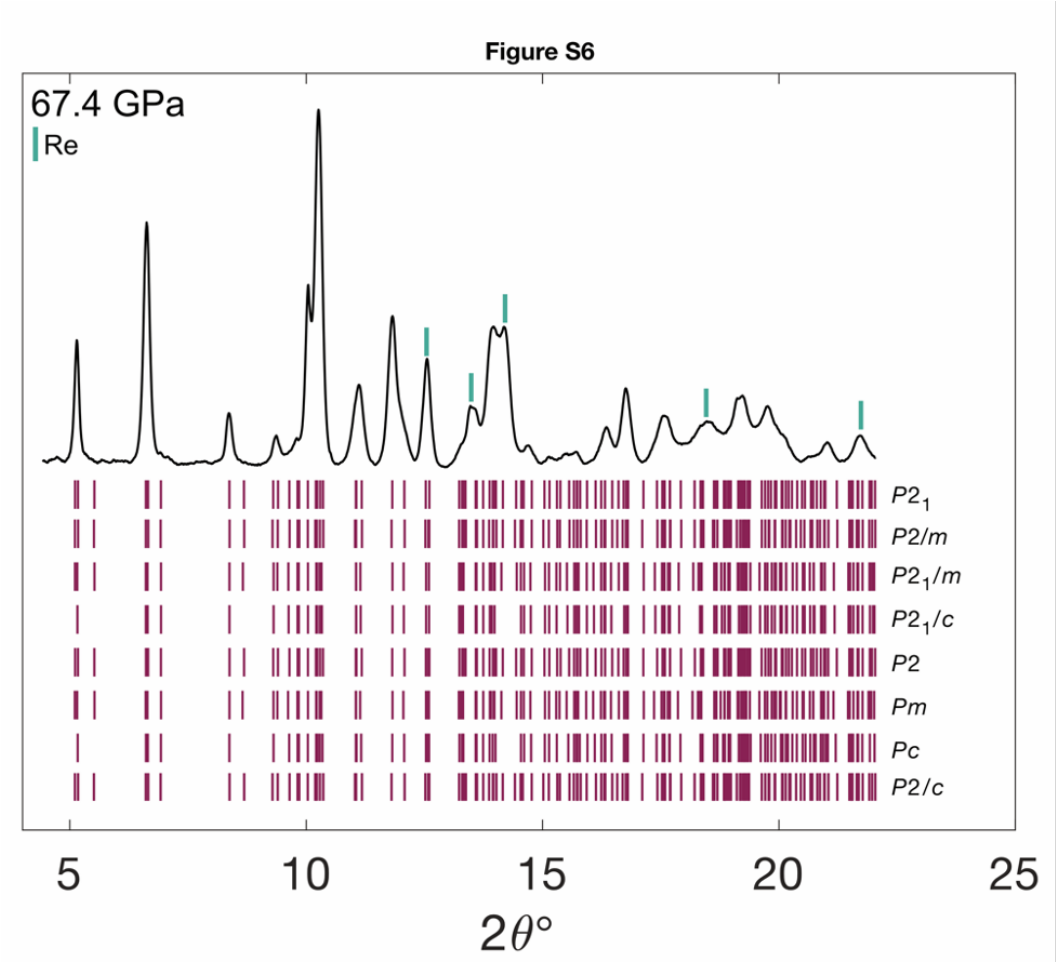

Figure S6: 67.4 GPa XRD pattern with eight candidate primitive monoclinic space groups $P2_1$, $P2_1/m$, $P2/m$, $P2/c$, $P2_1/c$, $P2$, Pm, and Pc. Re peaks are indicated as the green reflections located above each Re peak.

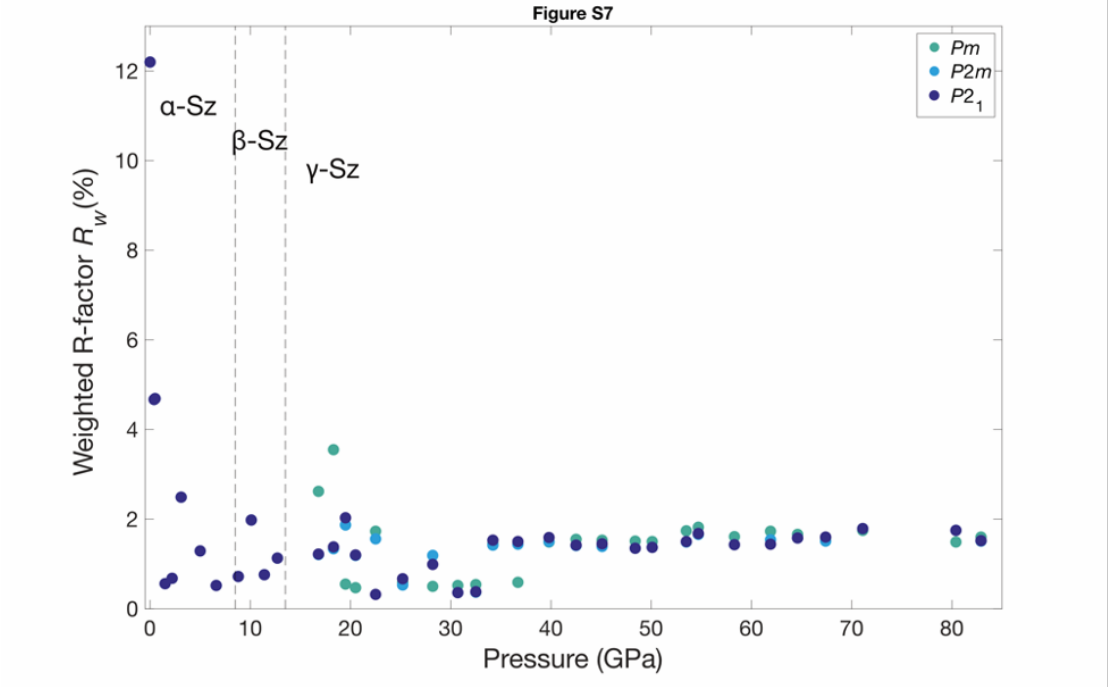

Figure S7: GSAS-II calculates a weighted R-factor (R_w) value useful for comparing different structural fits to a given data set. This factor was not used in place of a visual assessment of structural refinements to the data. The R_w values were used in this study as an additional comparison of competing structural refinements for the new, high-pressure structural transition. Plotted here are three examples of R_w values for the $P2_1$, $P2/m$, and Pm phases. For reasons explained in detail in the main text (including absence of reflections overlapping with Re), the $P2_1$ space group was chosen as the γ-Sz space group. However, R_w values for all three space groups remain approximately constant over the entire pressure range of the γ-Sz phase, with the Pm being slightly more scattered than the other two near 20 GPa. Given the many overlapping low-intensity peaks at higher 2θ values (see Figure S1), the consistency in R_w values at high pressures indicates that several primitive monoclinic space groups can at least fit the high intensity peaks well up to 83 GPa. The room-pressure R_w value is an outlier due to the high signal-to-background ratio, which generally results in artificially high R_w values (for a detailed discussion on R-factors see Toby (2006)). This room-pressure value was measured on powdered szomolnokite loaded in a Kapton tube and thus lacks X-ray diffraction background contribution from the diamonds due to Compton scattering.

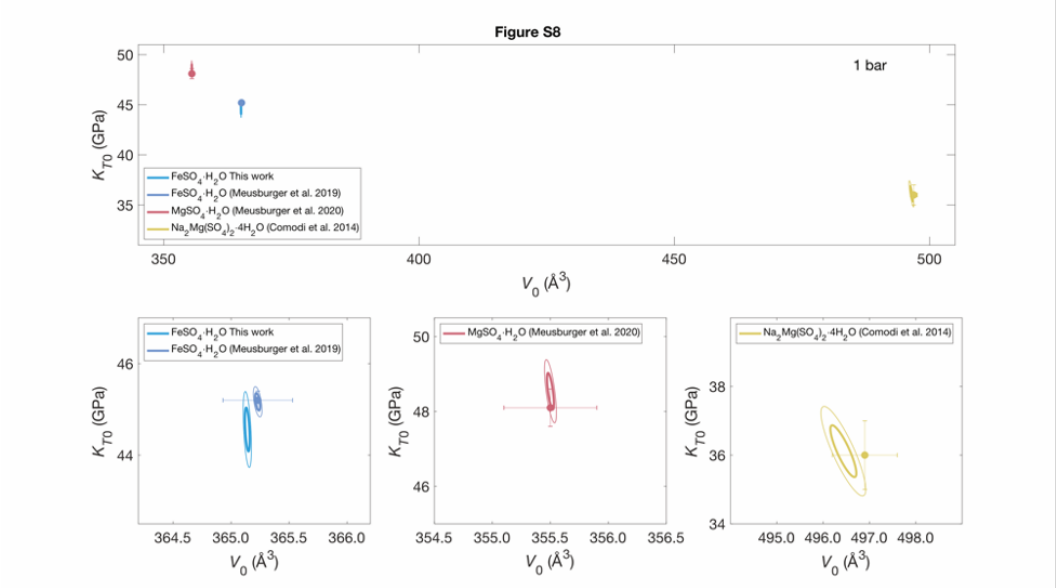

Figure S8: 1σ and 3σ K_{T0} vs. V_{T0} error ellipses for $FeSO_4{\cdot}H_2O$, $MgSO_4{\cdot}H_2O$, and $Na_2Mg(SO_4)_2{\cdot}4H_2O$ at 1 bar.

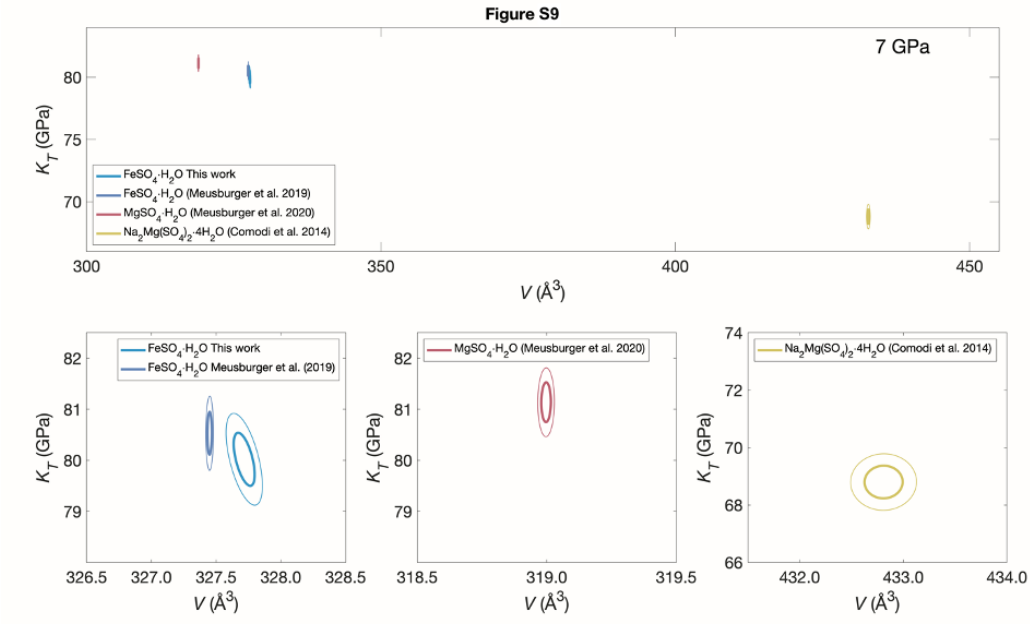

Figure S9: 1σ and 3σ K_T vs. V_T error ellipses for $FeSO_4{\cdot}H_2O$, $MgSO_4{\cdot}H_2O$, and $Na_2Mg(SO_4)_2{\cdot}4H_2O$ at 7 GPa.

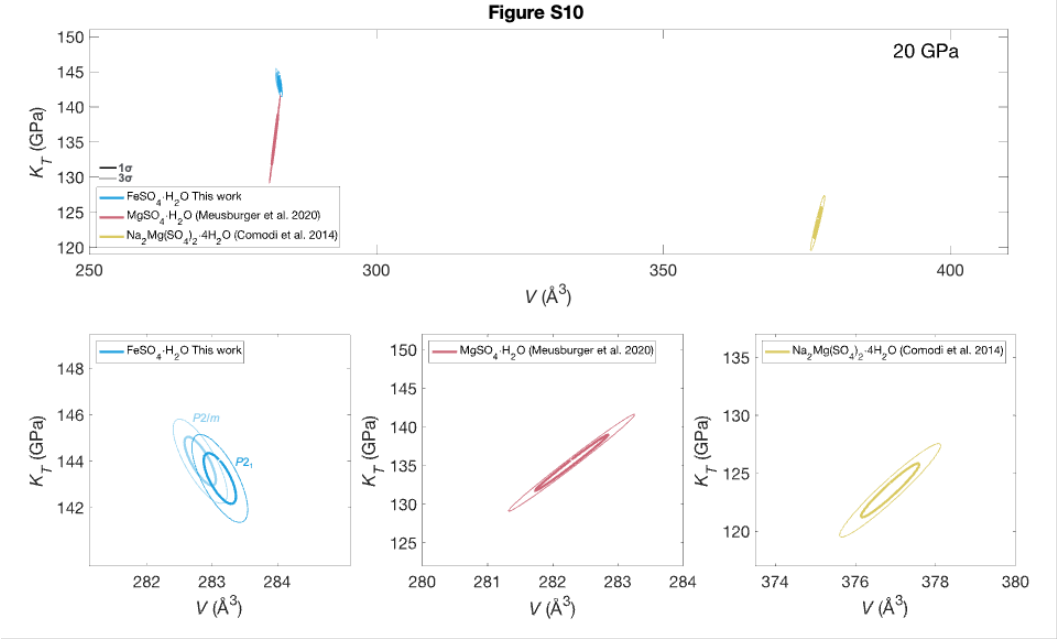

Figure S10: 1σ and 3σ K_T vs. V_T error ellipses for $FeSO_4{\cdot}H_2O$, $MgSO_4{\cdot}H_2O$, and $Na_2Mg(SO_4)_2{\cdot}4H_2O$ at 20 GPa. Both the $P2_1$ and $P2/m$ space group high-pressure EoS parameters are plotted for comparison and are the same within error.

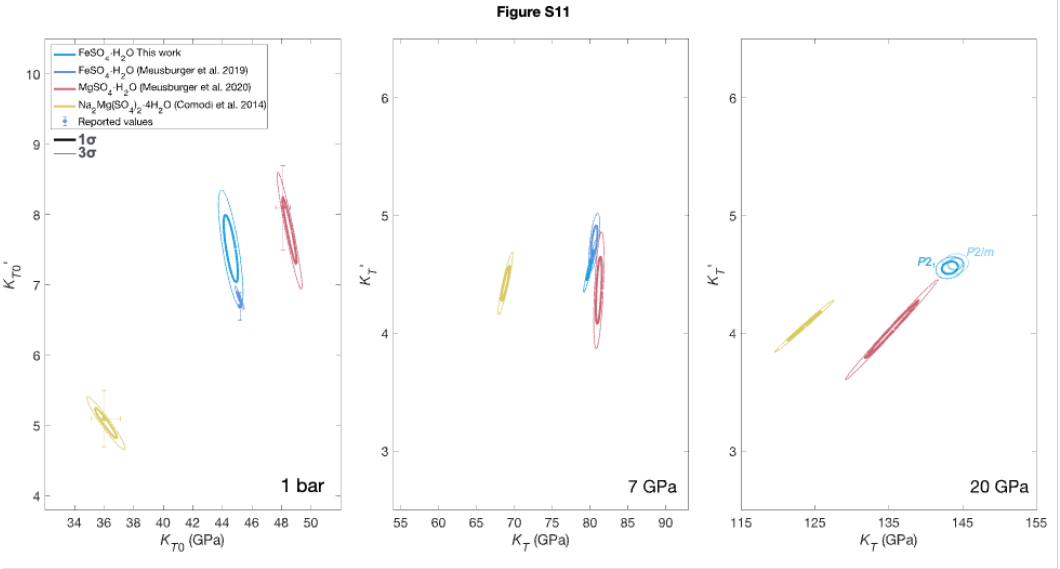

Figure S11: 1σ and 3σ K_T' vs. K_T error ellipses for $FeSO_4{\cdot}H_2O$, $MgSO_4{\cdot}H_2O$, and $Na_2Mg(SO_4)_2{\cdot}4H_2O$ at 1 bar, 7, and 20 GPa, including $P2_1$ vs. $P2/m$ comparison in the far right panel at 20 GPa which have the same values within error.

SUPPLEMENTARY MATERIAL FOR CHAPTER 3

This work	QS Site 1 (mm/s)	QS Site 2 (mm/s)	IS Site 1 (mm/s)	IS Site 2 (mm/s)	FWHM Site 1 (mm/s)	FWHM Site 2 (mm/s)	Weight Fraction Site 1	Weight Fraction Site 2
24-bunch mode A[a] χ^2 = 2.74	2.614(1)	1.804(28)	[1.366]	1.179(9)	0.005(2)	0.034(14)	0.954(3)	0.046(3)
Hybrid mode A χ^2 = 1.29	2.719	1.96(11)	[1.366]	1.366(10)	0.095(2)	0.42(22)	0.974(26)	0.026(26)
24-bunch mode B χ^2 = 1.19	2.669(6)	1.917(71)	[1.366]	1.339(63)	0.011(10)	0.295(11)	0.87(13)	0.130(13)
24-bunch mode C χ^2 = 1.31	2.662(3)	1.993(11)	1.366(6)*	1.216(30)*	0.015(1)	0.761(11)	0.518(10)	0.482(10)
24-bunch D χ^2 = 1.78	2.675(05)	2.065(46)	1.366(6)*	1.216(30)*	0.017(5)	0.754(86)	0.508(36)	0.492(36)
Average:	2.667(37)	1.94(12)	–	1.22(14)	0.028(4)	0.439(84)	0.770(21)	0.230(21)

Reference	QS Site 1 (mm/s)	QS Site 2 (mm/s)	IS Site 1 (mm/s)	IS Site 2 (mm/s)	Linewidth Site 1 (mm/s)	Linewidth Site 2 (mm/s)	Area Fraction Site 1	Area Fraction Site 2
Giester, Lengauer, and Redhammer, 1994	2.71(1)	–	1.26(1)	–	0.23(1)	–	1	–
Alboom et al., 2009)	2.719	–	1.263	–	0.250	–	1	–
Dyar et al., 2013 "S77" χ^2 = 2.23	2.73(2)	1.02(2)	1.26(2)	0.39(2)	0.27	0.30	0.94	0.04
Dyar et al., 2013 "92942" χ^2 = 4.11	2.73(2)	0.61(2)	1.26(2)	0.60(2)	0.34	0.45	0.96	0.04
Dyar et al., 2013 "92942" χ^2 = 14.58	2.76(2)	·–	1.28(2)	–	0.27	–	1	–
Dyar et al., 2013 "92942" χ^2 = 1.44	2.74(2)	0.42(2)	1.27(2)	0.43(2)	0.26	0.48	0.93	0.07
Perez et al., 2020 χ^2 = 1.52	2.679(3)	2.07(3)	1.231(7)	0.98(2)	(FWHM) 0.116(4)	(FWHM) 0.008(4)	(Wt. Fract.) 0.83(6)	(Wt. Fract.) 0.17

Table S1: Ambient conditions hyperfine parameters.
Note: Numbers in brackets indicate fixed parameters. Numbers in parentheses indicate 1σ error.
[a]Hyperfine parameters for ambient pressure measurement of the high-pressure series reported in this work.
*Corrected isomer shift based on simultaneous fitting of sample and stainless steel reference foil hyperfine parameters.

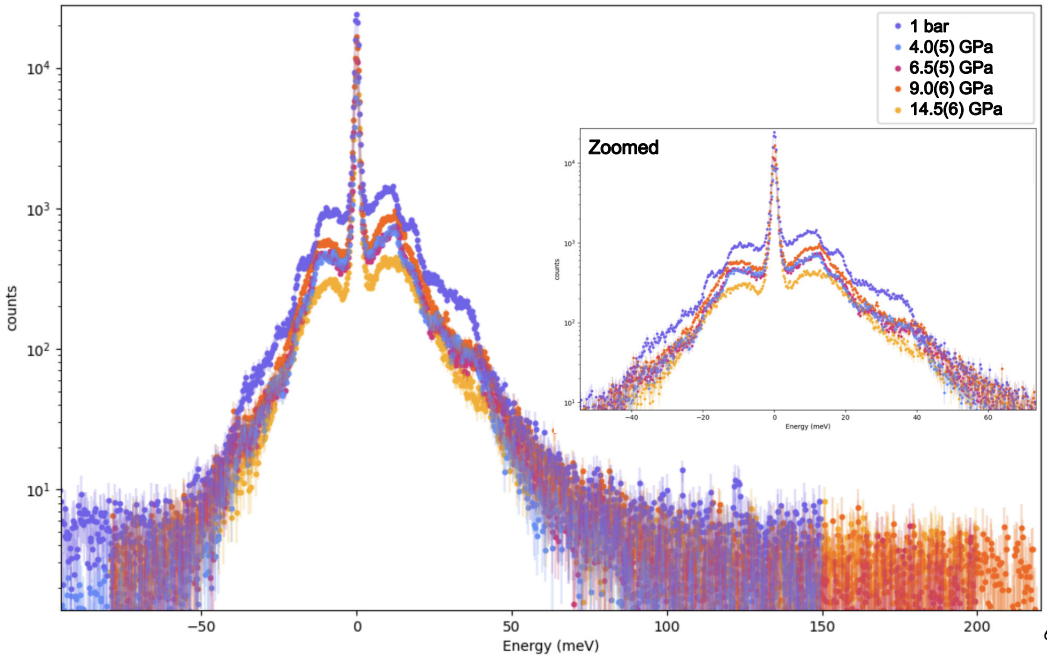

Figure S1: Raw NRIXS data are plotted with their full measured energy range. Inset shows zoomed in portion of the data where the structure of the data is most evident.

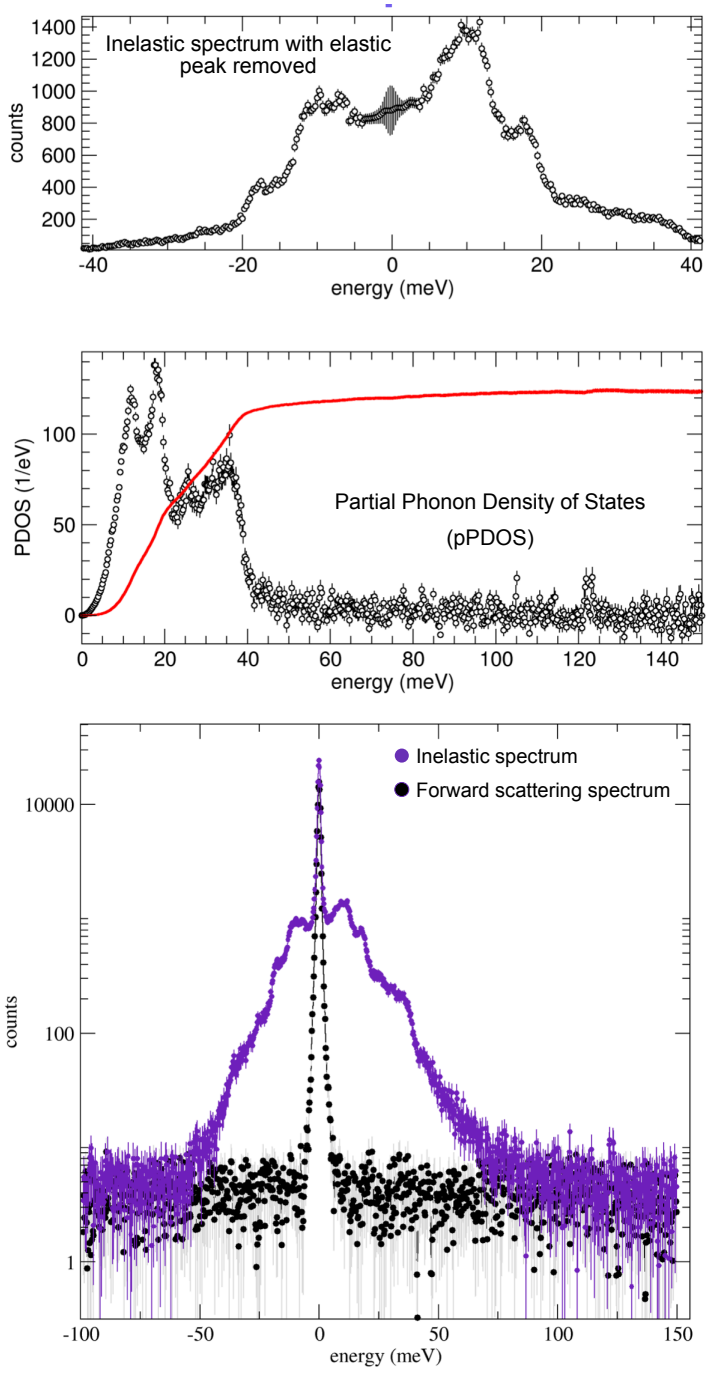

Figure S2: Elastic peak removal. Raw NRIXS and forward scattering data are plotted on the left at 1 bar. Panels on the right show the NRIXS spectrum with the forward scattering (elastic peak) removed.

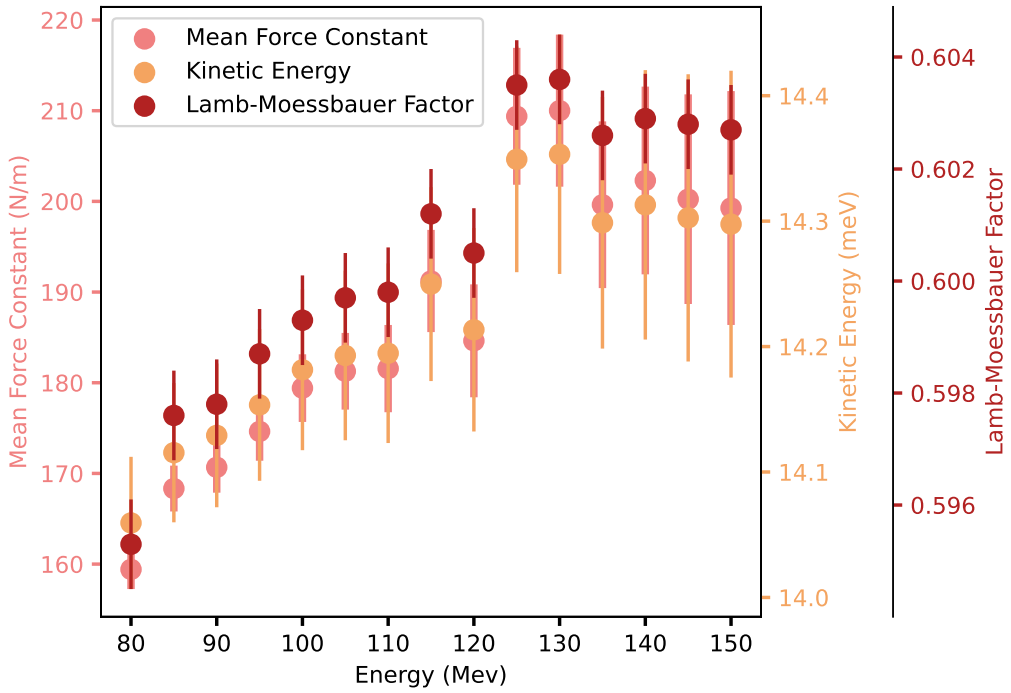

Figure S3: NRIXS parameters determination from singular energy window (MPHOX). 1 bar: -100 to +150 meV. PHOENIX employs a module "MPHOX" which allows NRIXS-derived parameters to be determined from subset of the data. PHOENIX allows easy systematic calculations as a function of cut-off energy. The mean force constant, kinetic energy, and Lamb-Mössbauer factor are plotted above as a function of energy-cut off with 1σ error bars. Example: the values at 100 meV were calculated using the from -100 to +100 meV. MPHOX may be used to determine useful energy windows to calculate parameters from. For example, a plateau in the calculated parameters can mean the measured data does not include any phonon modes that would alter the calculations. In the higher pressure MPHOX plots (**S4-S7**), it is not always apparent which cut-off energy is best to use due to noise in the data, which has motivated the probability density function method reported in the main text and supplemental figures S13-S17.

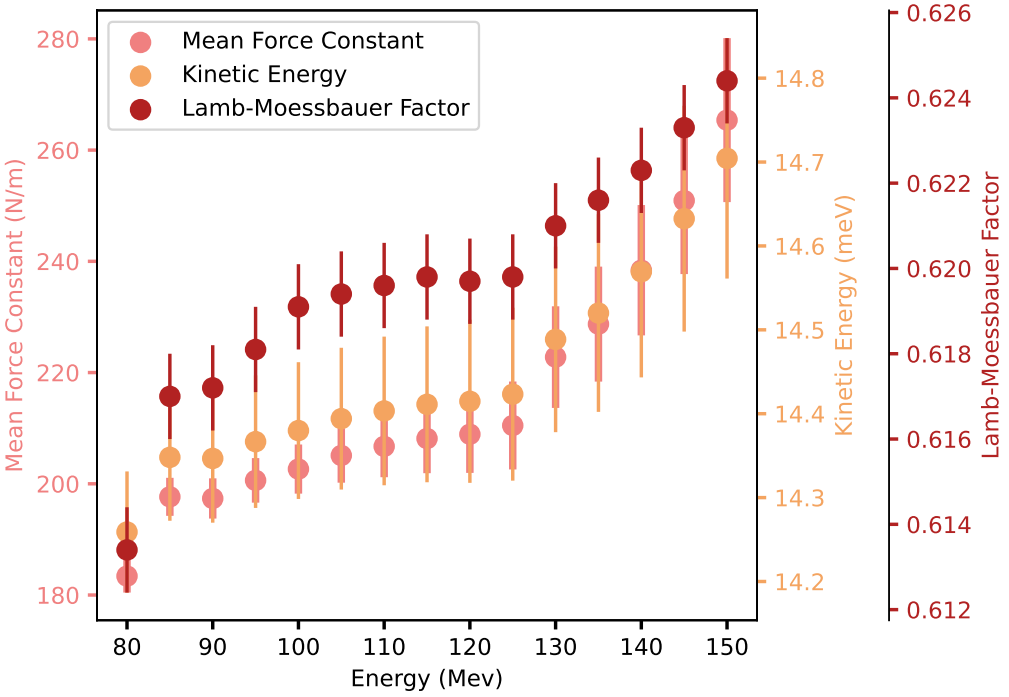

Figure S4: NRIXS parameters determination from singular energy window (MPHOX) – **4.0(5) GPa: -100 to +150 meV.**

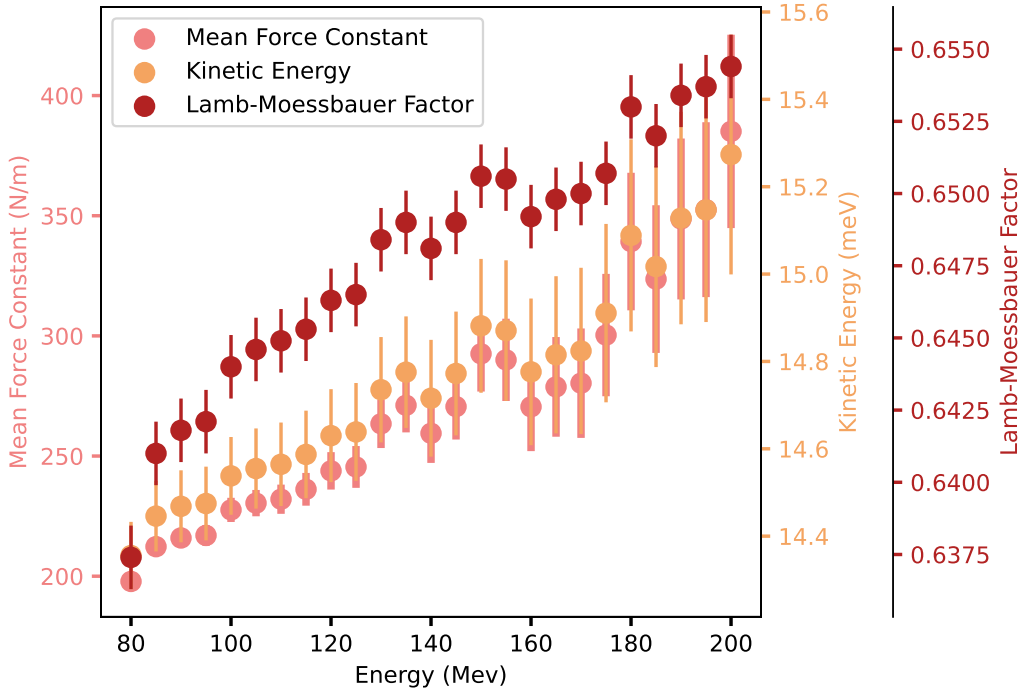

Figure S5: NRIXS parameters determination from singular energy window (MPHOX) – **6.5(5) GPa: -80 to +220 meV.**

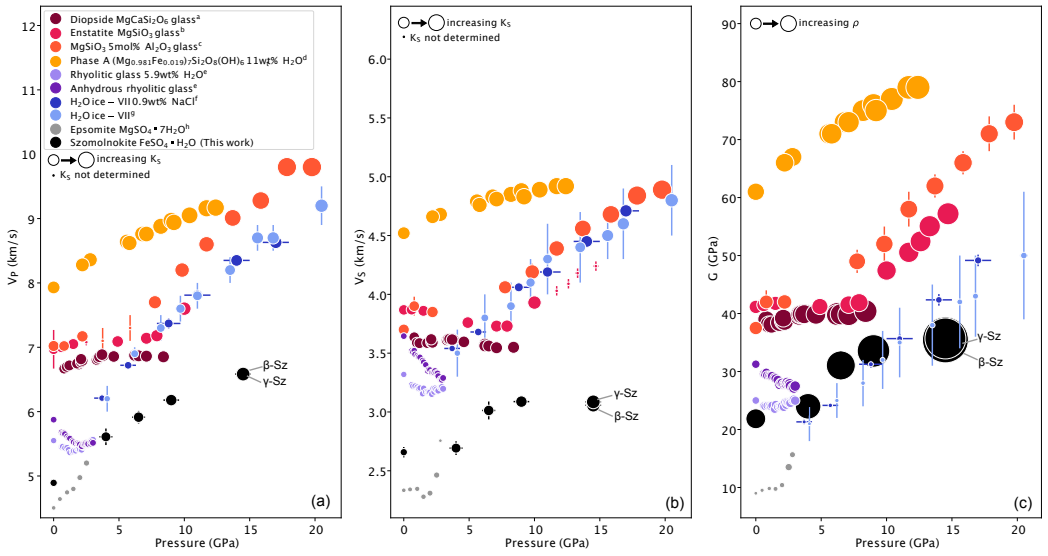

Figure S6: NRIXS parameters determination from singular energy window (MPHOX) – **9.0(5) GPa: -80 to +220 meV.**

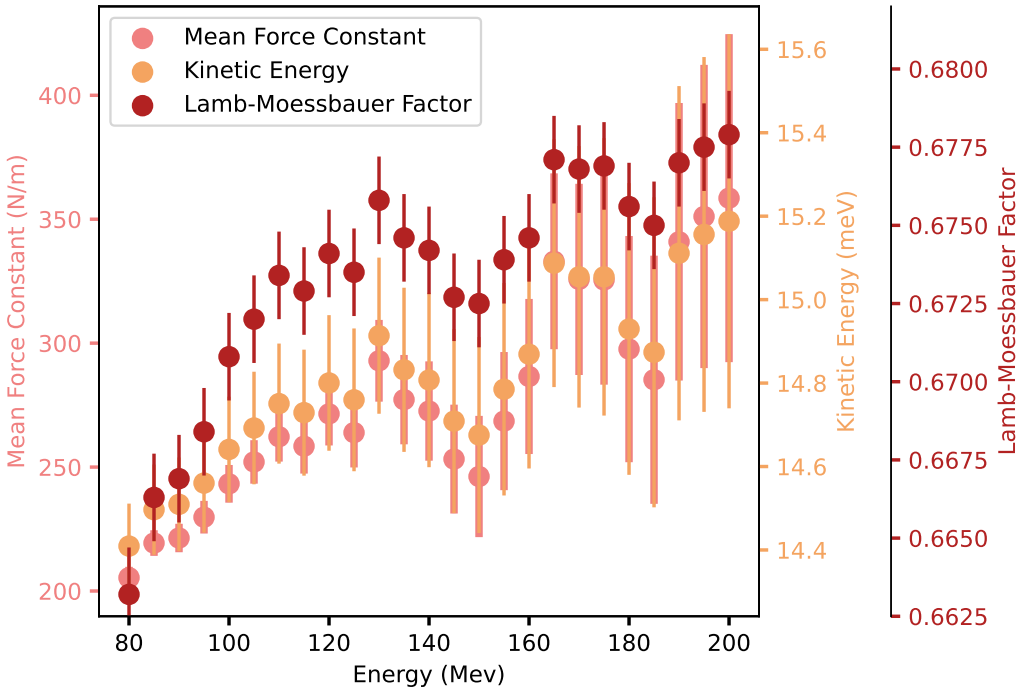

Figure S7: NRIXS parameters determination from singular energy window (MPHOX) – **14.5(6): GPa -80 to +200 meV.**

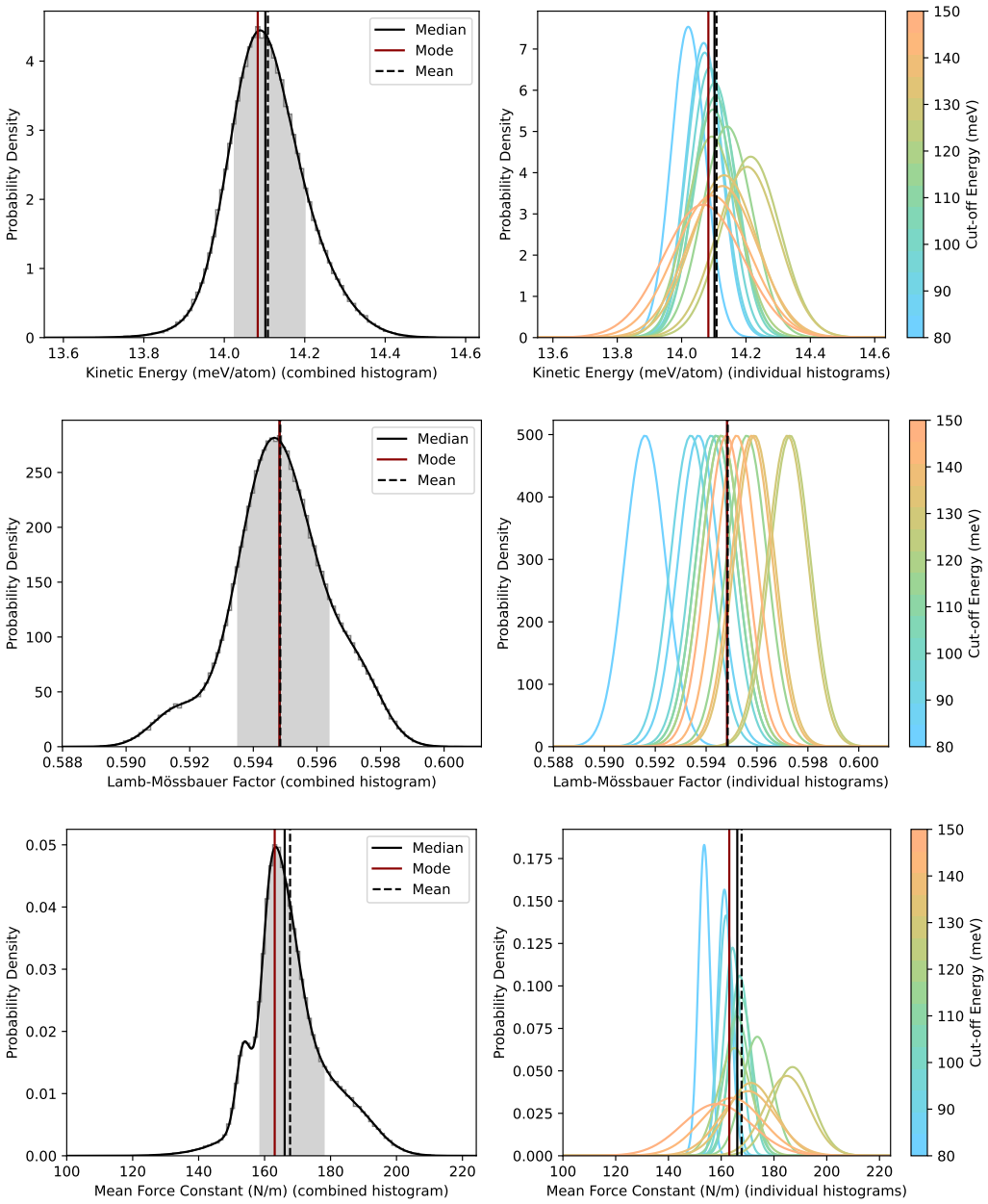

Figure S8: Distributions resulting from MPHOX values – **1 bar: -100 to +150 meV**. The left panels are the probability density distributions resulting from summing (and then normalizing) the series of distributions in the right panels for each parameter (kinetic energy, Lamb-Mössbauer factor, and mean force constant). Individual distributions in the right panels are constructed from randomly sampling within a Gaussian distribution centered at the value reported by MPHOX at that energy cut-off with a full-width at half maximum equal to 2.35σ (see supplementary Figure S3 for an example of MPHOX results.)

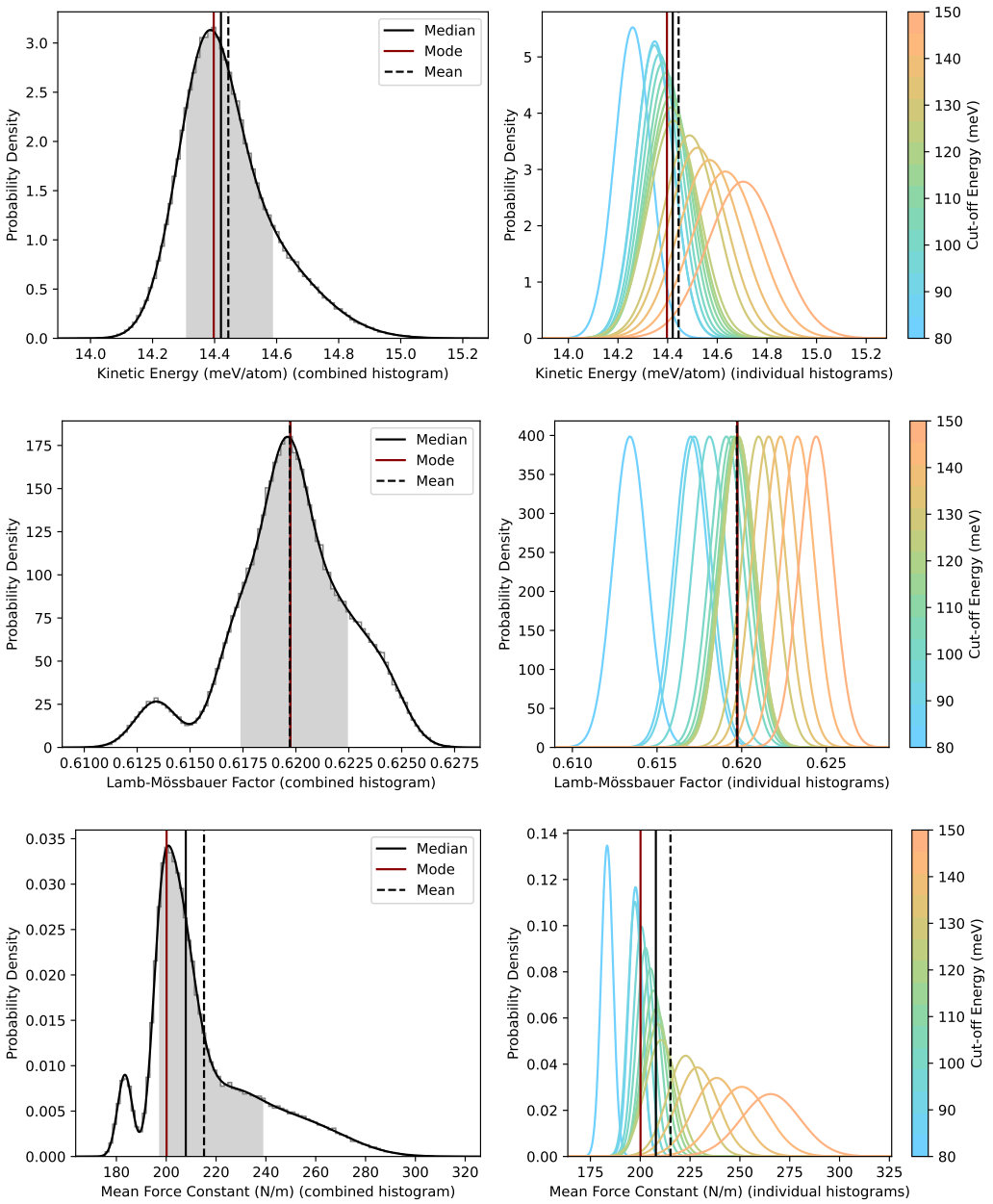

Figure S9: Distributions resulting from MPHOX values – **4.0(5) GPa: -100 to +150 meV.**

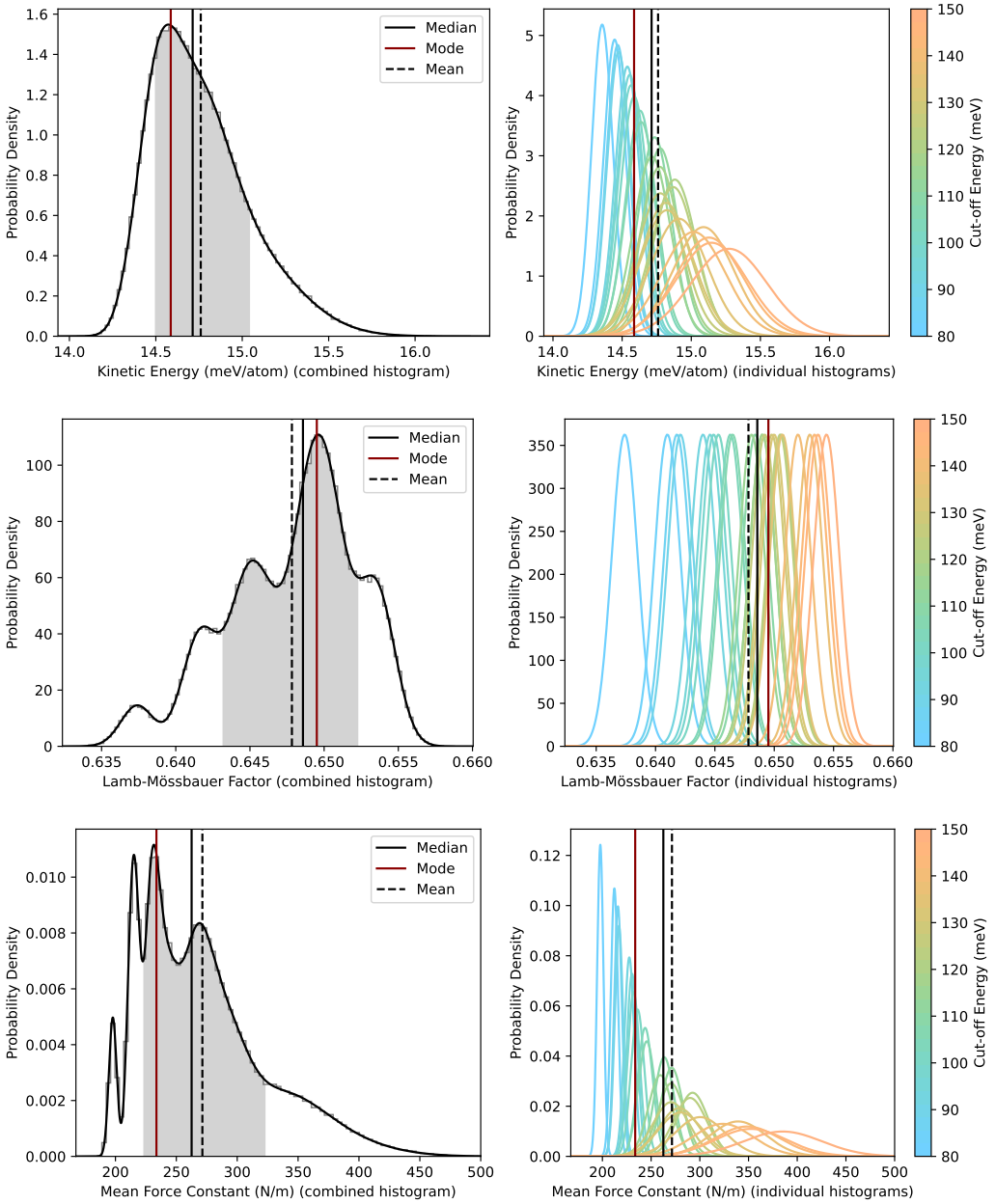

Figure S10: Distributions resulting from MPHOX values – **6.5(5) GPa: -80 to +220 meV.**

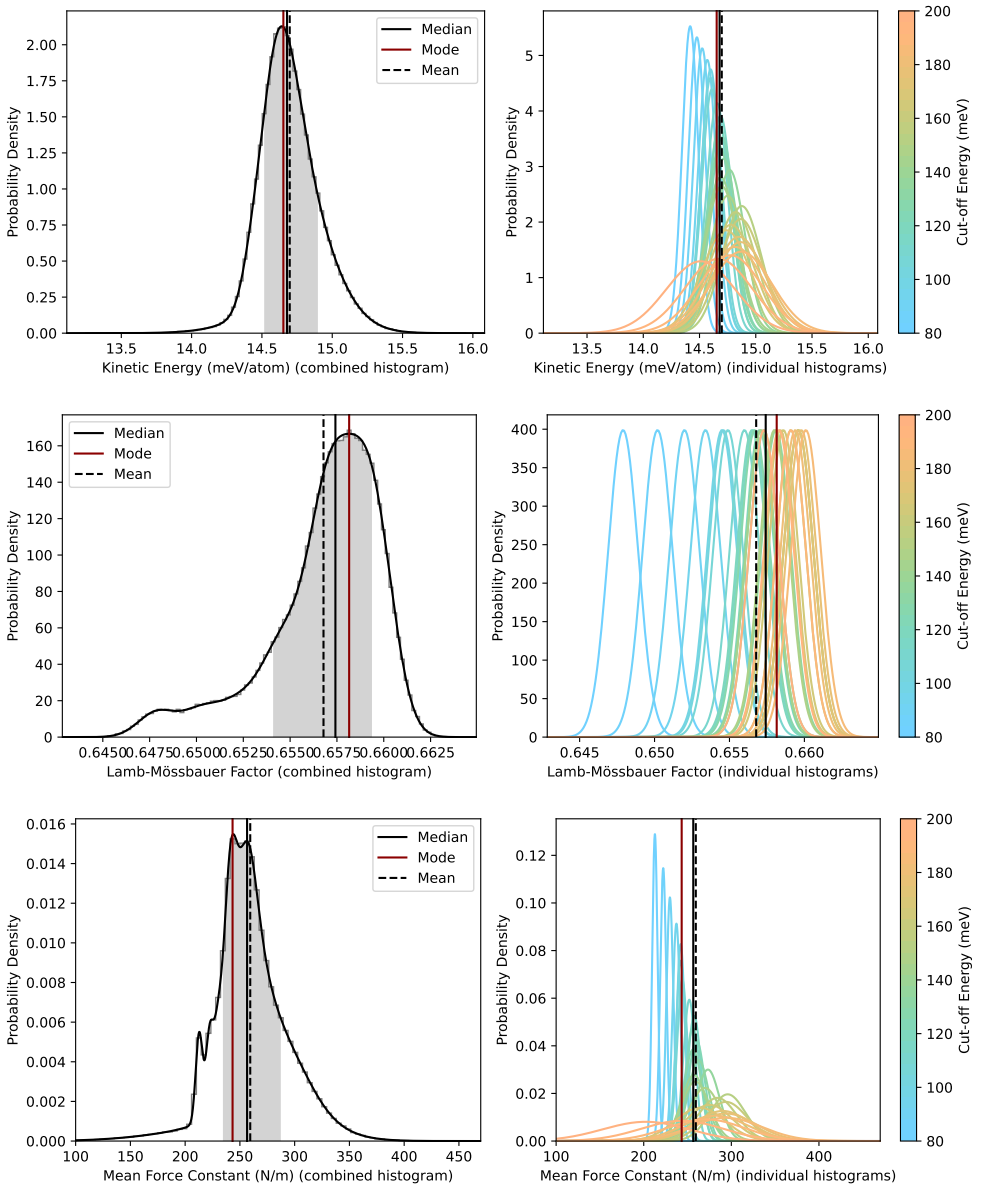

Figure S11: Distributions resulting from MPHOX values – **9.0(5) GPa: -80 to +220 meV.**

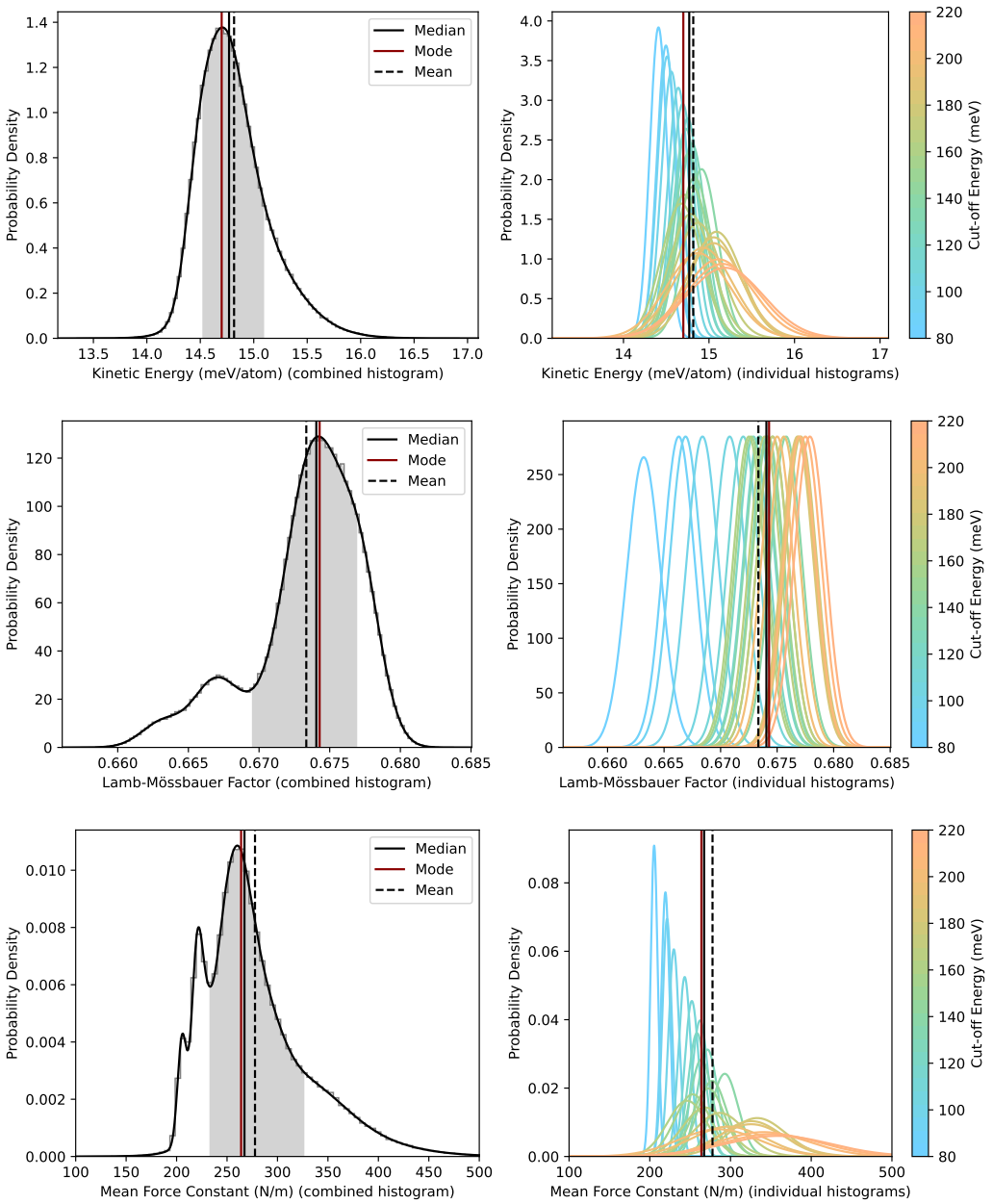

Figure S12: Distributions resulting from MPHOX values – **14.5(6) GPa: -80 to +200 meV.**

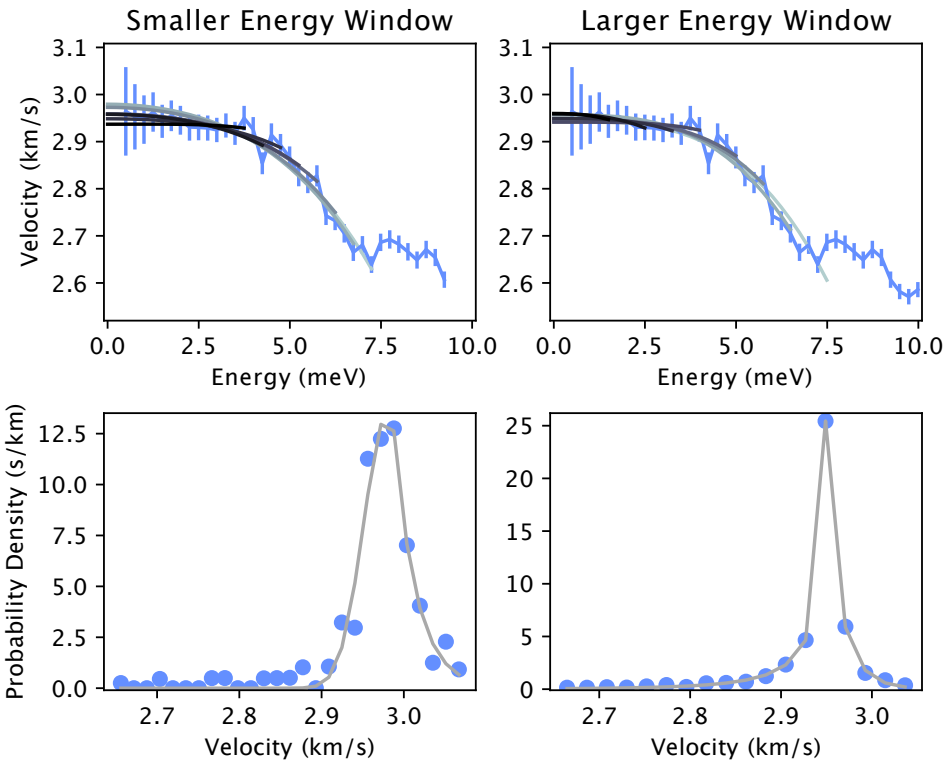

Figure S13: Select velocity fits and velocity probability distributions for each pressure – **1 bar: -100 to +150 meV.**

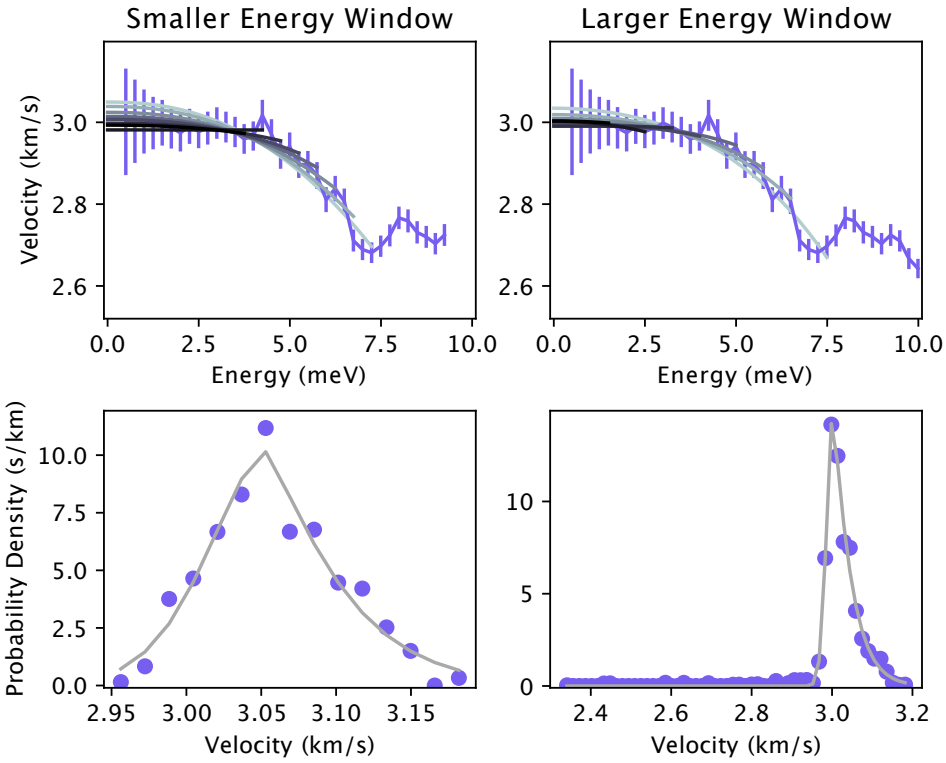

Figure S14: Select velocity fits and velocity probability distributions for each pressure – **4.0(5) GPa: -100 to +150 meV.**

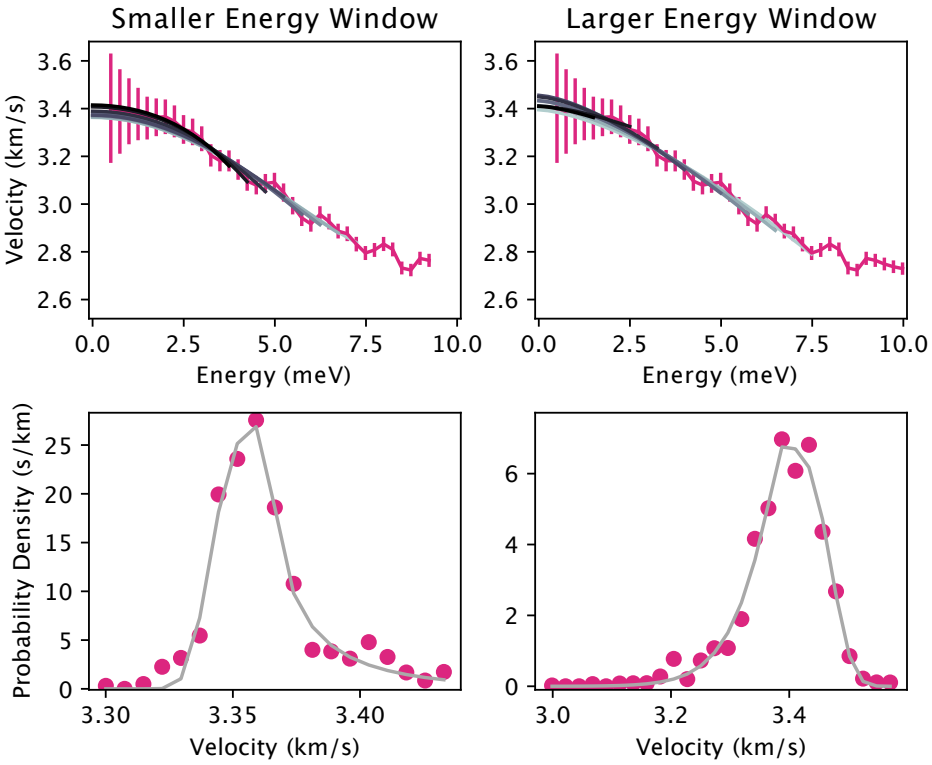

Figure S15: Select velocity fits and velocity probability distributions for each pressure – **6.5(5) GPa: -80 to +220 meV.**

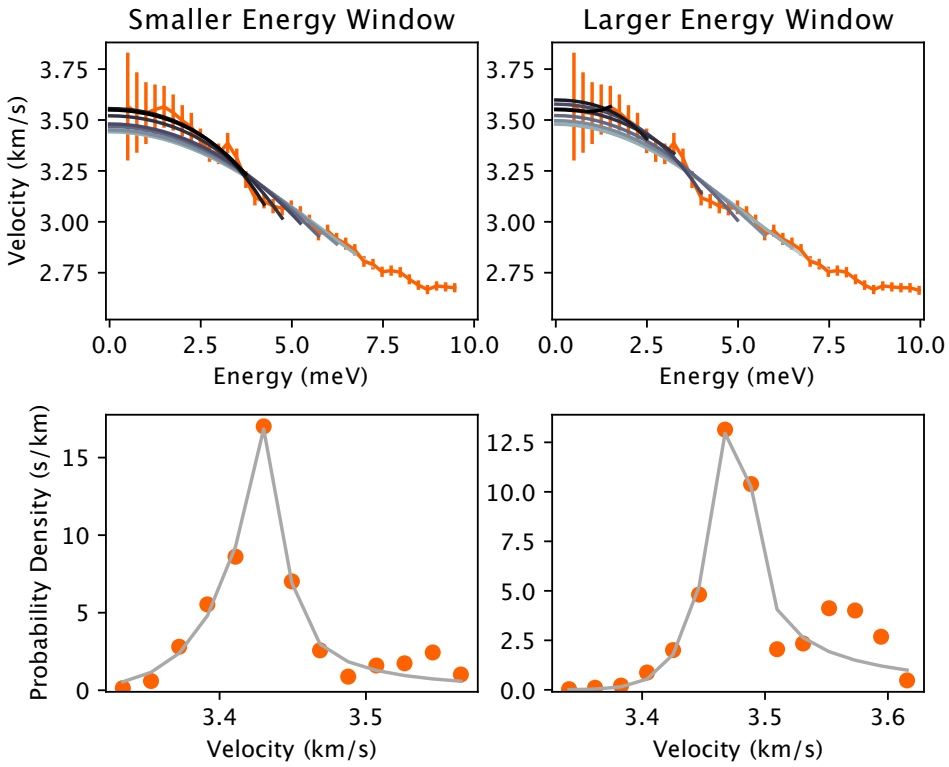

Figure S16: Select velocity fits and velocity probability distributions for each pressure – **9.0(5) GPa: -80 to +220 meV.**

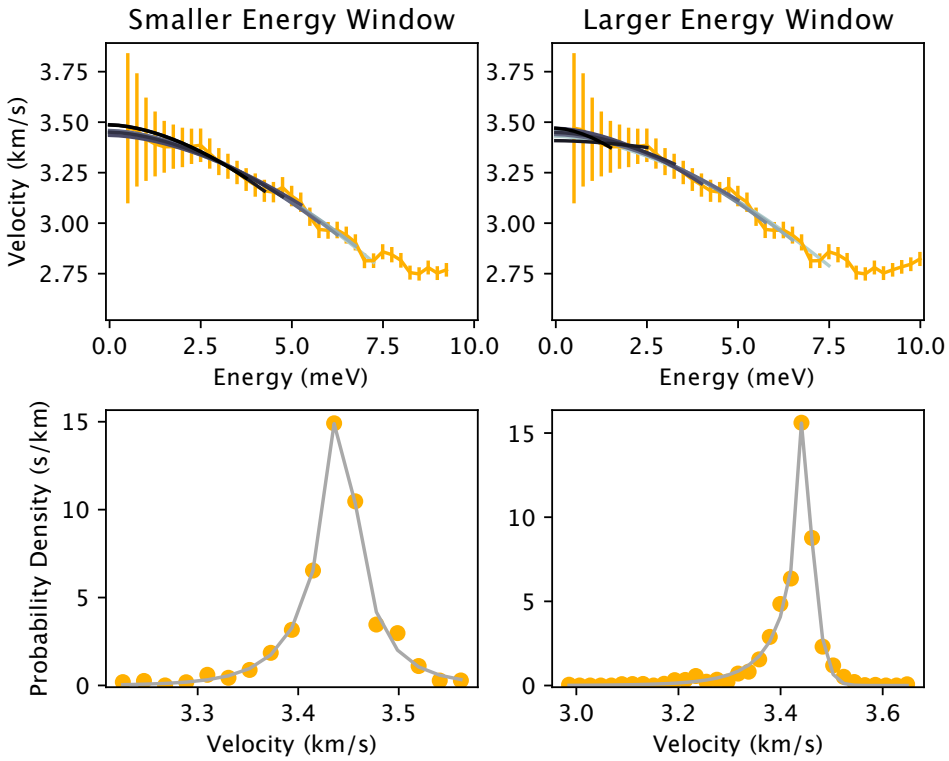

Figure S17: Select velocity fits and velocity probability distributions for each pressure: **14.5(5) GPa -80 to +200 meV, β-Sz phase.**

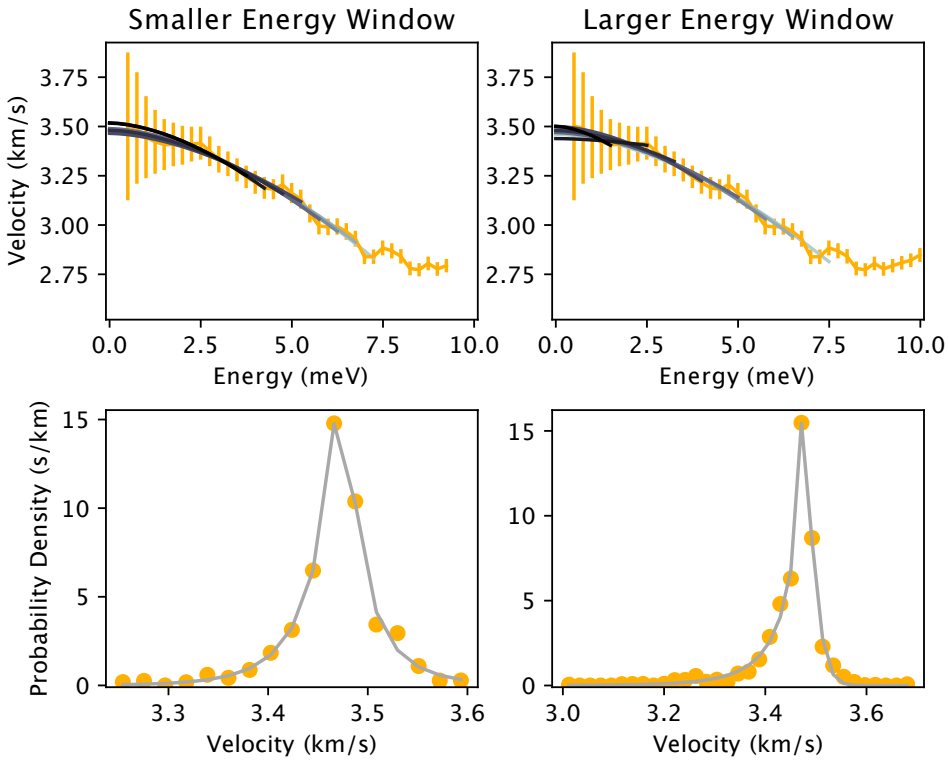

Figure S18: Select velocity fits and velocity probability distributions for each pressure: **14.5(5) GPa -80 to +200 meV, γ-Sz phase.**

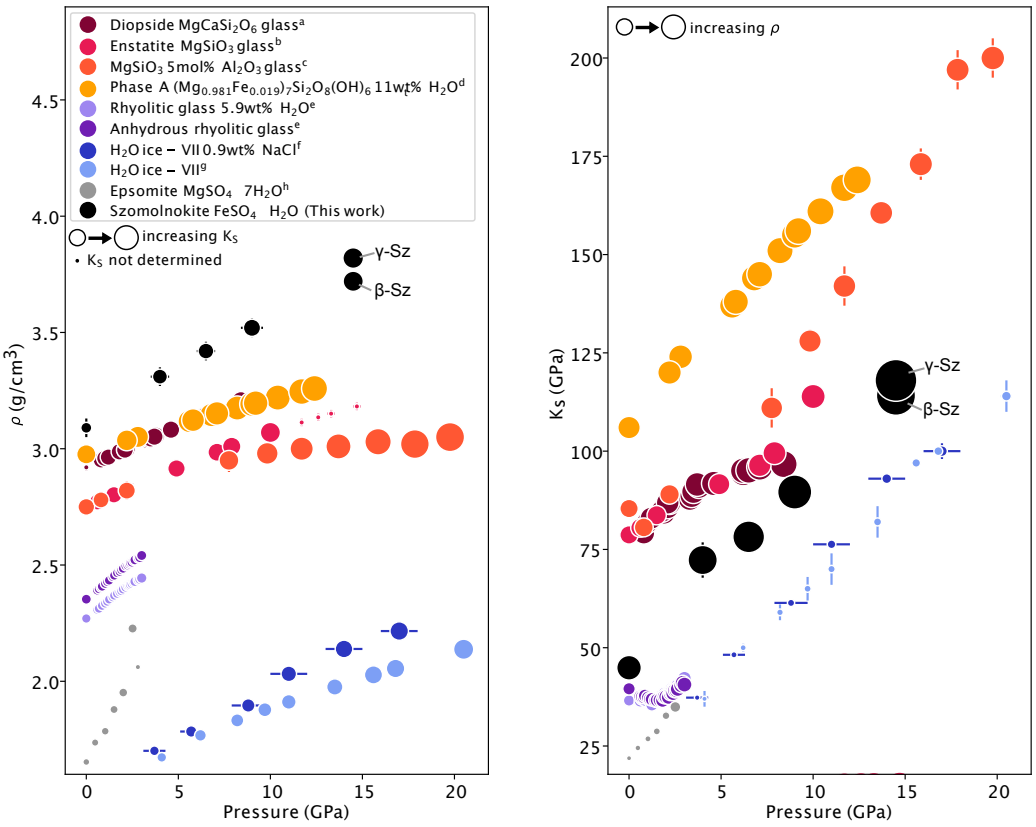

Figure S19: Adiabatic moduli and density comparison of high pressure phases. References are as follows [a]Sakamaki et al. (2014), [b]Sanchez-Valle and Bass (2010), [c]Wei et al. (2022), [d]Sanchez-Valle, Sinogeikin, et al. (2008), [e]Gu et al. (2021), [f]Shi et al. (2021), [g]Zhang, Hao, et al. (2019), and [h]Gromnitskaya et al. (2013) Velocity and pressures errors are plotted when reported, most are smaller than the symbol size. For szomolnokite's highest pressure point, two values are reported using elastic parameters for the β-$FeSO_4{\cdot}H_2O$ and γ $FeSO_4{\cdot}H_2O$ phases.

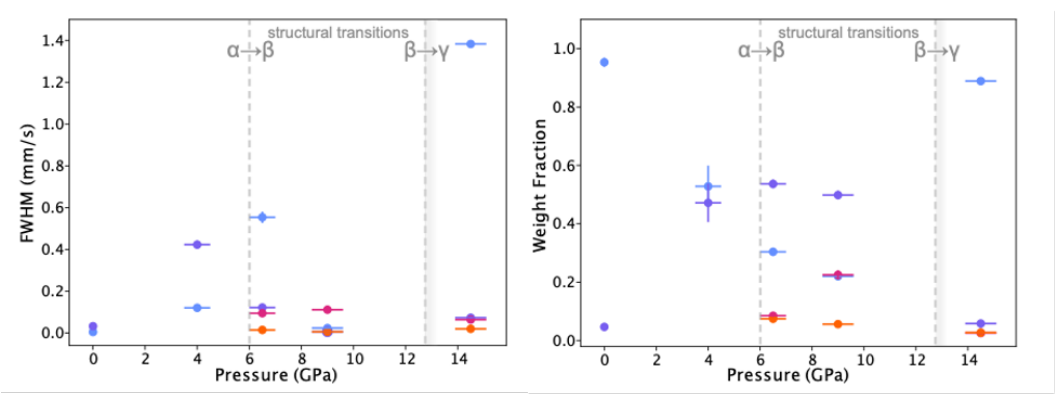

Figure S20: Weight fraction and full-width at half-maximums of iron sites measured by synchrotron Mössbauer measurements. All compression points were fit with a texture parameter fixed at 21.

SUPPLEMENTARY MATERIAL FOR CHAPTER 4

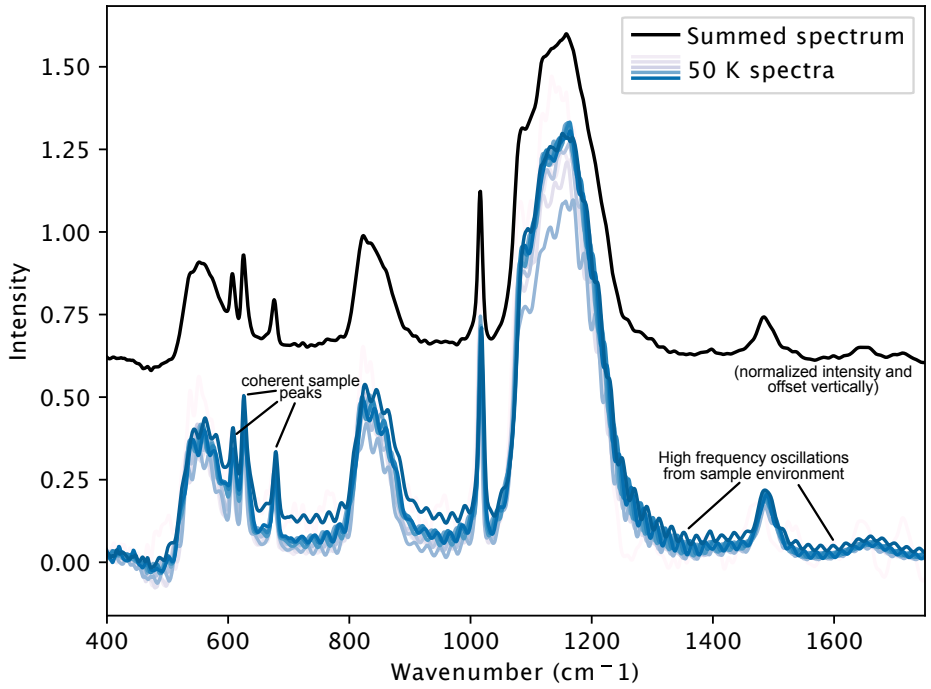

Figure S1: An example of diamond fringes in the 50 K compression dataset. High frequency oscillations throughout the spectrum <1800 cm^{-1} black were present. These high frequency oscillations ("fringes") are due to the interference of light scattering in the sample chamber between the two diamond anvils. Fringes may shift their wavenumber position and display changes in amplitude as a function of pressure. At low wavenumbers ~650 cm^{-1}, the smaller peaks originating from sample signal have similar shapes/widths as the fringes, and without the a priori knowledge that three sample modes should be located in this region, differentiation of sample peaks from the fringes is difficult. Viewing the entire data series is helpful in identifying coherent signal (see figure annotation), as the fringes shift more quickly than the sample modes with increasing pressure. The summation of all spectra in this dataset is plotted above the individual spectra. For this dataset, the fringes present in one spectrum are out phase with the fringes of a spectrum at another pressure. When all the spectra are summed, the fringes essentially disappear and signal originating from sample modes is clear.

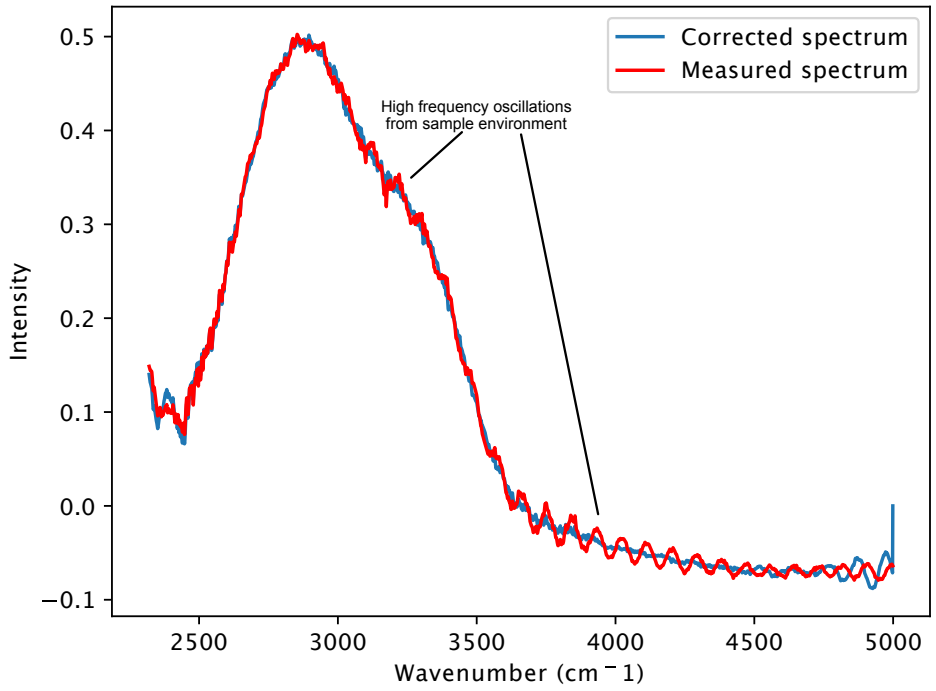

Figure S2: An example of diamond fringes in the H_2O stretching region for the highest pressure data point in the 300 K compression series (red spectrum). Though the broadness of the peaks is qualitatively clear, artifacts in the spectral shape due to fringes may influence the fitting procedure performed in Fityk. The corrected spectrum is plotted in blue (see Figure S3 for correction).

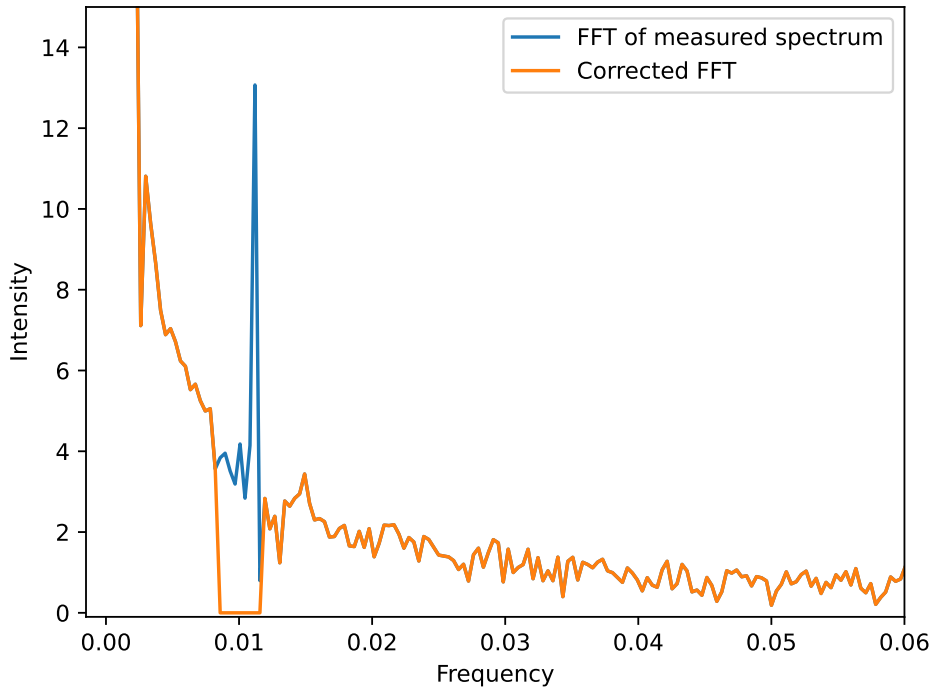

Figure S3: The fast Fourier transform (FFT) of the measured in spectrum plotted in Figure S2 is plotted here in blue and is overlain by the correct FFT (orange). The peak at ~0.01 is due to the diamond fringe oscillation. Removal of this frequency region thus removes the unwanted fringe oscillations upon back transformation of the spectrum.

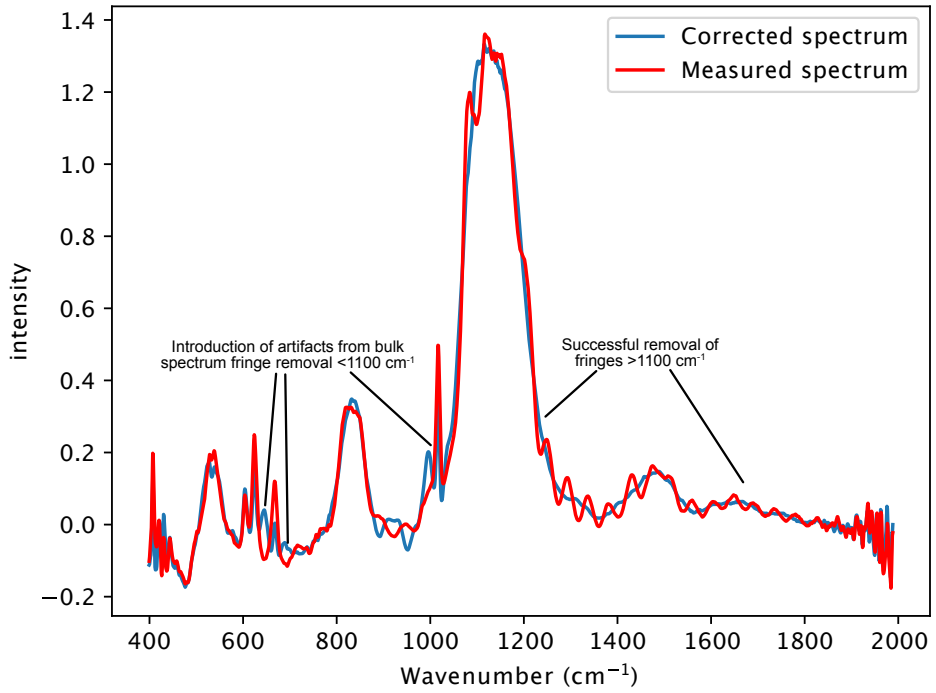

Figure S4: An example of fringes in the spectral region <2000 cm^{-1} for a 300 K 1 bar spectrum (red). Upon taking the fast Fourier transform (FFT) of the spectrum (see Figure S5), the fringe oscillation is removed from the entire spectrum (blue spectrum). As discussed in the main text, removal of the fringe oscillations for the entire low wavenumber region is difficult due to the similar peak shape/widths of the sample signal. This improper removal decreases the intensity of the narrow peaks and introduces artifacts adjacent to the peaks as annotated in the figure. For this region, long-wavelength features like the ~550 and 850 cm^{-1} H_2O libration modes were treated for fringe removal, while the narrower peaks like those at 625 and 1020 cm^{-1}were fit in isolation. Removal of the fringes is successful for wavenumbers >1100 cm^{-1}.

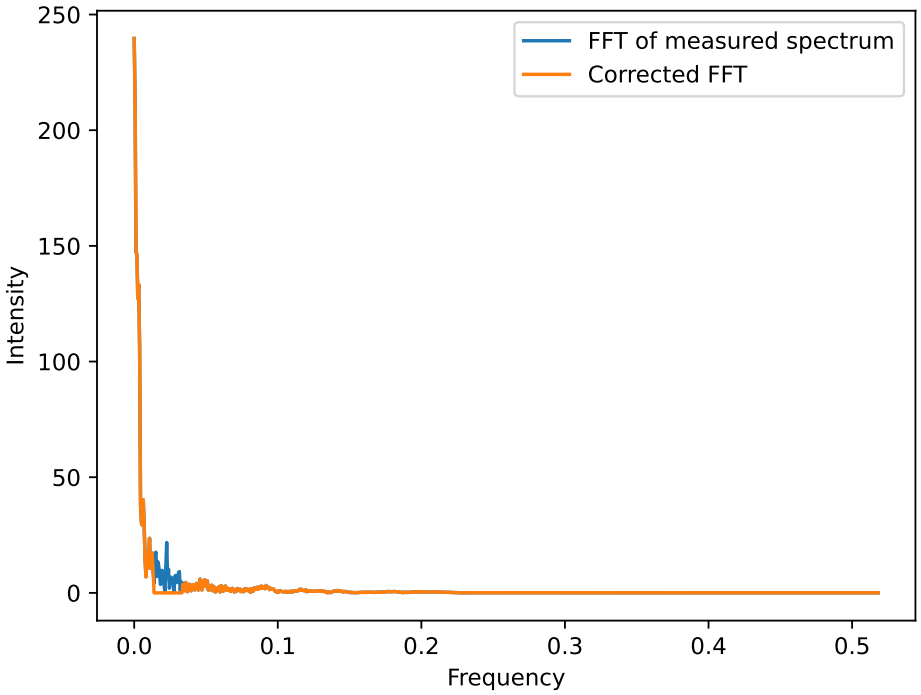

Figure S5: The fast Fourier transform (FFT) of the measured in spectrum plotted in Figure S4 is plotted here in blue and is overlain by the corrected FFT (orange). The peak at ~0.025 is due to the diamond fringe oscillation. Removal of this frequency region thus removes the unwanted fringe oscillations upon back transformation of the spectrum but also effects smaller peaks and generates artifacts for regions of the spectrum <1100 cm^{-1}.

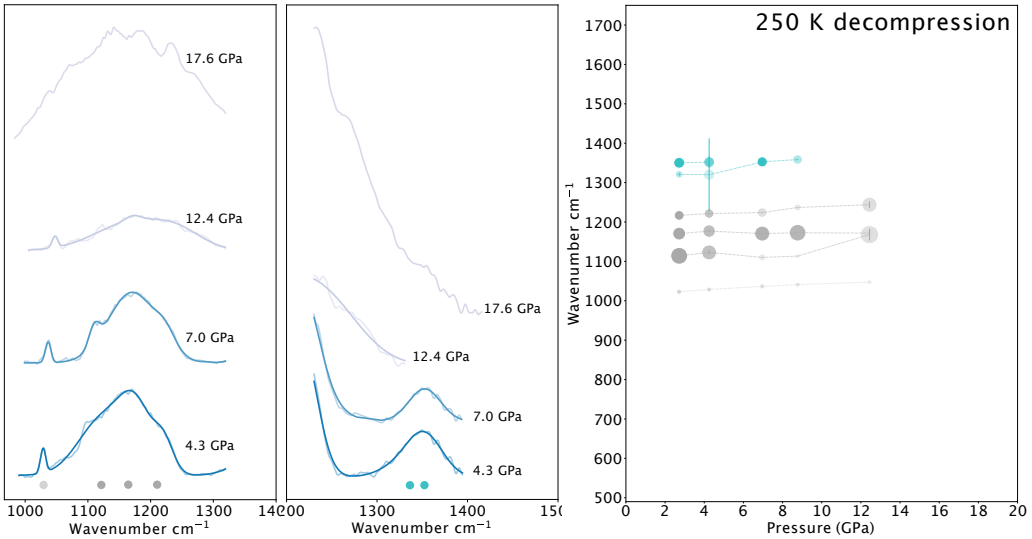

Figure S6: Select spectra from the 1000-1700 cm-1region for the 250 K high pressure dataset and the fitted peak positions for all data. The spectrum <1000 cm-1 was unresolvable. Symbol sizes represent the full-width half maximum of each peak. Symbol opacity represent the peak's height, relative to itself.

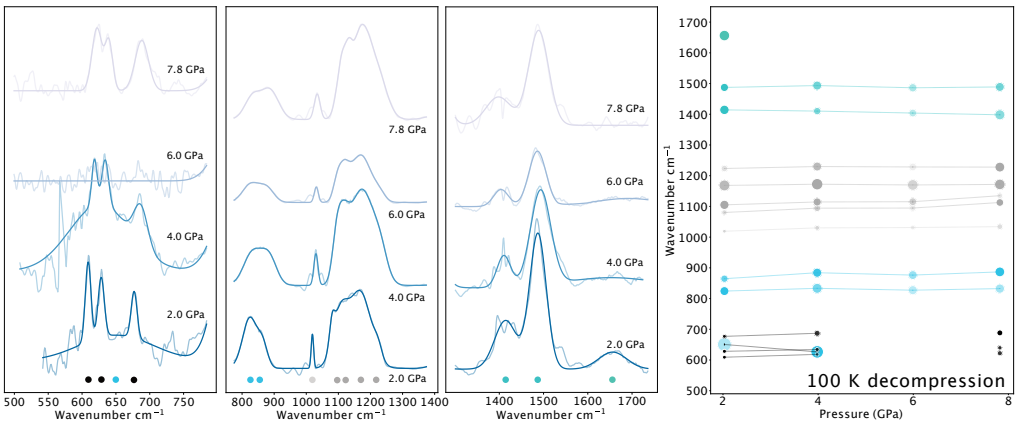

Figure S7: Select spectra from the 550-1700 cm-1 region for the 100 K decompression high pressure dataset and the fitted peak positions for all data. Symbol sizes represent the full-width half maximum of each peak. Symbol opacity represent the peak's height, relative to itself. The 500-750 cm-1 mode was unresolvable at 6 GPa.